AGU100 ADVANCING EARTH AND SPACE SCIENCE

Geochemistry, Geophysics, Geosystems

RESEARCH ARTICLE
10.1029/2017GC007260

Key Points:
- The 1.65-Ma Crystal Knob volcanic pipe hosts xenoliths that sample the deep mantle lithosphere near the California coast
- Spinel peridotites equilibrated near 1000 °C at depths between 45 and 75 km and show a signature of deep melt interaction
- The mantle lithosphere beneath the Coast Ranges was tectonically underplated during the Cretaceous and heated by the Neogene slab window

Supporting Information:
- Supporting Information S1

Correspondence to:
D. P. Quinn,
davenquinn@caltech.edu

Citation:
Quinn, D. P., Saleeby, J. B., Ducea, M. N., Luffi, P., & Asimow, P. D. (2018). Late Cretaceous construction of the mantle lithosphere beneath the central California coast revealed by Crystal Knob xenoliths. *Geochemistry, Geophysics, Geosystems*, *19*, 3302–3346. https://doi.org/10.1029/2017GC007260

Received 26 SEP 2017
Accepted 5 MAY 2018
Accepted article online 23 JUN 2018
Published online 21 SEP 2018
Corrected 21 OCT 2018

This article was corrected on 21 OCT 2018. See the end of the full text for details.

Late Cretaceous Construction of the Mantle Lithosphere Beneath the Central California Coast Revealed by Crystal Knob Xenoliths

D. P. Quinn[1], J. B. Saleeby[1], M. N. Ducea[2,3], P. Luffi[4], and P. D. Asimow[1]

[1]Division of Geological and Planetary Sciences, California Institute of Technology, Pasadena, CA, USA, [2]Department of Geosciences, University of Arizona, Tuscon, AZ, USA, [3]Faculty of Geology and Geophysics, University of Bucharest, Bucharest, Romania, [4]Geological Institute of Romania, Bucharest, Romania

Abstract The Pleistocene (1.65 Ma) Crystal Knob volcanic neck in the California Coast Ranges is an olivine-plagioclase phyric basalt containing dunite and spinel peridotite xenoliths. Crystal Knob erupted through the Nacimiento belt of the Franciscan complex and adjacent to Salinian crystalline nappes. Its xenoliths sample the mantle lithosphere beneath the outboard exhumed remnants of the southern California Cretaceous subducting margin. This sample set augments previously studied xenolith suites in the Mojave Desert and Sierra Nevada, which linked the mantle lithosphere architecture and crustal structure of the western Cordillera. We examine six peridotite samples ranging from fertile lherzolites to harzburgite residues. Time-corrected (ϵ_{Nd}) of 10.3–11.0 and $^{87}Sr/^{86}Sr$ of 0.702 are characteristic of underplated suboceanic mantle. Pyroxene exchange geothermometry shows equilibration at 950–1060 °C. Phase stability, Ca-in-olivine barometry, and 65- to 90-mW/m^2 regional geotherms suggest entrainment at 45- to 75-km depth. The samples were variably depleted by partial melting, and re-enrichment of the hottest samples suggests deep melt-rock interaction. We test the Crystal Knob temperature depth array against model geotherms matching potential sources for the mantle lithosphere beneath the Coast Ranges: (A) a shallow Mendocino slab window, (B) a young Monterey plate *stalled slab*, and (C) Farallon plate mantle nappes, underplated during the Cretaceous and reheated at depth by the Miocene slab window. Models B and C fit xenolith thermobarometry, but only model C fits the tectonic and geodynamic evolution of southern California. We conclude that the mantle lithosphere beneath the central California coast was emplaced after Cretaceous flat slab subduction and records a thermal signature of Neogene subduction of the Pacific-Farallon ridge.

Plain Language Summary The Crystal Knob volcanic neck is a small, deeply sourced lava that erupted near in the California Coast Ranges 1.65 million years ago. It carried xenoliths, hand-sized fragments of the mantle, which can help us understand how the western edge of the North American continent was formed. We focused on six samples from Crystal Knob with different mineralogical characteristics, all of which originated in the mantle. Their chemistry suggests that they were not originally part of North America. Some xenoliths had been partially melted, and many had additional material added, changing their composition from pristine mantle. Mineral phases record their temperature (950–1060°C) and depth (45–75 km) prior to eruption. This rare direct record of the temperature of the upper mantle allows us to test several options for the formation of theunder pinnings of the central California coast. The most viable option is that the mantle beneath the edge of North America was tectonically pushed under the continent ~75 million years ago. It heated from below ~24 million years ago at the end of Farallon plate subduction. This history fits with extensive evidence that much of the deep architecture of the California coast is inherited from the Cretaceous period.

1. Introduction

The tectonic and petrogenetic processes by which Earth's continental mantle lithosphere develops through time are of fundamental importance to geodynamics and Earth history. The architecture of the mantle lithosphere, integrated with regional geophysical data and tectonic and petrogenetic studies of the overlying crust, offers critical insights into the geodynamic processes of continental assembly. Mantle xenoliths

entrained in volcanic rock reveal compositions and textures in a vertical transect through the underlying deep lithosphere. Petrogenetic studies of xenolith suites can discern their thermal conditions, depth of entrainment, and geochemical evolution. These features can provide insight into tectonic processes affecting the entire lithosphere.

The Crystal Knob xenolith suite, in the Coast Ranges of central California, presents a rare opportunity to sample the mantle lithosphere directly beneath a region of long-lived subduction accretion. The complex Late Cretaceous and Neogene tectonic processes that built the present Coast Ranges suggest several possible sources for the underlying mantle lithosphere. When restored for Neogene dextral offset, the position of Crystal Knob suggests that its upper mantle underpinnings may have been emplaced as asthenospheric mantle upwelling into the Pacific-Farallon slab window (Wilson et al., 2005). Other workers (e.g., Pikser et al., 2012) propose a shallowly dipping stalled slab beneath the Coast Ranges from the latest phase of subduction in Neogene time. We propose a third model, in which mantle lithosphere was underplated during Cretaceous extensional collapse after flat slab subduction (Chapman et al., 2012; Luffi et al., 2009). Given its position near the edge of the continent, this underplated lithospheric mantle would have experienced a thermal pulse due to Neogene ridge subduction (Wilson et al., 2005).

In this contribution, we present new petrologic, geochemical, and thermobarometric data on mantle xenoliths hosted in the Pleistocene Crystal Knob volcanic neck in coastal central California. These new data sets, plus derivative geochemical modeling and thermal modeling of the central California lithosphere, are used to decipher the petrogenesis of Crystal Knob xenoliths and host basaltic lavas. Constraints on the thermal structure of the mantle lithosphere are used to test the three models of the Late Cretaceous to present evolution of the lithospheric underpinnings of central California. The tectonic processes uncovered by this study can provide new insights into the relative role of Cretaceous and Neogene processes in building the margin of the North American continent.

1.1. Regional Tectonic Setting

The Crystal Knob xenolith locality samples an important lithospheric column through the Late Cretaceous convergent margin of the North American Cordillera. This regionally extensive belt includes a voluminous continental magmatic arc, generated as the Farallon oceanic plate subducted eastward beneath western North America (e.g., Ducea et al., 2015; Glazner, 1991), and the Franciscan complex, the crustal level accretionary complex of this subduction zone. The Franciscan includes tectonic slivers of Farallon plate oceanic basement and pelagic sedimentary rocks, as well as upper plate siliciclastic rocks derived from the magmatic arc (Blake et al., 1988; Chapman, 2016; Chapman et al., 2016; Cowan, 1978; Murchey & Jones, 1984; Sliter, 2004). The crystalline basement blocks of the *Salinian terrane*, or *Salinia* (Page, 1981), have recently been recognized as a series of nappes derived from the southern California segment of the Late Cretaceous magmatic arc, displaced westward to lie tectonically above the accretionary complex near the central California coast (Barth et al., 2003; Chapman et al., 2012; Ducea et al., 2009; Hall, 1991; Hall & Saleeby, 2013; Kidder & Ducea, 2006). The Crystal Knob xenolith locality lies along the western margin of Salinia, adjacent to the Nacimiento fault (Figure 1), a polyphase shear zone which, in its original geometry, constituted the local structural base of the Salinian crystalline nappe sequence (Hall & Saleeby, 2013). The Crystal Knob xenolith suite samples the uppermost mantle beneath the Franciscan accretionary complex and its local veneer of Salinia crystalline nappes.

Restoring the central Coast Ranges to their position relative to North America prior to San Andreas transform offset places them outboard of the southern California batholith, the extended southern continuation of the Sierra Nevada batholith in the Mojave Desert (Figure 1). In this restored position, the crystalline nappes that constitute Salinia correlate to deeply exhumed Cretaceous arc plutonic rocks of the southernmost Sierra Nevada batholith and northwestern southern California batholith (Barbeau et al., 2005; Chapman et al., 2012; Saleeby, 2003; Wood & Saleeby, 1997).

The southernmost Sierra Nevada batholith has been exhumed, with granitic rocks at the surface originating at shallow to medial crustal depths (2- to 4-kb pressure) in the bulk of the batholith grading toward deep crustal levels (10 kb) at its southernmost reaches (Ague & Brimhall, 1988; Nadin & Saleeby, 2008). Seismic imaging shows a strong reflector which is effectively flat beneath the western Mojave plateau (Yan et al., 2005) and dips ~30°N beneath the southernmost Sierra Nevada (Malin et al., 1995). This inflection aligns with increasing exhumation of the batholith and is interpreted as the relict megathrust surface, with a lateral ramp toward a *flat slab* beneath the Mojave province, atop which the southern California batholith was dispersed

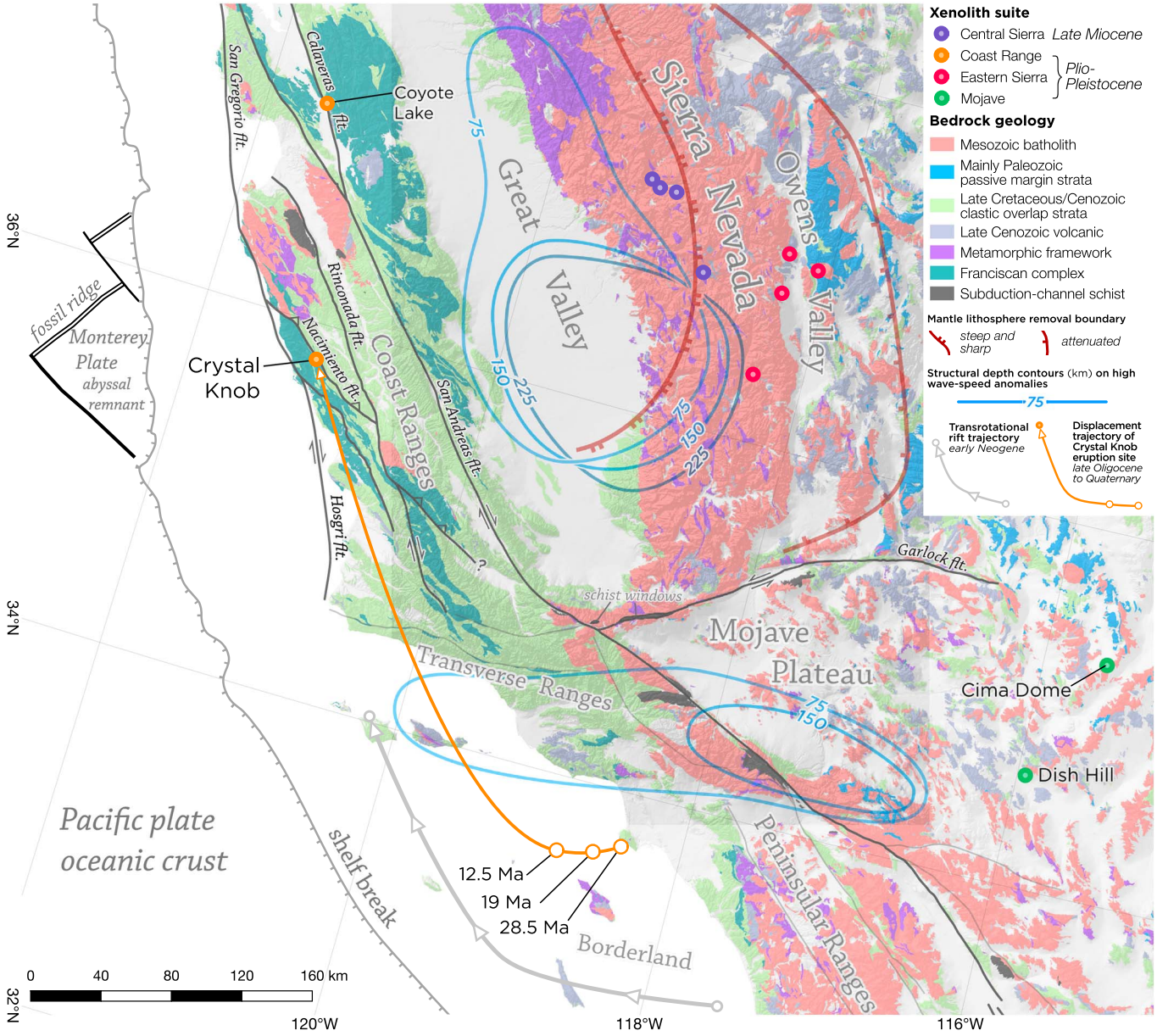

Figure 1. Map of southern California showing the tectonic setting of Crystal Knob and its placement relative to the dispersed Southern California batholith, Neogene dextral faults, and the stalled Monterey microplate. Sampling locations for previous xenolith studies are shown: the Central and Eastern Sierran suites show a record of delamination of a batholithic root (Ducea & Saleeby, 1996), and Mojave Plateau sites show underplating of Farallon plate lithospheric nappes during the Cretaceous (Luffi et al., 2009). The position of Crystal Knob is also shown, along with its North America relative position prior to dextral offset on the Neogene San Andreas transform system. Crystal Knob restores to ~350 km SE of its current location, with ~310-km displacement on the modern San Andreas Fault and ~40-km remainder on the Rinconada Fault. Independent reconstructions using the regional paleomagnetic framework of Wilson et al. (2005) and restoration of slip along San Andreas system faults (Dickinson et al., 2005) agree to within 5 km on the position of the Crystal Knob source locale at 19 Ma (see also Figure 17).

and truncated (Chapman et al., 2016; Saleeby, 2003). The 1) nucleated along this inflection during the early Miocene (Saleeby et al., 2016).

These exhumed batholithic rocks form the upper plate above a polyphase low-angle extensional fault system, remobilized in late Cretaceous time along the former shallow subduction megathrust. Franciscan affinity, mainly metaclastic rocks, were underplated beneath this tectonic surface (Barth et al., 2003; Chapman et al., 2010, 2012; Chapman, Wood, et al., 2016; Ducea et al., 2009; Malin et al., 1995; Saleeby, 2003; Yan et al., 2005). These subduction-channel schists are exposed in a series of tectonic windows (Figure 1) and encase blocks

and nappes of Farallon-plate oceanic basement and sedimentary rock. The schist protoliths were derived from the upper-plate batholithic belt, which was rapidly exhumed above a shallow flat segment of the Franciscan subduction megathrust system (Barth et al., 2003; Chapman, Jacobson, et al., 2016; Chapman et al., 2013; Saleeby et al., 2007). Truncation of lower crustal batholithic rocks and underplating of subduction channel schists require tectonic erosion of the underlying mantle wedge lithosphere and deepest arc crust.

Recent studies attribute the southern California flat slab to ephemeral buoyancy resulting from the subduction of the conjugate massif to the Shatsky Rise oceanic igneous province (Livaccari et al., 1981; Saleeby, 2003; Sliter, 2004), which is currently resolved in deep seismic tomographic images beneath the interior of North America (Liu et al., 2010; Sun et al., 2017). As the Shatsky conjugate moved deeper into the mantle beneath the North American plate, the Salinia nappes and adjacent (restored for Neogene dextral faulting) deeply exhumed batholithic rocks were displaced and structurally attenuated by both the shallow subduction megathrust and subsequent trench-directed extensional faulting (Chapman et al., 2012; Liu et al., 2010; Saleeby, 2003).

Later, Neogene ridge subduction and the opening of the Pacific-Farallon slab window (Atwater & Stock, 1998) drove far-field effects including late Cenozoic regional volcanism in central and southern California (Dodge, 1988) and the convective ascent of asthenosphere in the southern Basin and Range province (Le Pourhiet et al., 2006). Beginning in Miocene time, the crustal blocks through which Crystal Knob erupted were moved northwest along the San Andreas transform system to their present position (e.g., Argus & Gordon, 1991; Wilson et al., 2005).

1.2. Previous Mantle Xenolith Studies

The southwest North American Cordillera hosts many xenolith localities, at which upper mantle and lower crustal rock fragments were entrained in mainly late Cenozoic volcanic eruptions. Early studies of a number of these xenolith suites catalogued petrographic features and classified samples into textural groups (e.g., Nixon, 1987; Wilshire et al., 1988). Subsequently, modern geochemical and petrogenetic techniques have revealed several regional mantle lithosphere domains: Precambrian crustal root, Cretaceous arc mantle wedge, underplated Farallon plate nappes, and late Cenozoic shallow convective asthenosphere (e.g., Alibert, 1994; Beard & Glazner, 1995; Ducea & Saleeby, 1998b; Galer & O'Nions, 1989; Jové & Coleman, 1998; Lee, Rudnick, & Brimhall, 2001; Livaccari & Perry, 1993; Luffi et al., 2009; Usui et al., 2003).

The central Sierra Nevada xenolith suite (Figure 1) was entrained in late Miocene small-volume volcanic flows and plugs north of the zone of flat slab subduction. It samples the intact Sierra Nevada batholithic root and Cretaceous mantle wedge (Chin et al., 2015; Ducea & Saleeby, 1996, 1998b; Lee et al., 2006; Lee, Rudnick, & Brimhall, 2001; Saleeby, 2003). In contrast, xenolith suites in the eastern Mojave Desert record the partial tectonic erosion of subcontinental mantle lithosphere (including Cretaceous mantle wedge) and underplating of Farallon plate mantle lithosphere (Armytage et al., 2015; Luffi et al., 2009; Shervais et al., 1973; Shields & Chapman, 2016). The Dish Hill locality (Figure 1) records an upper mantle duplex with imbricated nappes of Farallon plate oceanic mantle lying structurally beneath a relatively thin roof of attenuated continental lithosphere peridotite. The mantle duplex is interpreted to have formed as the Farallon plate retreated following low-angle subduction of the Shatsky conjugate (Luffi et al., 2009).

Xenoliths of the eastern Sierra suite (Figure 1) occur in Pliocene-Quaternary mafic lava flows and record significantly steeper thermal gradients and more fertile compositions than the older xenoliths of the central Sierra, suggesting Neogene asthenospheric upwelling (Ducea & Saleeby, 1996, 1998a). Seismic studies show a corresponding domain of asthenospheric mantle that extends to the base of the crust (~30-km depth) in the eastern Sierra (Frassetto et al., 2011; Jones & Phinney, 1998; Jones et al., 2014; Zandt et al., 2004). The eruption of xenolith-hosting lavas of the eastern Sierra suite within the <5-Ma Owens Valley rift system (Figure 1) was likely driven by upper mantle convection (Le Pourhiet et al., 2006; Jones et al., 2014).

The upper mantle source of most xenolith suites in the Cordillera clearly corresponds to surface geology: subcontinental xenolith suites are generally erupted through cratonic and pericratonic crust, mantle wedge suites through the Cretaceous large-volume batholith, and asthenospheric suites through active rifts. However, xenoliths derived from underplated Farallon plate material have thus far only been recovered from inboard crustal domains in the eastern Mojave province. These lithospheric underpinnings were underplated with large subhorizontal displacements along a relatively shallow subduction megathrust system (Helmstaedt & Doig, 1975; Lee et al., 2001).

Figure 2. Cobble of Crystal Knob alkali basalt containing peridotite xenoliths.

Restored for Neogene dextral faulting, the lithospheric block hosting Crystal Knob was directly outboard of the Dish Hill xenolith locality (Figure 1), where the mantle lithosphere is formed by Farallon nappes underplated during Cretaceous time (Luffi et al., 2009). Accordingly, the mantle lithosphere beneath the Coast Ranges may be composed of outboard equivalents of these underplated nappes. However, subsequent Pacific-Farallon subduction and the slab window that developed during its early Neogene cessation may have also affected mantle lithosphere structure in the region. The Crystal Knob xenolith suite provides an opportunity to resolve the ambiguous mantle lithosphere architecture of coastal California and to understand the effects of flat slab subduction, microplate rotation and capture, and ridge subduction on the deep structure of a subducting margin.

2. The Crystal Knob Xenolith Locality

The Crystal Knob volcanic neck (35.806°N, 121.174°W) is a Pleistocene olivine-plagioclase phyric basalt that erupted along the margin of the Franciscan assemblage 500 m west of the Nacimiento Fault in the Santa Lucia Mountains of central California (Seiders, 1989). It was described in Wilshire et al. (1988) but not studied in detail. The basaltic plug is ~80 m in diameter at the surface and has entrained abundant dunite and sparse spinel peridotite xenoliths (Figure 2). The dunites have textural features typical of igneous cumulates, and olivine aggregates decrease in size to single grain xenocrysts, which are visually indistinguishable from phenocrysts in the basalt groundmass. Sparse spinel peridotites, lacking textures suggestive of cumulate origin, are also present. In conjunction with the compositional data presented below, we interpret the peridotites as entrained fragments of the mantle lithosphere.

Samples were collected from the Crystal Knob basalt with an emphasis on the polyphase peridotite xenoliths. Xenolith samples are 5- to 10-cm diameter friable peridotites with 200-μm to 1-mm grains. Additionally, samples of the host basalt and dunite cumulates were collected to establish context for the xenoliths.

2.1. Petrographic and Analytical Methods

Polished thin sections of 30-μm thickness were prepared for six peridotite xenolith samples (CK-2 through CK-7) and the basalt host lava (CK-1). The xenolith samples were bound with epoxy prior to sectioning. Large-format rectangular thin sections were pared for two dunite cumulate samples hosted in basalt (CK-D1 and CK-D2). The samples were evaluated under a petrographic microscope to identify characteristic textural and mineralogic features (Table 1 and Figure 3).

Electron backscatter intensity images of each thin section were collected using a ZEISS 1550 VP field emission scanning electron microscope at the California Institute of Technology. These were coregistered with optical scans and electron-microprobe analysis points using an affine transformation between fixed stage coordinates. Modal mineralogy was mapped on a grid atop these aligned data sets (Figure 4).

Major element compositions were measured on polished thin sections with a five-spectrometer JEOL JXA-8200 electron-probe microanalyzer at the California Institute of Technology. Abundances were counted in wavelength dispersive mode using a 15-kV accelerating potential, a focused 25-nA beam, and counting times of 20 s on peak and 10 s off peak. The instrument was calibrated using natural and synthetic standards; matrix corrections were made using the CITZAF (Armstrong, 1988) algorithm. We performed 1,714 measurements across the six peridotite samples, concentrated in 3–4 locations of interest per sample emphasizing areas with orthopyroxene and clinopyroxene in contact to aid in thermometry. We also took 403 measurements of the basaltic host and entrained dunites (Table 2).

Table 1
Summary of Petrographic Data

Sample	Type	Notes
CK-1	Basalt	Host lava containing phenocrysts, xenocrysts, and <1-cm xenolith fragments (Figure 3a)
CK-2	Lherzolite	Fertile lherzolite with pristine textural features
CK-3	Harzburgite	Depleted harzburgite with the largest crystals in the sample set and small equant spinels
CK-4	Harzburgite	Most affected by post-formation melting, with grain boundary melt veins containing 10- to 50-μm aggregates of equant amphibole and other phases
CK-5	Harzburgite	Relatively depleted sample but with more clinopyroxene than CK-3
CK-6	Lherzolite	Fertile, with abundant spinel, large intergrown crystals and recrystallized aggregates of orthopyroxene and clinopyroxene; small-scale, vermicular intergrowth of clinopyroxene within orthopyroxene
CK-7	Lherzolite	Somewhat altered, with small-volume melt veins but without growth of microcrystalline aggregates (as in CK-4)
CK-D1	Dunite	Host lava containing dunite and peridotite xenolith fragments Peridotite fragments contain petrographic exsolution lamellae of clinopyroxene within orthopyroxene (Figure 3c)
CK-D2	Dunite	Host lava containing dunite and peridotite xenolith fragments

Minerals were automatically assigned for microprobe measurements using a nearest-neighbor fitting algorithm between pure end member phases. These analyses were aligned with optical and backscatter imagery and checked for consistency: poor-quality measurements with low totals were automatically flagged for removal (Taylor, 1998), and mixed phases along grain boundaries were discarded on a case-by-case basis.

Additional isotope and trace element geochemical techniques applied to the harzburgite and lherzolite samples are discussed throughout section 2.4.

2.2. The Basaltic Host

The Crystal Knob hxenoliths are hosted by an alkali basalt containing sparse vesicles and abundant plagioclase feldspar, potassium feldspar, clinopyroxene, and olivine phenocrysts. Sample CK-1 of the basaltic host contains dunite and multiphase peridotite fragments ranging from aggregates of a few grains to ~5-cm xenoliths. The groundmass is dominated by altered glass and abundant microphenocrysts of potassium and plagioclase feldspar. Though dominantly black, it is mottled with greenish-gray alteration color domains at ~500-μm scale. These domains are crosscut by elongate narrow (~1 mm) shear bands of finer-grained material with sparse vesicles and phenocrysts.

Petrographic study of dunite fragments within the Crystal Knob basalt reveals residues from multiple stages of melt fractionation. Thin sections CK-D1 and CK-D2 contain dunite and peridotite fragments up to 2 cm in diameter within a basaltic groundmass. The peridotite fragments show textures similar to the polyphase peridotite samples (CK-2 to CK-7). The dunite fragments have textures typical of cumulate residues: finer-grained than the peridotites, they contain a mosaic of closely packed 50-200 μm olivine grains with melt filling intergrain spaces. Some dunite encases peridotite fragments containing large (up to 2 mm) grains of olivine, pyroxene, and spinel. CK-D1 notably contains a large, pitted, spinel grain embedded in dunite. These dunite cumulates are texturally representative of the majority of xenoliths in the Crystal Knob basalt.

Clinopyroxene in the basalt groundmass is separated into two compositional groups: some phenocrysts show an average Mg# of ~76 (Mg# defined as molar Mg/(Mg+Fe) · 100). A separate group of high-Mg# clinopyroxenes (up to Mg# 91) are hosted in xenolith fragments and cores of zoned single grains. Concentrically zoned clinopyroxene grains with high-Mg# cores up to 300 μm in diameter (Figure 5) record multistage

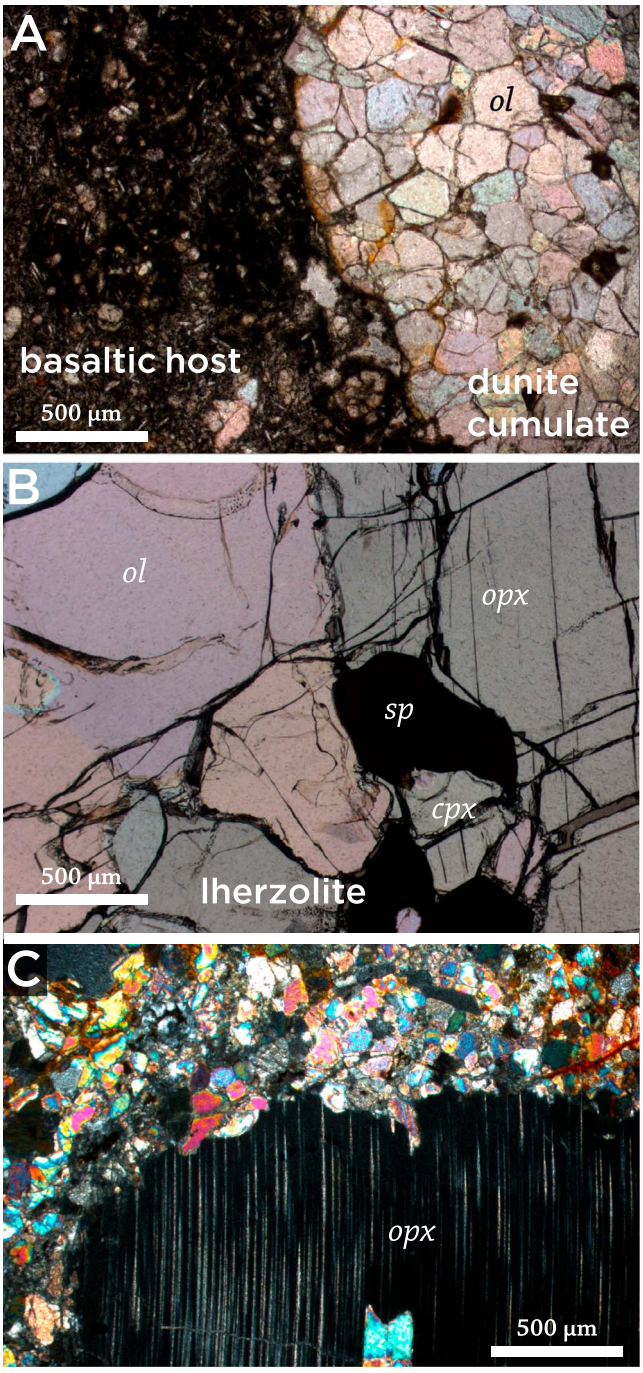

Figure 3. Optical petrographic images (2.5-mm wide field of view) showing characteristic textures of the xenolith samples and basaltic host. (a) Sample CK-D2, with the edge of a cumulate xenolith composed of equant olivine (ol) grains (200 μm characteristic scale) set against a host lava groundmass containing <100-μm phenocrysts of olivine, pyroxene, and plagioclase feldspar. (b) The spinel lherzolite sample CK-4 with >2-mm olivine, orthopyroxene (opx), clinopyroxene (cpx), and spinel (sp). (c) Sample CK-D2, with a single large orthopyroxene crystal with augite exsolution lamellae and containing an olivine inclusion juxtaposed against dunite cumulate material consisting of mosaic-textured olivine grains.

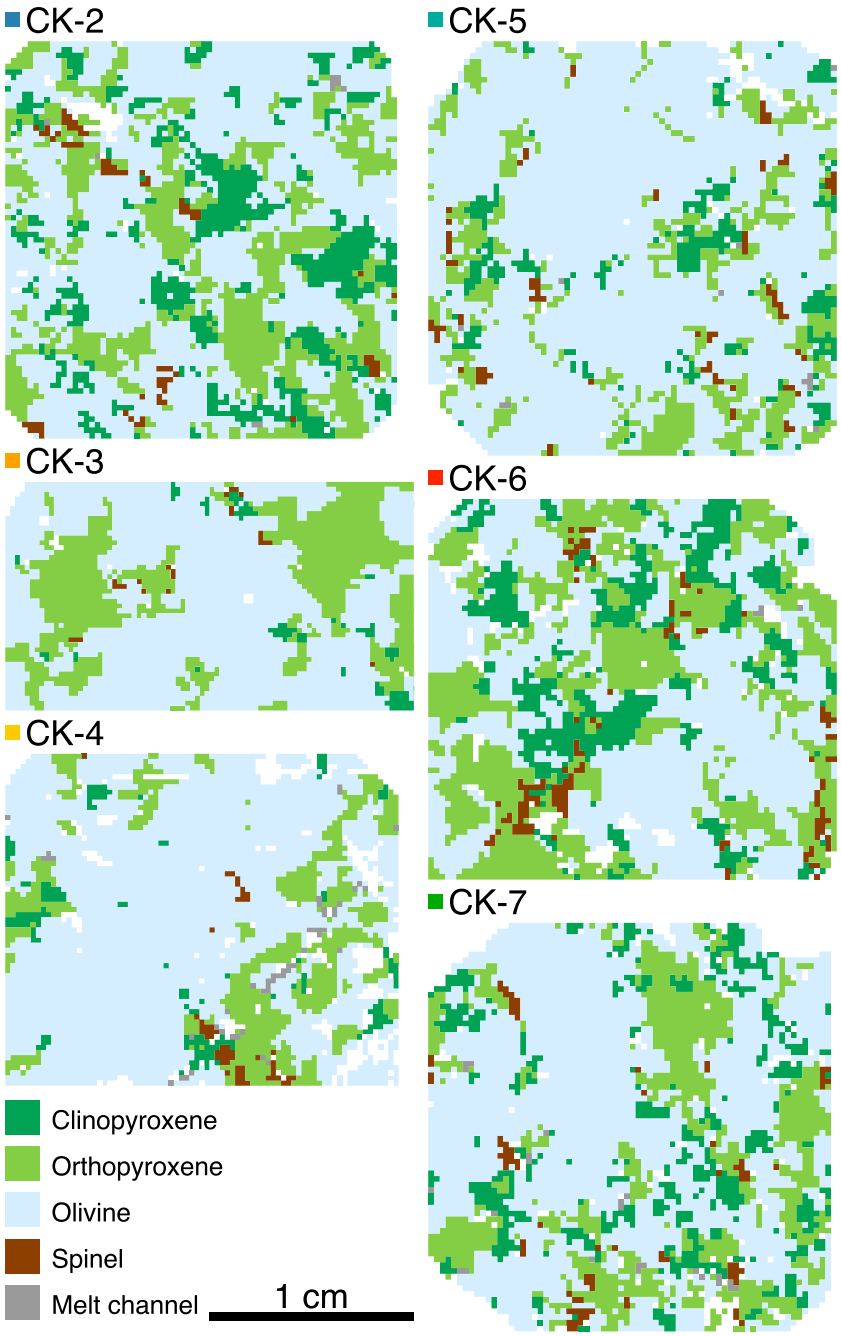

Figure 4. Mineral classification images of each sample (1″ round thin section) created manually atop coregistered electron backscatter and optical imagery, showing the textural variation within Crystal Knob spinel peridotites. The variable clinopyroxene abundances correspond to fertility. A melt channel cutting diagonally across the bottom-right quadrant of CK-4 (dark gray line) is the most significant textural signature of late-stage melt interaction in the sample set. These classifications form the basis of recalculated modal abundances (Figure 8).

crystallization in a progressively evolving magma, and thin, low-Mg# rims suggest that the last phase of fractionation likely occurred during magma ascent and cooling.

Olivine grains in the host lava sample a range from fertile lherzolite major element compositions (Mg# ≈ 89) through progressively lower Mg#, with cumulate aggregates clustered at Mg#=68 (Figure 6a). We suspect that the olivine grains in the basalt represent both fragments of the mantle source (xenocrysts, possibly mechanically separated from entrained peridotites) and cumulates that crystallized at various stages of melt evolution.

Table 2
Xenolith and Host Lava Major Element Compositional Data

Sample	SiO_2	FeO	MgO	TiO_2	Al_2O_3	Na_2O	CaO	MnO	Cr_2O_3	NiO	K_2O	Total	*n*	Mg#	Cr#
A. Xenolith mineral composition												Average of *n* measurements, oxide wt%			
Olivine															
CK-2	40.78	9.90	49.08	0.01	0.01	0.01	0.07	0.14	0.01	0.35	—	100.36	48	89.84	—
CK-3	41.00	9.45	49.77	0.02	0.02	0.01	0.10	0.13	0.03	0.35	—	100.88	52	90.37	—
CK-4	40.86	9.06	49.75	0.03	0.03	0.01	0.11	0.13	0.02	0.35	—	100.35	84	90.73	—
CK-5	41.35	10.04	49.41	0.02	0.01	0.00	0.07	0.14	0.01	0.34	—	101.39	28	89.76	—
CK-6	40.72	11.61	48.04	0.02	0.02	0.01	0.11	0.15	0.02	0.30	—	100.99	33	88.06	—
CK-7	40.98	10.47	48.85	0.01	0.01	0.00	0.08	0.15	0.01	0.35	—	100.92	44	89.26	—
Orthopyroxene															
CK-2	54.62	6.42	32.45	0.12	4.65	0.10	0.82	0.14	0.35	0.08	—	99.73	97	90.02	4.79
CK-3	54.97	6.17	32.83	0.12	4.30	0.12	1.11	0.13	0.63	0.09	—	100.45	105	90.46	8.90
CK-4	55.08	5.86	32.90	0.09	3.98	0.11	1.14	0.13	0.67	0.09	—	100.05	134	90.92	10.20
CK-5	55.67	6.49	32.84	0.13	4.63	0.11	0.89	0.14	0.34	0.08	—	101.32	66	90.02	4.69
CK-6	54.43	7.54	31.52	0.12	4.83	0.12	1.11	0.15	0.51	0.08	—	100.41	63	88.17	6.60
CK-7	54.97	6.85	32.54	0.11	4.74	0.11	0.90	0.15	0.36	0.09	—	100.83	68	89.43	4.83
Clinopyroxene															
CK-2	51.41	3.23	15.10	0.51	6.83	1.60	19.95	0.09	0.74	0.04	—	99.51	102	89.27	6.81
CK-3	52.09	3.35	16.34	0.29	5.77	1.33	19.73	0.09	1.19	0.04	—	100.23	115	89.68	12.12
CK-4	51.88	3.19	16.51	0.36	5.37	1.16	19.99	0.09	1.20	0.04	—	99.78	86	90.22	13.23
CK-5	52.39	3.21	15.14	0.60	7.03	1.70	20.08	0.09	0.74	0.04	—	101.02	70	89.38	6.62
CK-6	51.81	4.14	15.83	0.39	6.45	1.35	19.32	0.10	0.96	0.04	—	100.39	53	87.21	9.07
CK-7	51.93	3.55	15.40	0.45	6.81	1.58	19.87	0.09	0.74	0.05	—	100.47	69	88.55	6.83
Spinel															
CK-2	0.04	11.54	20.42	0.09	56.26	0.01	0.00	0.11	9.23	0.36	—	98.06	23	75.92	9.92
CK-3	0.04	13.49	18.89	0.16	45.03	0.01	0.00	0.16	20.22	0.28	—	98.29	28	71.40	23.15
CK-4	0.05	13.53	17.66	0.39	42.48	0.00	0.00	0.16	22.05	0.28	—	96.62	26	69.94	25.84
CK-5	0.03	11.58	20.59	0.12	57.74	0.00	0.00	0.12	9.21	0.34	—	99.74	11	76.02	9.67
CK-6	0.06	15.85	18.38	0.20	49.63	0.01	0.00	0.15	14.70	0.29	—	99.27	14	67.40	16.57
CK-7	0.04	12.61	20.24	0.10	55.82	0.00	0.00	0.13	9.97	0.35	—	99.26	8	74.10	10.70
B. Host lava (CK-1) mineral composition												Representative measurement, oxide wt%			
Potassium feldspar															
Groundmass	64.09	0.47	0.00	0.25	21.26	6.50	1.50	0.01	0.00	—	6.29	100.37	—	1.37	—
Plagioclase feldspar															
Groundmass	54.71	0.82	0.01	0.26	27.79	5.27	10.41	0.02	0.01	—	0.30	99.60	—	2.47	—
Olivine															
Xenocryst	41.63	9.20	48.94	0.01	0.00	0.01	0.09	0.13	0.01	—	0.00	100.02	—	90.46	—
Phenocryst	37.64	28.29	32.67	0.01	0.00	0.01	0.32	0.80	0.00	—	0.00	99.73	—	67.31	—
Clinopyroxene															
Xenocryst	47.81	9.04	11.84	2.57	5.31	0.64	22.42	0.23	0.00	—	0.00	99.88	—	70.01	—
Phenocryst	51.03	6.85	14.63	1.07	5.59	0.72	19.94	0.20	0.17	—	0.00	100.20	—	79.19	—
C. Xenolith whole-rock composition *recalculated from mineral modes*												Normalized oxide wt%			
CK-2	45.04	8.26	40.84	0.10	2.19	0.23	2.73	0.13	0.22	0.25	—	100	—	89.73	—
CK-3	44.28	8.50	44.77	0.04	1.20	0.05	0.54	0.13	0.21	0.28	—	100	—	90.37	—
CK-4	43.80	8.23	45.15	0.05	1.12	0.05	0.72	0.13	0.26	0.28	—	100	—	90.50	—
CK-5	43.01	9.13	44.83	0.06	1.25	0.09	1.04	0.13	0.13	0.29	—	100	—	89.68	—
CK-6	45.54	9.46	38.59	0.09	2.79	0.19	2.56	0.15	0.44	0.20	—	100	—	87.78	—
CK-7	43.94	9.06	41.98	0.07	1.93	0.18	2.15	0.14	0.21	0.27	—	100	—	89.05	—

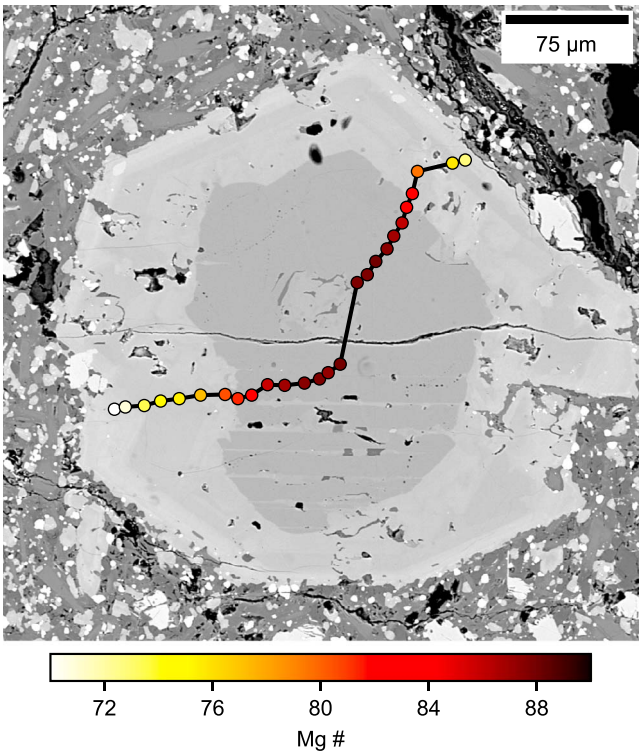

Figure 5. Profile of Mg# measured across clinopyroxene phenocryst in the host lava sample CK-1. The grain has a partially cannibalized and fractured xenocryst core with a Mg# of ~90, surrounded by successive layers with lower Mg#, with Mg# 75 material in the outermost 30 µm of the grain.

2.3. Eruptive Age

The age of lavas hosting mantle xenolith suites is required to link their petrogenesis to tectonic and geodynamic processes (e.g., Ducea & Saleeby, 1998a). The age of the Crystal Knob host lava was determined using the $^{40}Ar/^{39}Ar$ technique on phenocryst plagioclase. A billet of the host lava (sample CK-1) containing visible plagioclase lathes was provided to the USGS Geochronology Laboratory in Denver, Colorado. The sample was irradiated in the USGS TRIGA reactor, and plagioclase feldspar grains were step heated in situ using an infrared laser. Loss of ^{39}Ar was measured simultaneously on a Thermo Scientific Argus VI using four Faraday detectors (m/e 40-37) and ion counting (m/e 36). The detectors were intercalibrated using standard gas and air pipettes. The measurements are corrected for blanks above baselines, radioactive decay, and nucleogenic interferences and standardized against a Fish Canyon sanidine with an age of 28.20 Ma. Nonradiogenic argon is assumed to have an atmospheric composition of $^{40}Ar/^{39}Ar = 298.56$ (Cosca et al., 2011).

Step-heating data are presented in Table 3 and shown graphically in Figure 7. Our preferred age of 1.65 ± 0.06 Ma (2σ) is defined by the 12 intermediate of 15 heating steps. The entire spectrum defines a similar age, within error, of 1.71 Ma. We infer that the xenoliths were entrained from the upper mantle directly beneath the Crystal Knob volcanic pipe during the mid-Pleistocene.

2.4. Spinel Peridotite Xenoliths

2.4.1. Petrography

The spinel peridotite xenoliths (CK-2 through CK-7) are texturally classified using the scheme of Pike and Schwarzman (1977). All samples display a xenomorphic texture with anisotropy largely absent. Most samples have minor plastic deformation features, including slight kink bands in some olivine crystals. However, small (~1°) axial rotations between large subgrain crystal domains suggest little to no strain. Samples CK-2 and CK-5 exhibit a weak shape-preferred alignment in elongate spinels (Figure 4).

Minor late-stage alteration is seen in all peridotite samples. This includes variably Fe-rich grain boundaries of major phases and Ti enrichment in pyroxene rims (<10 µm from the grain edge). Sample CK-4 contains a thin melt channel that cuts linearly across the thin section (Figure 4). This channel is bounded by resorbed edges of the major phases (olivine and orthopyroxene) and hosts microcrystalline clinopyroxene, 10-µm-scale euhedral

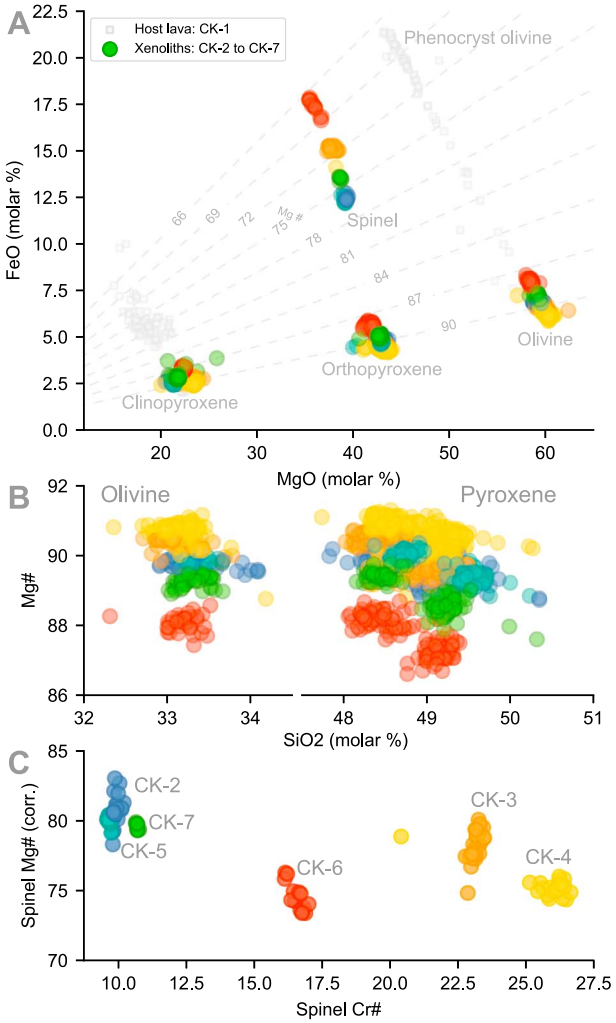

Figure 6. Major element compositional data for the Crystal Knob spinel peridotites and host lavas. The data are colorized by sample in a consistent scheme used in Figure 15. (a) FeO versus MgO measured by electron microprobe for grain cores, showing range in major element depletion between samples. Dotted lines show Mg# levels. (b) Mg# (total iron basis) versus SiO2 for the silicate phases in the Crystal Knob peridotite xenoliths. This shows the range in major element depletion between samples, including the low Mg# of CK-6, the most fertile sample. (c) Spinel Cr# versus Mg# (corrected based on cation charge balance) showing grouping of samples by Cr content, corresponding to different levels of depletion. The highest-Cr samples (CK-3 and CK-4) are harzburgite residues. Colors are by sample as labeled in (c).

spinels, and minor amphibole. Near this melt channel, thin intergranular streamers are enriched in Na and Ti. This grain boundary melt infiltration is less extensive in sample CK-3 and not present in other samples.

Clinopyroxene and orthopyroxene grains form interlocking crystal domains in all samples. This is most apparent in CK-3 and CK-4, where sparse clinopyroxene is always adjacent to orthopyroxene. Sample CK-7 shows minor exsolution lamellae of orthopyroxene and clinopyroxene. Peridotite fragments in CK-D1 show abundant pyroxene exsolution lamellae (Figure 3c), and sample CK-6 shows similar vermicular pyroxene exsolution. CK-6 also contains unique composite pyroxenes, with fused domains marked by substantially different crystal-axis orientations.

2.4.2. Compositions of Dominant Phases

Major element abundances for the peridotite xenoliths were measured by electron microprobe using methods discussed in section 2.1. Results are summarized in Table 2a and Figure 6. Generally, phase compositions show tight per sample groupings, which suggest equilibrium within each sample. The major silicate phases show Mg# > 87, consistent with fertile or residual mantle compositions. Variations in Mg# between samples indicate differences in melt extraction and refertilization history between the samples.

Table 3
Step-Heating Data for Ar Geochronology

Step	Power W	$\frac{^{36}Ar}{^{39}Ar} \times 10^3$	$\frac{^{37}Ar}{^{39}Ar}$	$\frac{^{38}Ar}{^{39}Ar} \times 10^2$	$\frac{^{40}Ar}{^{39}Ar}$	^{39}Ar mol $\times 10^{-12}$	^{39}Ar %	$\frac{Ca}{K}$	$\frac{^{40}Ar*}{^{39}Ar}$	$^{40}Ar*$ %	Age Ma
1	1.25	13.54 (42)	0.397 (22)	3.9 (2.9)	4.97 (13)	1.07	0.471	2.87 (16)	1.041 (79)	20.93	2.00
2	1.5	5.116 (52)	0.3354 (27)	2.60 (39)	2.4085 (85)	8.21	3.624	2.429 (20)	0.976 (15)	40.52	1.88
3	1.75	0.927 (21)	0.2368 (16)	2.28 (25)	1.0901 (25)	13.36	5.898	1.716 (12)	0.8805 (66)	80.77	1.69
4	2	0.871 (19)	0.2218 (17)	2.56 (23)	1.0966 (27)	14.36	6.339	1.608 (12)	0.8995 (61)	82.03	1.73
5	2.25	1.284 (17)	0.2037 (12)	2.17 (20)	1.1963 (24)	16.82	7.427	1.4770 (90)	0.8707 (54)	72.79	1.67
6	2.5	1.668 (20)	0.2052 (13)	1.50 (20)	1.2988 (26)	16.22	7.161	1.4882 (94)	0.8586 (61)	66.11	1.65
7	2.75	1.167 (20)	0.2297 (16)	1.28 (24)	1.1311 (27)	13.48	5.952	1.666 (12)	0.8474 (64)	74.92	1.63
8	3	1.124 (22)	0.2570 (22)	0.84 (27)	1.0963 (33)	11.84	5.228	1.865 (16)	0.8331 (72)	75.98	1.60
9	3.5	1.252 (23)	0.3368 (22)	0.98 (28)	1.1016 (31)	11.25	4.968	2.445 (16)	0.8228 (73)	74.67	1.58
10	4	1.905 (33)	0.4860 (34)	0.70 (40)	1.2635 (49)	8.01	3.537	3.529 (25)	0.832 (10)	65.82	1.60
11	4.5	2.020 (42)	0.6755 (46)	0.57 (51)	1.2690 (50)	6.23	2.749	4.906 (33)	0.857 (13)	67.46	1.65
12	5	3.274 (33)	0.7668 (28)	1.04 (28)	1.5669 (40)	11.49	5.073	5.571 (20)	0.806 (10)	51.41	1.55
13	6	3.288 (27)	0.8220 (22)	1.04 (20)	1.6034 (33)	16.30	7.199	5.974 (16)	0.8549 (82)	53.25	1.64
14	8	4.072 (17)	0.89534 (91)	1.306 (82)	1.8180 (15)	42.65	18.831	6.5083 (66)	0.8563 (53)	47.04	1.65
15	10	4.701 (36)	1.1287 (31)	1.28 (24)	2.1567 (51)	13.23	5.844	8.207 (23)	1.074 (11)	49.70	2.06
16	15	6.048 (30)	1.2869 (21)	1.53 (15)	2.4689 (35)	21.97	9.701	9.360 (15)	1.0291 (90)	41.59	1.98

Samples CK-2, CK-5, and CK-7 cluster tightly in Fe-Mg space, with relatively low Mg#s indicative of fertile compositions similar to average depleted mantle (Workman & Hart, 2005). Silicate phases in CK-3 and CK-4 have Mg# > 90, suggesting a residual composition. Sample CK-6 has low Mg#s for all major phases, with values as low as 87 for clinopyroxenes. All phases in this sample show higher iron abundance than expected for fertile peridotites.

Based on measured phase composition, we correct spinel Mg# from total iron to ferrous iron basis using charge balance on a four-oxygen basis. This correction results in spinel Mg# between 75 and 81, slightly higher than the uncorrected value (Table 4). Some samples, particularly CK-2, have scatter in corrected Mg# due to

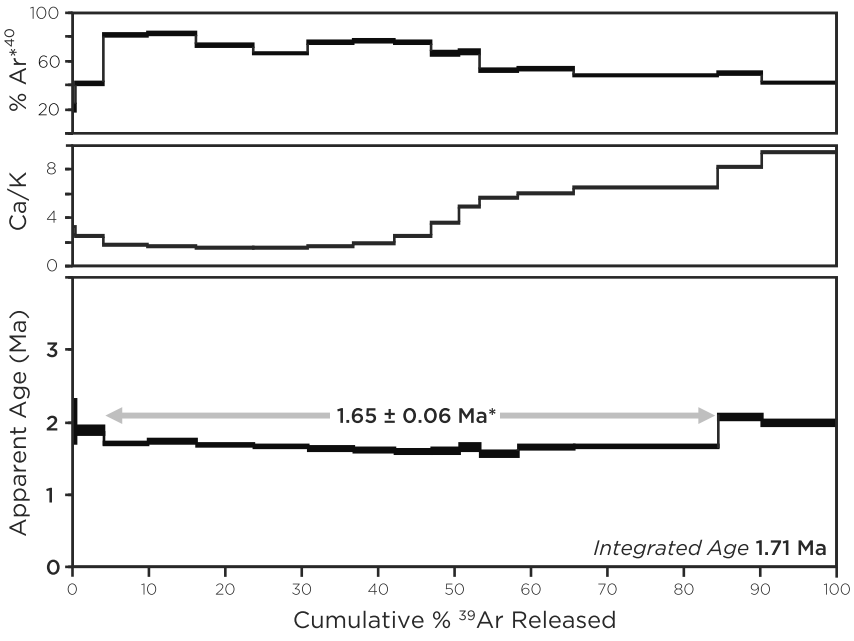

Figure 7. Step-heating results for $^{40}Ar/^{39}Ar$ dating of the Crystal Knob host basalt, with a broad plateau for 1.65 Ma and an average of 1.71 Ma.

Table 4
Spinel Ferric Iron Content[a]

Sample	Fe^{2+}	Fe^{3+}	Fe^{3+}/Σ Fe	Mg#[b]	Mg#[c]	*n*
CK-2	0.19	0.06	0.25	75.9	80.8	23
CK-3	0.22	0.10	0.31	71.4	78.3	28
CK-4	0.24	0.08	0.24	69.9	75.3	26
CK-5	0.20	0.05	0.21	76.0	80.0	11
CK-6	0.25	0.10	0.29	67.4	74.5	14
CK-7	0.20	0.07	0.27	74.1	79.6	8

[a]Estimated from cation site balance. [b]Using $Fe^{2+} = \Sigma$ Fe. [c]Corrected.

unmeasured transition metals (e.g. Zn, Co, and V) that are common in oxide minerals. A range of spinel Cr# (molar Cr/(Cr+Al) · 100) from 10 for the fertile samples to 22–27 for CK-3 and CK-4 implies variation in degree of partial melting. Sample CK-6 has an intermediate spinel Cr# (Figure 6c).

2.4.3. Modal Mineralogy

The spinel peridotite samples are dominated by olivine and orthopyroxene, and quantitative modal abundances were measured by mapping phases on a 5,000-point grid atop coregistered optical scans and electron backscatter mosaics (Figure 4). Volumetric modes were converted to weight percent using representative densities for spinel facies peridotite phases given in Nesse, (2000; Table 5).

Modal abundance data show a range in lithology from lherzolites to clinopyroxene harzburgites (Figure 8). All samples contain minor (<1%) spinel. The samples span a range of clinopyroxene content from 12.2% for the fertile lherzolite CK-2 to 0.91wt% for the depleted harzburgite CK-3. The harzburgites have larger grains (500 μm characteristic scale) than the lherzolites (~200 μm), and CK-3 contains 2-mm orthopyroxene crystals. All samples are Type I peridotites in the Frey and Prinz (1978) classification system.

2.4.4. Whole-Rock Composition

Whole-rock major element abundances are reconstructed from averaged mineral composition and estimated modes. Representative mineral compositions are given in Table 2a and recalculated whole-rock compositions in Table 2c. Whole-rock Mg# ranges from 87 to 91. Within each sample, a consistent Mg# for all silicate phases (Figure 6) is indicative of Fe-Mg equilibrium. All samples contain <1wt% spinel, with Mg# variation mirroring that of the silicate phases.

Samples CK-2, CK-5, and CK-7 have Mg# between 89 and 90 (both for individual silicate phases and reconstructed whole-rock measurements). CK-3 and CK-4 have a whole-rock Mg# > 90. CK-6 has a whole-rock Mg# < 88 and contains substantially more Cr, Al, and Fe than the other samples. Though CK-6 is generally the most enriched in incompatible elements, sample CK-2 contains somewhat more Ca and Na. Both of these samples have fertile major element compositions.

2.4.5. Discussion of Peridotite Composition

The coincident low Mg# and spinel Cr# of the lherzolite samples CK-2, CK-5, and CK-7 imply that they are fertile to partially depleted peridotites, with low melt volumes extracted (assuming no refertilization). These samples contain consistently fertile phases (Mg# of ~89), with variation in whole-rock composition coupled primarily

Table 5
Recalculated Modal Mineralogy[a]

Sample	Olivine	Orthopyroxene	Clinopyroxene	Spinel	Alteration
CK-2	64.29	22.79	12.45	0.46	0.02
CK-3	73.61	25.33	0.97	0.09	0.00
CK-4	76.10	21.44	1.93	0.31	0.22
CK-5	81.13	13.99	4.32	0.53	0.04
CK-6	56.11	31.67	11.14	1.07	0.00
CK-7	71.02	18.45	9.74	0.71	0.07

[a]wt% based on Nesse (2000) phase densities.

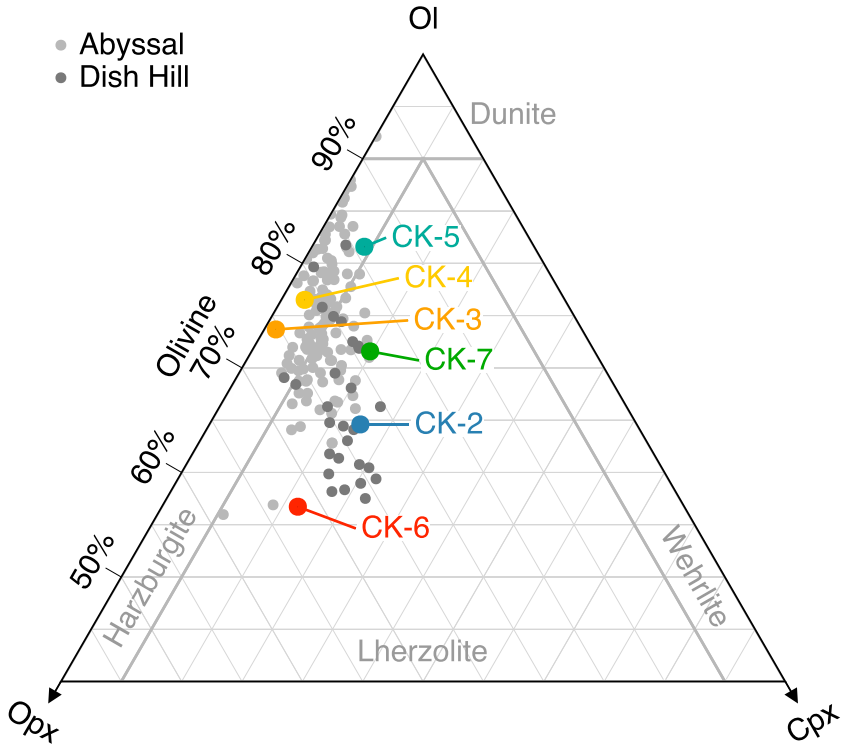

Figure 8. Modal composition of Crystal Knob peridotites. Abyssal (Asimow, 1999; Baker & Beckett, 1999) and Dish Hill (Luffi et al., 2009) peridotite compositions are shown for comparison.

to changing phase abundances: the samples show a range in olivine abundance from 65 to 75wt% (Figure 8) without adjustment in equilibrium phase compositions, suggesting low to moderate levels of depletion.

The harzburgite samples CK-3 and CK-4 contain high-Cr# spinels and high Mg# (>90) silicate phases. These features, along with low (<2%) clinopyroxene modes, are typical of residues of high-degree partial melting. The depleted phase compositions and abundance of refractory Cr in spinel indicate almost-complete removal of incompatible lithophile elements (Dick & Bullen, 1984).

CK-6 is a clear anomaly: high-iron phase compositions (Figure 6b), low whole-rock Mg#, and high clinopyroxene modal abundances (Figure 8) are markers of fertility, but intermediate spinel Cr# and abundant orthopyroxene are typical of depleted residues. We propose a two-stage history, where the highly fertile major element composition of CK-6 was gained by assimilation of a fractionated, Fe-rich melt into a partially depleted residue. In this case, excess pyroxene would have formed due to the addition of silica to an olivine-rich residual assemblage, and the relatively chromian spinels represent a prerefertilization vestige. We explore the potential depletion and re-enrichment of these samples further in section 2.6.1.

Table 6
Radiogenic Isotope Measurements

Sample	Sm	Nd	$\frac{^{147}Sm}{^{144}Nd}$	$\frac{^{143}Nd}{^{144}Nd_{[0]}}$	$\Delta t \times 10^6$	ϵ_{Nd}	T_{CHUR}	Rb	Sr	$\frac{^{87}Rb}{^{86}Sr}$	$\frac{^{87}Sr}{^{86}Sr_{[0]}}$	$\Delta t \times 10^7$
CK-2	1.388	2.994	0.28041	0.51319	−3.03	10.69	1.00	0.055	42.704	0.00370	0.70237	−0.85
CK-3	1.783	3.988	0.27031	0.51317	−2.92	10.34	1.10	0.342	49.802	0.01976	0.70235	−4.53
CK-4	1.087	2.539	0.25877	0.51320	−2.79	10.99	1.38	0.058	41.610	0.00403	0.70232	−0.92
CK-5	1.313	3.335	0.23799	0.51318	−2.57	10.57	1.99	0.354	52.082	0.01956	0.70231	−4.49
CK-6	1.470	3.285	0.27053	0.51317	−2.92	10.46	1.10	0.135	38.320	0.01009	0.70242	−2.31
CK-7	0.482	1.105	0.26379	0.51317	−2.85	10.42	1.21	0.092	13.665	0.01934	0.70237	−4.44

Note. Δt is a time correction of the preceding measured isotope ratio to eruptive conditions (t = 1.65 Ma).

Table 7
Trace Element Abundances (ppm)

Sample	La	Ce	Pr	Nd	Sm	Eu	Gd	Tb	Dy	Ho	Er	Tm	Yb	Lu	*n*
Clinopyroxene															
CK-2	1.09	2.70	4.47	7.18	10.98	11.33	12.21	13.79	14.18	14.25	14.33	12.45	14.27	13.29	3
CK-3	9.05	8.03	6.46	6.09	6.57	4.80	8.07	8.04	8.52	8.49	8.40	6.61	8.43	4.96	3
CK-4	15.89	11.10	8.69	7.39	5.14	5.05	4.85	3.97	5.17	6.10	5.53	5.72	6.56	5.56	2
CK-5	12.18	12.23	11.73	12.35	12.84	13.66	14.24	15.51	15.43	16.38	14.97	14.62	15.78	11.94	2
CK-6	6.60	6.72	6.41	7.78	9.35	10.77	11.17	12.08	11.81	12.02	10.83	10.67	11.44	9.31	3
CK-7	5.24	5.76	7.33	9.02	12.38	17.48	13.15	16.08	14.25	14.68	13.49	13.44	14.99	11.20	2
Orthopyroxene															
CK-2	0.00	0.01	0.02	0.03	0.10	0.48	0.21	0.31	0.50	0.58	0.78	1.07	1.55	1.87	3
CK-3	0.04	0.03	0.04	0.04	0.10	0.20	0.15	0.22	0.38	0.53	0.67	0.74	0.95	1.11	4
CK-4	0.10	0.13	0.19	0.19	0.23	0.27	0.26	0.26	0.38	0.44	0.64	0.66	1.08	1.00	2
CK-5	0.02	0.03	0.05	0.07	0.11	0.08	0.21	0.38	0.46	0.66	0.83	0.96	1.59	1.90	2
CK-6	0.03	0.03	0.05	0.07	0.14	0.25	0.28	0.46	0.57	0.78	0.88	1.20	1.53	1.68	3
CK-7	0.02	0.03	0.04	0.04	0.12	0.16	0.22	0.38	0.51	0.64	0.87	1.03	1.50	1.71	3
Whole-rock (recalculated from modal mineralogy)															
CK-2	0.14	0.34	0.56	0.90	1.39	1.52	1.57	1.79	1.88	1.91	1.96	1.79	2.13	2.08	—
CK-3	0.10	0.09	0.07	0.07	0.09	0.10	0.12	0.13	0.18	0.22	0.25	0.25	0.32	0.33	—
CK-4	0.33	0.24	0.21	0.18	0.15	0.16	0.15	0.13	0.18	0.21	0.24	0.25	0.36	0.32	—
CK-5	0.53	0.53	0.51	0.54	0.57	0.60	0.64	0.72	0.73	0.80	0.76	0.77	0.90	0.78	—
CK-6	0.74	0.76	0.73	0.89	1.09	1.28	1.33	1.49	1.50	1.59	1.48	1.57	1.76	1.57	—
CK-7	0.51	0.57	0.72	0.89	1.23	1.73	1.32	1.64	1.48	1.55	1.47	1.50	1.74	1.41	—

2.5. Rb-Sr and Sm-Nd Isotopes

Portions of each spinel peridotite sample were crushed using a disk mill at the California Institute of Technology. Clinopyroxene grains (150–300 μm, 35–45 mg per sample, and free of visible inclusions and alteration) were picked by hand under a binocular microscope. These clinopyroxene separates were analyzed for strontium and neodymium isotopes at the University of Arizona, Tuscon, following the procedures described in Otamendi et al. (2009) and Drew et al. (2009). The samples were spiked with mixed ^{147}Sm-^{150}Nd tracers

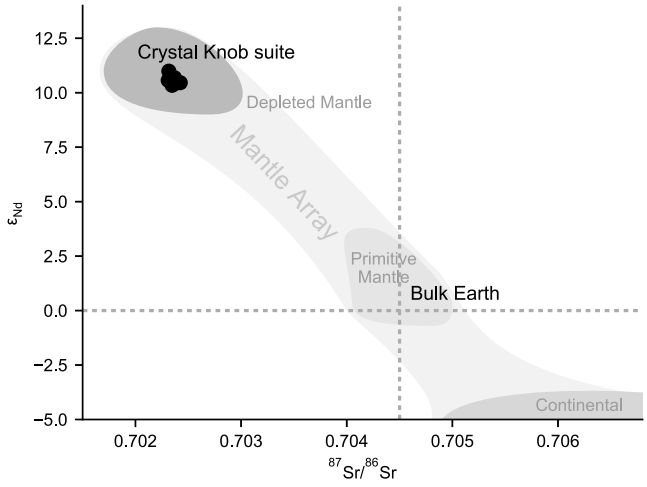

Figure 9. Paired Sm-Nd and Rb-Sr isotope data for the Crystal Knob sample set contextualized relative to major Earth reservoirs. The position of Crystal Knob within the *depleted mantle* field suggests that the mantle lithosphere underlying coastal California was sourced directly from shallow mantle material with no continental component, either beneath a mid-ocean ridge or by direct underplating.

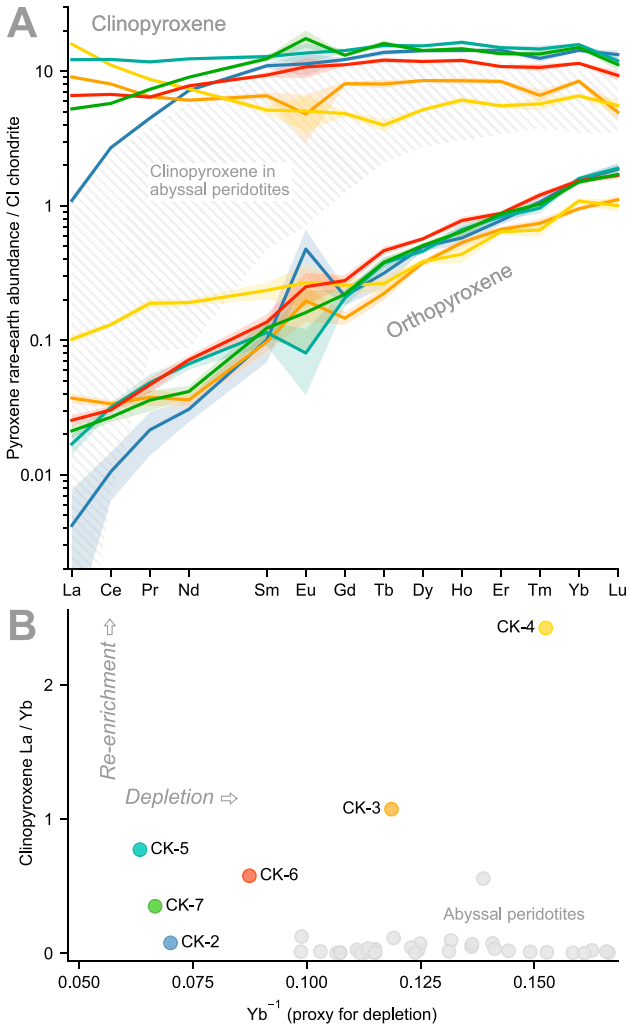

Figure 10. (a) Chondrite-normalized pyroxene rare-earth element abundances showing the range in depletion and re-enrichment in the Crystal Knob sample set. (b) Element ratio proxies for depletion and re-enrichment of clinopyroxene rare-earth elements, showing that samples have a range of depletion characteristics and levels of re-enrichment. Colors are by sample as labeled in (b).

(Ducea & Saleeby, 1998b; Wasserburg et al., 1981). Rb was measured on a quadrupole inductively-coupled plasma mass spectrometer (ICP-MS), while Sr was measured in static multicollector mode on a VG 54 instrument. Sm was analyzed using a static routine on a VG Sector 54 multicollector thermal ionization mass spectrometer, and Nd was measured as an oxide on a multicollector VG 354 instrument. Results are presented in Table 6.

All samples are enriched in radiogenic ^{143}Nd (time-corrected ϵ_{Nd} from 10.3 to 11.0) and depleted in ^{87}Sr (time-corrected ^{87}Sr/^{86}Sr of 0.702). These values are well below those of 0.708 recorded by Salinian granites (Chapman et al., 2014; Kistler & Champion, 2001), suggesting that the mantle lithosphere sampled by Crystal Knob is sourced from a different mantle reservoir than the overlying crust of the central California coast. More broadly, this pattern of strong depletion in large ion lithophile elements is characteristic of the depleted convecting mantle (Figure 9). This signature rules out an origin in the subcratonic mantle lithosphere or Mesozoic mantle wedge beneath western North America (Ducea & Saleeby, 1998a; Luffi et al., 2009; Wilshire et al., 1988) and suggests an origin in the asthenospheric or underplated oceanic mantle (DePaolo & Wasserburg, 1976; McCulloch & Wasserburg, 1978).

2.6. Trace Elements

Trace element concentrations were acquired for pyroxene grains in each xenolith sample, using a Cameca IMS-7f-GEO magnetic sector secondary ion mass spectrometer (SIMS) at the California Institute of Technology.

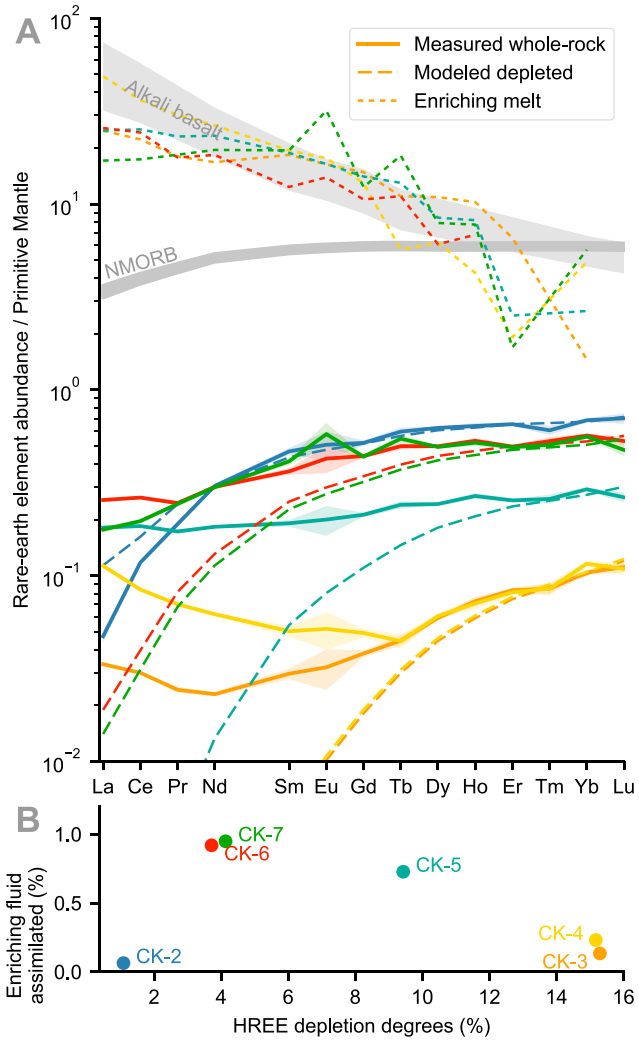

Figure 11. (a) Recalculated whole-rock trace elements for xenolith samples (Table 7) presented with best fitting modeled compositions for depleted peridotite and enriching fluid, using the model discussed in text. The rare-earth compositions of NMORB (Sun & McDonough, 1989) and alkali basalt (Farmer et al., 1995) are presented for comparison with the modeled composition of the enriching fluids, which closely resemble alkali basalt for all samples. Sample CK-2 shows no excess enrichment, and a hypothetical re-enriching fluid composition is not calculated. (b) REE depletion and re-enrichment trends for xenolith samples derived from modeling shown in (a). For all samples, <1% assimilation of alkali-basalt-like melt is required to explain the observed trends of REE re-enrichment. NMORB = normal mid-ocean ridge basalt; HREE = heavy rare-earth element.

Two to three each of orthopyroxene and clinopyroxene grains were targeted per xenolith sample. Measurements were acquired with 9-kV beam flux and a 100 μm spot size. The USGS glass standard NIST 610 was used as an external standard for all elements (Gao et al., 2002). Minimal variation in measured concentration was observed at grain and sample scale, though clinopyroxene in CK-6 and orthopyroxene in CK-7 show differences outside of analytical error in Ba, La, and Ce (potentially attributable to concentrations near SIMS detection limits). Other measurements are largely concordant, and results are presented as within-sample averages in Table 7 and Figure 10. Whole-rock trace element abundances (Table 7 and Figure 11a) are estimated by scaling measured concentrations in clinopyroxene and orthopyroxene to mineral modes. Olivine is excluded from calculations, which is of minimal impact as rare-earth elements (REEs) are 2–3 orders of magnitude less compatible in olivine than in clinopyroxene (Luffi et al., 2009; Witt-Eickschen & O'Neill, 2005). The resulting whole-rock trace element compositions correct for decreasing modal pyroxene abundances during depletion.

Table 8
Melting Degrees Estimated Using MgO, Al_2O_3, and HREE[a] Content

Sample	F_{HREE} (%)	F_{MgO} (%)	$F_{Al_2O_3}$ (%)
CK-2	1.1	7.0	11.6
CK-3	15.3	17.4	17.2
CK-4	15.2	18.3	17.6
CK-5	9.4	17.5	16.9
CK-6	3.7	0.3	7.9
CK-7	4.1	10.3	13.1

[a]heavy rare-earth element.

Clinopyroxene, orthopyroxene, and recalculated whole-rock REEs show the effects of both depletion and refertilization. The samples show a range of depletion in REEs relative to depleted mantle, and clinopyroxene HREEs (heavy REEs) follow patterns seen in abyssal peridotites (Warren, 2016) and consistent with single-stage depletion. Elevated LREEs (light REEs) suggest later refertilization. Whole-rock trace elements also record this pattern, but the incorporation of modal abundances highlights the range in REE depletion: sample CK-5 in particular has much lower REE concentrations than its clinopyroxene abundances would suggest, due to low clinopyroxene modes.

2.6.1. Modeling Depletion and Re-Enrichment

The partial correspondence of the trace element data set to abyssal peridotites suggests that enrichment can be compared to a typical mantle fractional melting history. We construct a melt-partitioning model to determine the degree of depletion of the Crystal Knob xenolith samples and distinguish between potential enriching agents (Figure 11a).

A generic model of peridotite depletion is constructed in *alphaMELTS* (Smith & Asimow, 2005), using the pMELTS family of algorithms. A parcel of material is tracked along an isentropic fractional melting path (1% melt porosity) starting at a mantle potential temperature of 1,350°C, 3.0 GPa, and a depleted MORB mantle (DMM) composition (Workman & Hart, 2005). Trace element partition coefficients from Lee et al. (2007) are used to track these components, and we confirm that garnet is removed from the evolving system at ~2.0 GPa. These starting parameters were chosen to provide the best correspondence with the overall experimental data set. A wide range of initial conditions (up to 1,500°C at 3.0 GPa) provides similar results for the shape of depleted trace element profiles, and the mapping of predicted composition to temperature depends on starting conditions.

The samples are fit to model steps along this adiabatic path using minimization of the squared deviations of measured values from model HREE (Er-Lu) compositions. HREE concentrations can reasonably be assumed to be a proxy for depletion, since HREEs, have low diffusion rates and are not easily modified by late re-enrichment. Thus, the best fitting decompression step gives a model composition for the samples after single-stage depletion. The measured composition of sample CK-2 matches this modeled composition across the REEs, while other samples have much higher LREE concentrations than is reasonable for residues of decompression melting.

In a second arithmetic step, the best fit depleted profile is subtracted from measured REE. Excess REE in the sample (typically LREE) is interpreted as the contribution from batch addition of an enriching melt. To improve comparability of the trace element pattern with that of potential enriching agents, the model is normalized

Table 9
Results of Two-Pyroxene Thermometers

Sample	TA98 (°C)	BKN (°C)	Ca-Opx (°C)	n_{opx}	n_{cpx}	REE (°)	
CK-2	core	949 (12)	1010 (10)	992 (4)	52	23	973 (9)
	rim	953 (21)	1012 (20)	1001 (8)	26	72	
CK-5	core	962 (22)	1030 (23)	980 (4)	49	44	956 (13)
	rim	953 (19)	1018 (21)	1020 (114)	65	22	
CK-7	core	976 (8)	1029 (8)	1008 (5)	31	45	961(10)
	rim	1002 (15)	1060 (22)	1026 (50)	33	28	
CK-4	core	1037 (15)	1075 (19)	1085 (4)	75	44	1071 (24)
	rim	1049 (9)	1093 (12)	1089 (14)	43	50	
CK-3	core	1042 (4)	1088 (4)	1069 (4)	44	65	1025 (17)
	rim	1043 (9)	1091 (10)	1083 (27)	67	60	
CK-6	core	1057 (14)	1093 (15)	1078 (4)	35	33	1087 (10)
	rim	1075 (5)	1110 (6)	1084 (11)	34	21	

Note. For major element thermometers, σ (in parentheses) represents errors between individual measurements. For REE thermometer, it is regression error. REE = rare-earth element.

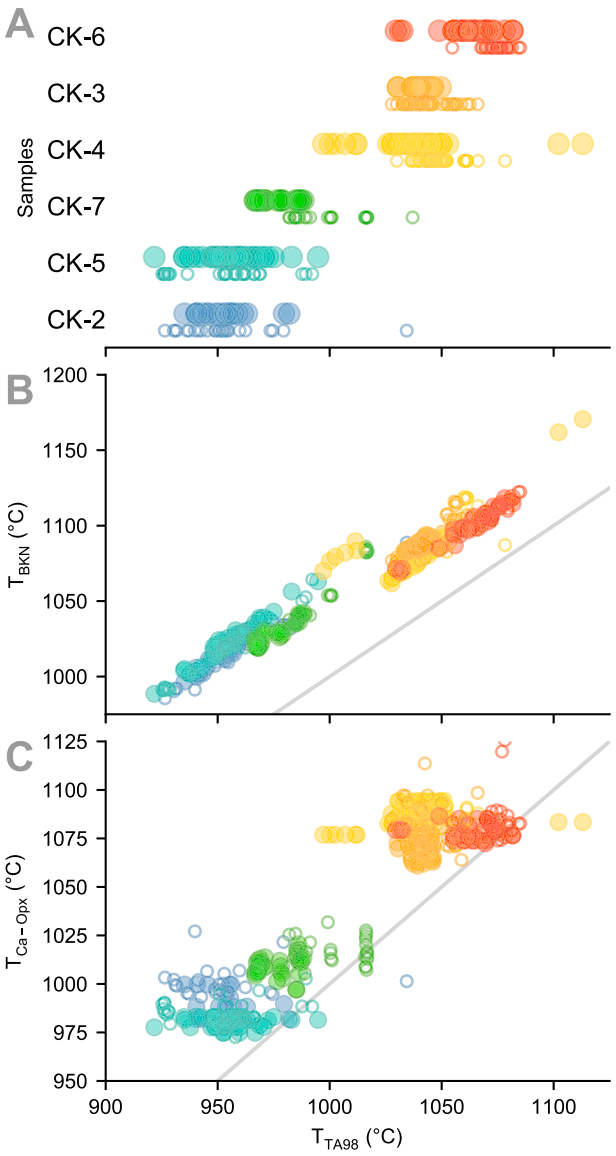

Figure 12. Comparison of results from pyroxene major element thermometers. (a) TA98 core and rim measurements (filled and open circles, respectively) categorized by sample. Samples CK-3, CK-4, and CK-7 show elevated grain rim temperatures, and core temperatures largely fall within a 25–50°C range for each sample. (b) TA98 and BKN temperatures showing a strong linear relationship, with BKN estimates higher by 30–70°C. (c) Ca-in-orthopyroxene and TA98 temperatures, showing the reproduction of two temperature cohorts around 980 and 1080°C by the Ca-in-orthopyroxene thermometer. Colors are by sample as labeled in (a). Gray lines show 1:1 relationship.

to an average HREE of six times primitive mantle, a typical HREE concentration for both normal MORB (Sun & McDonough, 1989) and alkali basalt (Farmer et al., 1995). The slope of the resulting normalized profile is diagnostic of the relative abundance of trace elements in the re-enriching agent. The normalization factor employed to shift the composition of enriching fluids to this value (Figure 11b) is proportional to the amount of material added during re-enrichment (assuming a consistent composition).

The model results show that partial melting, followed by re-enrichment by alkali basalt, can explain the trace element variability within the Crystal Knob sample set. REEs in the fertile lherzolite CK-2 follow the modeled trend for nearly undepleted peridotite (Figure 11). Enrichment by the assimilation of small amounts (<1%) of a melt with a trace element pattern similar to alkali basalt is reasonable for all samples (Figure 11b). The low pyroxene modes in samples CK-3 and CK-4 lead to pronounced LREE enrichment, with the assimilation of small masses of enriching melt greatly increasing normalized abundances. However, if HREEs have been substantially enriched (as may be the case for sample CK-6), excess LREE is a minimum constraint on re-enrichment.

Primary depletion degrees are estimated by finding the pMELTS model compositions that best fit the whole-rock HREE, MgO, and Al2O3 composition of each xenolith sample (Table 8). Results show trends superficially similar to those in modal abundance (Figure 8) and trace element (Figure 10) data.

2.6.2. Discussion of Trace Elements

The HREE compositions and modeled depleted REE profiles of the Crystal Knob xenoliths are similar to those found in abyssal peridotites (Johnson et al., 1990), suggesting that the xenoliths are residues of progressive fractional melting of primitive mantle at the mid-ocean ridge. Trace element patterns, and their alignment with phase composition and modal abundance, suggest that HREE depletion within the Crystal Knob samples is primary, without significant HREE re-enrichment. These trends are a proxy for fertility, and the lherzolite CK-2 is essentially undepleted and apparently has not been fractionally melted.

The variably elevated LREE content of all samples except CK-2 is not present in abyssal peridotites (Figure 10) and suggests secondary re-enrichment by LREE-rich material at depth. Our modeling of whole-rock depletion and re-enrichment suggests a similar degree of LREE refertilization for all samples except CK-2, corresponding to a volumetrically minor <1% bulk assimilation of fractionated basaltic melt. The most pronounced LREE enrichments occur in infrequent clinopyroxene grains in depleted harzburgites (CK-3 and CK-4) and may arise from the preferential assimilation of REEs in sparse clinopyroxene. Sample CK-6 contains high LREEs in excess of those formed at any stage of fractional melting. This suggests that CK-6 assimilated a significant amount of more evolved melt and has a trace element profile (including HREE composition) formed by refertilization.

2.7. Major Element Thermometry

Electron microprobe major element data are used as the basis for pyroxene Ca exchange geothermometry. Several complementary formulations are used: BKN (Brey & Köler, 1990) and TA98 (Taylor, 1998) are two slightly different formulations based on empirical calibration of the two-pyroxene Ca exchange reaction in with laboratory systems. TA98 is explicitly calibrated to account for errors arising from high Na content. The Ca-in-orthopyroxene thermometer (Brey & Köler, 1990) is formulated for use in the absence of clinopyroxene. Results are shown in Table 9 and Figure 12.

Core and rim compositions are separated to assess within-sample temperature disequilibrium and late-stage (e.g. eruptive) heating. Analytical errors (caused by uncertainty in microprobe data) are small, on the order of 5°C (1σ). Other sources of error include the calibration of the thermometer and potential bias from within-sample disequilibrium. Taylor (1998) reports residuals of calibration of the thermometer to experimental data, which yield total errors of 50–60°C (1σ). Unreported calibration errors for the BKN and Ca-OPX thermometers are likely similar in scale (Taylor, 1998). In practice, error distributions based on calibration with heterogeneous experimental samples likely form an upper bound on relative errors.

Within-sample temperature variation is a proxy for the relative error of recovered temperatures. Measured pyroxene compositions are grouped by location, and separate temperatures are calculated for each nearest-neighbor pair of orthopyroxene and clinopyroxene. Analytical errors are propagated through the calculation. The resulting distribution of temperatures for grain cores and rims for each sample (with *n* ranging from 19 to 74 pairs per group) accounts for within-sample variation and provides an approximation of measurement precision.

2.7.1. Thermometer Results

Average TA98 temperatures range from 957 to 1063°C for cores and 955 to 1054°C for rims (Table 9). CK-2 core temperatures indicate more complete equilibration, with a standard deviation of only 2.3°C (compared with 8.2–12.4°C for all other samples). Core temperatures for individual grain pairs are distributed roughly normally, and clustered temperatures in an ~25–50°C range for each sample suggest that aggregated grain pair temperatures model errors around true sample equilibrium temperatures. Outlying core temperatures in samples CK-4 and CK-6 may indicate two-pyroxene major element disequilibrium at millimeter scale. In CK-4, a few core TA98 temperatures of 1100°C are likely related to late-stage diffusion during entrainment and eruption.

Rim temperatures (measured ~10 μm from grain edges) are generally higher than core temperatures, although the level of disparity varies widely between samples. CK-2 shows only modestly elevated rim temperatures, while CK-3 and CK-6 show significant scatter to temperatures ~180°C higher than grain cores (CK-5 and CK-7 contain a few measurements of this type as well). High and variable rim temperatures may be related to melt infiltration during entrainment and eruption but with significant mobilization of cations limited to grain rims. CK-4, which shows high core temperatures and the most significant petrographic evidence of melt infiltration, lacks high-temperature rim compositions, suggesting equilibration at high temperature, possibly in the Crystal Knob melt.

2.7.2. Discussion of Two-Pyroxene Thermometry

Different two-pyroxene thermometers produce similar results, suggesting that temperature measurements are robust estimates of sample equilibrium temperatures (Figure 12). The Ca-in-OPX thermometer shares its calibration with BKN (Brey & Köler, 1990) and sensibly yields coincident results. The low within-sample scatter of Ca-in-OPX temperatures likely results from fast diffusion and re-equilibration of small amounts of Ca in orthopyroxene. TA98 and BKN temperatures have a strong linear relationship, with BKN temperature estimates higher by up to 50°C. This relationship mirrors the findings of Nimis and Grütter (2010) and can be expressed as $T_{BKN} = 0.9T_{TA98} + 145$ (°C). Nimis and Grütter (2010) advise the preferred use of TA98 based on experimental validation. Given the largely predictable results of two-pyroxene thermometers, we accept their preference for further analysis.

The samples can be divided into two cohorts based on equilibration temperature. A cooler group (samples CK-2, CK-5, and CK-7) has grain core temperatures clustered at ~970°C (TA98). A hotter group (samples CK-3, CK-4, and CK-6) has a mean temperature of ~1,050°C (TA98). The division between these two groups is robust, apparent in all thermometers, and aligned with geochemical differences within the sample set. The hotter samples have higher spinel Cr# and greater HREE depletion, and the range of temperatures likely records the sourcing of two sets of xenoliths from different depths within a magmatic ascent system. Throughout this paper, the samples are color coded, with blue-green corresponding to the low-temperature array and red-yellow representing the high-temperature samples (Figure 6–15).

2.8. REE-in-Pyroxene Thermometry

We use the Liang et al. (2013) REE in two-pyroxene thermometer to estimate sample equilibration temperatures using an independent system. The relative immobility of REEs allows assessment of equilibrium temperatures over longer timescales than those queried with two-pyroxene cation exchange thermometry.

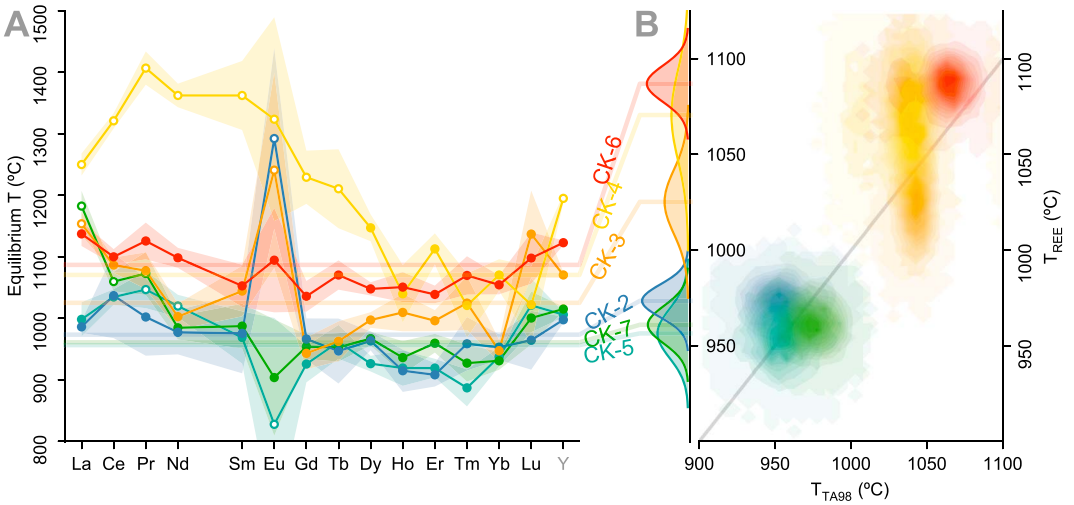

Figure 13. REE thermometry of xenolith samples. (a) Per element equilibrium temperatures with projection of best fitting sample temperature as horizontal lines for each sample. Data points far from the horizontal line signify disequilibrium between pyroxene phases, and those outliers plotted with open circles are excluded from the fit. (b) Best fitting REE temperatures for each sample with Gaussian error bounds, plotted against a kernel density distribution of TA98 major element temperatures. Joint error distributions are created using a Monte Carlo approach for both error distributions. This approach shows significant disequilibrium in Eu and across LREE for sample CK-4. The samples can be grouped into two temperature cohorts, with all samples, especially the low-temperature group, agreeing well with the TA98 thermometer. Colors are by sample.

Rare-earth abundances are compiled for SIMS measurements of pyroxene phases in contact (two to three pairs) for each xenolith sample. A two-pyroxene equilibrium is calculated for each REE and Y and is shown in Figure 13a. A robust regression with a Tukey biweight norm is used to find the equilibrium temperature for each sample. Significant outliers from the fit are excluded from thermometry and discussed below. Measured temperatures are between ~950 and 1100°C for the sample set (Table 9) and broadly correspond to TA98 temperatures for each sample (Figures 13b and 14), although some differences may be diagnostic of preserved fossil heating events.

2.8.1. Pyroxene Rare-Earth Disequilibrium

CK-3 shows misfit in La, while CK-5 and CK-7 have disequilibrium in several LREEs. Sample CK-4 shows major disequilibrium in the light and medium REEs, with only elements heavier than Ho retaining a linear relationship.

The pattern of disequilibrium in sample CK-4 could force assimilation of REEs into orthopyroxene, effectively raising the LREE mineral-melt partition coefficient $D^{opx/cpx}$ relative to HREEs. The shape of this disequilibrium may be due to the parabolic nature of the partition curves for both pyroxene phases, which are incompletely modeled by a linear relationship when offset (Blundy & Wood, 2003; Sun & Liang, 2012). The incorporation of more LREEs into orthopyroxene due to low clinopyroxene modes (Figure 10) could also magnify any miscalibration of the thermometer. Regardless, since measured LREEs are consistently enriched, with low analytical errors for both orthopyroxene and clinopyroxene, we conclude that anomalies in LREE temperature do not signal disequilibrium compositions.

All samples except CK-6 and CK-7 show results off the linear trendline for Eu. This disequilibrium, discussed in Sun and Liang (2012), is dependent on the oxygen fugacity (and Eu^{2+}/Eu^{3+} ratio) of the host magma. In normal magmas, this pattern could also arise from the effect of *ghost* plagioclase, which can create local Eu enrichments and depletions in the neighborhood of resorbed plagioclase grains. This would suggest that the xenoliths originated in the shallow mantle lithosphere and were transported deeper, causing plagioclase breakdown. Discerning between these scenarios is difficult due to Eu abundances near ion microprobe detection limits.

Two-pyroxene REE disequilibrium can be explained by a fossil heating event that was retained only in REEs due to their slow diffusion rates. This must have happened prior to subsolidus major element re-equilibration and is thus unrelated to the Crystal Knob eruption. Potential causes include focused heating of sample CK-4,

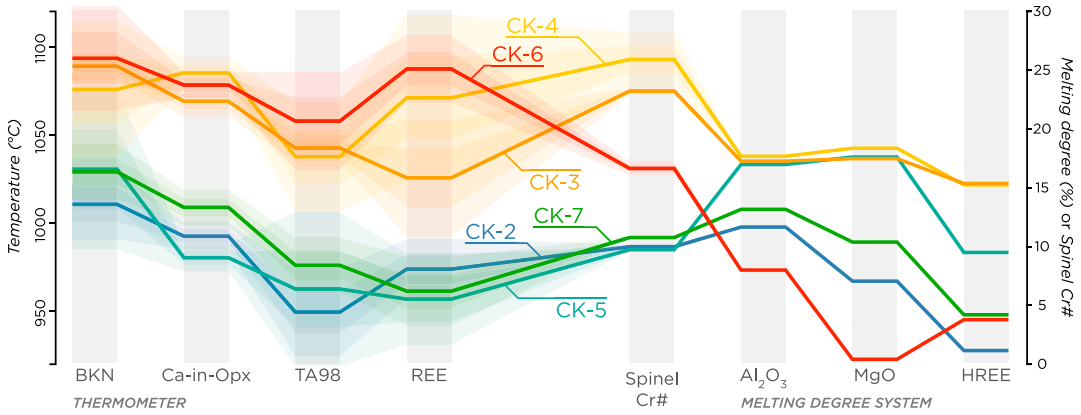

Figure 14. Summary of temperature and depletion degree data for the peridotite xenoliths showing the two temperature cohorts of the data set, which remain separable for all thermometers and are centered roughly 80°C apart. Estimates for all thermometers track together except for the higher-temperature estimates for the REE thermometer for samples CK-4 and CK-6, which may reflect a fossil heating event. Spinel Cr# and several melt extraction proxies are used to assess the level of depletion of the samples. The lower-temperature samples are generally less depleted in all systems, with variable MgO and Al2O3 depletion reflecting low modal abundances of pyroxene. Sample CK-6 has moderately high spinel Cr# but low levels of whole-rock depletion, suggesting bulk assimilation of an enriching fluid. REE = rare-earth element.

poorly understood equilibrium partition coefficients (e.g., due to reducing mantle conditions), and incomplete linearizing assumptions in the Liang et al. (2013) thermometer. Untangling these effects is beyond the scope of this work but presents several opportunities for further study.

2.8.2. Comparison With Major Element Thermometry

Rare-earth exchange thermometry confirms the temperature groupings found by major element thermometry (Figure 14). REE temperatures of 950–970°C for the low-temperature cohort are most comparable to TA98. For these samples, the TA98 and REE temperatures together record long-term equilibrium with no significant thermal perturbations. In the high-temperature cohort, samples CK-4 and CK-6 record REE temperatures significantly higher than TA98 (~1080°C versus ~1040°C). CK-3 records a lower temperature in line with major element thermometry. Trivalent REEs in pyroxene diffuse several orders of magnitude slower than bivalent major elements (Liang et al., 2013), so high-temperature events can set the distribution of REEs despite subsequent major element re-equilibration at lower temperature. Higher temperatures recorded by REE thermometry for CK-4 and CK-6 are likely due to a fossil heating event that primarily affects the deepest samples.

CK-4 may have experienced a unique transient heating event, with individual LREE cations recording high temperatures (>1200°C) in disequilibrium with the ~1070°C HREE temperature (Figure 13a). This event could result from metasomatic processes, which possibly correspond to the melt infiltration textures (intergranular melt channels) unique to this sample (Figure 4).

3. Geothermal Constraints on the Deep Lithosphere

3.1. Extrapolation From Surface Heat Flow

Previous studies have used surface heat flows to estimate the thermal structure and evolution of the mantle lithosphere beneath the central California coast ranges. Blackwell and Richards (2004) compiled a heat flow database across the western United States based on borehole measurements in wells >100 m deep. Erkan and Blackwell (2009) reports a *Coast Range Thermal Anomaly* of high surface heat flux (70–90 mW/m^2) which spans the entire Coast Range belt, on both sides of the San Andreas Fault zone. The Mojave Plateau has similarly high heat flows, but lower heat flows of 20–40 mW/m^2 are found in the adjacent Central Valley and Sierra Nevada. Coast Range heat flows are high in the global distribution of regionally averaged continental heat flows, which ranges from lows of 20 mW/m^2 in cratonic cores to 120 mW/m^2 in focused areas of active mantle upwelling (e.g., the southern Salton Trough; Erkan & Blackwell, 2009; Pollack & Chapman, 1977).

Erkan and Blackwell (2009) attributed high surface heat flows in the Coast Ranges to nonconductive processes such as shear heating, rapid surface uplift, and fluid circulation along faults. Shear heating does not cause

Table 10
Material Properties Used in Modeling

Material properties		CC[a]	ML[b]	
Thermal conductivity	k	2.7	3.138	W/m/K
Specific heat capacity	C_p	1,000	1,171	J/kg/K
Density	ρ	2,700	3,300	kg/m^3
Radiogenic heat generation	α	2.5	0.006	μ W/m^3
Mantle potential temperature	T_p		1,450	°C
Kinematic properties (Royden, 1993, subduction model)				
Rate of subduction	v		100	mm/yr
Backarc distance of emplacement	x		100	km
Depth of subduction interface	z		30	km
Frictional heating	q_{fric}		0	mW/m^2
Subduction accretion	a		0	m/s
Subduction erosion	e		0	m/s

[a]continental crust. [b]mantle lithosphere.

significant additions to heat flow (e.g., Kidder et al., 2013; Lachenbruch & Sass, 1980). However, sustained rock uplift and erosion, such as that documented since 2 Ma in the Santa Lucia Range (Ducea et al., 2003), can raise the crustal geothermal gradient through advection of material. More significantly, regional thermal conductivity can be enhanced by hydrothermal circulation in the presence of fractures. The crust of the Coast Ranges and the Mojave Plateau underwent extensive Late Cretaceous crustal detachment faulting (Wood & Saleeby, 1997; Chapman et al., 2012), and the Coast Ranges underwent additional Neogene transform faulting. Mantle fluids in the San Andreas Fault zone (Kennedy, 1997) suggest fluid upwelling along these fractures, and high surface heat flows may be due to increased permeability, fracture-following fluid transport, and heat advection. In contrast, the intact batholithic domains underlying the Sierra Nevada, Central Valley, and Peninsular Ranges have relatively low heat flows (Erkan & Blackwell, 2009).

Nonconductive heat transport can significantly impact the extrapolation of lithospheric geotherms from surface heat flows, and conductive geotherms anchored at the surface may overestimate mantle lithosphere temperatures. Accordingly, mantle lithosphere temperatures modeled by seismic tomography are cooler than those extrapolated from surface heat flows. Goes and van der Lee (2002) predict temperatures of 700–1100°C at 50- to 100-km depth beneath coastal California, suggesting <60 mW/m^2 steady state heat flows. Li et al. (2007) estimate the lithosphere-asthenosphere boundary to be at ~70-km depth in the southern Coast Ranges. With a 1200–1300°C lithosphere-asthenosphere boundary (e.g., O'Reilly & Griffin, 2010; Fischer et al., 2010), this corresponds to steady state heat flows of 70–80 mW/m^2.

Steady state geotherms extrapolated from surface heat flows generalize the heat transfer properties of the entire lithospheric column and thus provide only first-order constraints on mantle lithosphere thermal state. Measurements of temperature and depth of xenolith equilibration can allow more direct reconstruction the deep lithospheric geotherm.

3.2. Depth Constraints From Crystal Knob Xenoliths

The depths of the xenolith samples in the mantle lithosphere, coupled with equilibration temperatures, provide a direct constraint on the geotherm beneath Crystal Knob at the time of eruption. Pyroxene exchange geothermometry shows that the peridotite samples form two temperature groups with centroids separated by roughly 60°C. This temperature range likely corresponds to an array of sample sources along a depth gradient. For spinel peridotites, equilibration depths can only be analytically determined within broad boundaries. With no reliable geobarometers for spinel peridotites, several less robust metrics are used to evaluate the depth of the xenolith source. We present several lines of reasoning suggesting that the samples

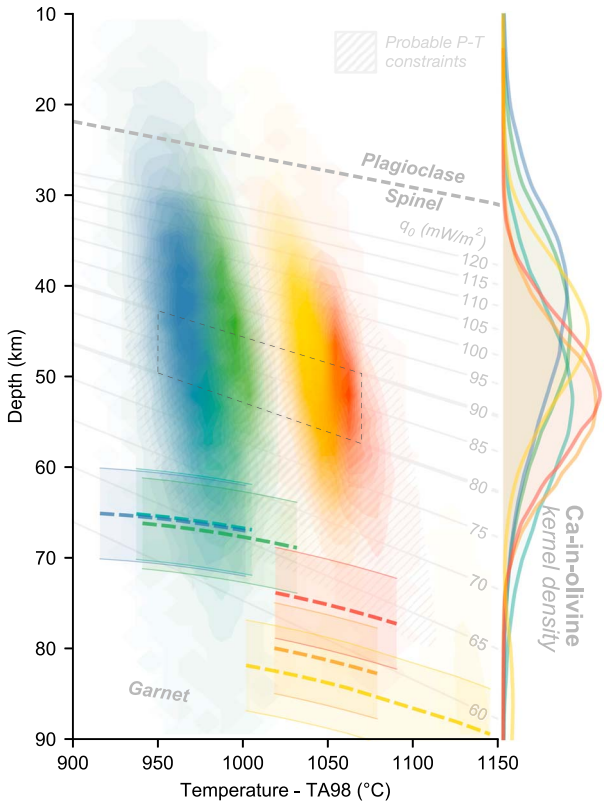

Figure 15. Summary of depth constraints for the xenolith samples. Colored fields represent density contours of Monte Carlo error distributions of Ca-in-olivine pressure/TA98 temperature pairs for each sample, accounting for analytical errors and within-sample scatter. Plots on the right margin project these distributions along the depth axis. Colored, dashed lines show estimates of the maximum spinel stability depth for spinel Cr content matching each sample (O'Neill, 1981), with imposed error bars of 0.15 GPa. The hatched background represents P-T bounds of the potential xenolith source region based on thermobarometry and phase stability. Steady state conductive geotherms for values of surface heat flow q_0 are plotted beneath the data, with 80–90 mW/m^2 highlighted as maximum reasonable geotherms for the mantle. A dashed box shows the extent of sample temperatures along these geotherms. The synthesis of this data suggests that the samples were sourced from ~45- to 75-km depth.

were entrained from relatively deep in the spinel stability field (~45–75 km). Several of the techniques below produce estimates of pressure rather than depth. We convert these to depths using a hydrostatic gradient of ~0.03 GPa/km, integrating crust and mantle densities given in Table 10.

3.2.1. Limits of Spinel Stability

Entrainment depths of all peridotite xenoliths must be greater than ~30 km, the depth of the Moho near the Crystal Knob eruption site (Tréhu, 1991), which will be discussed in more detail in section 4. The plagioclase-spinel peridotite facies transition (typically at 20–30 km) is another minimum depth constraint,but it is highly composition dependent (Green & Ringwood, 1970), with high-Cr harzburgites stable to the surface (Borghini et al., 2009).

The high-pressure boundary of spinel stability limits maximum possible entrainment depths. The spinel-garnet peridotite facies transition is composition dependent and poorly constrained for natural systems but thought to lie over the 50- to 80-km depth interval (O'Neill, 1981; Kinzler, 1997; Gasparik, 2000; Klemme, 2004). The breakdown depth of spinel is strongly dependent on temperature and composition, particularly the amount of refractory Cr hosted by spinel. Several experimental and thermodynamic studies have estimated the magnitude of this effect. O'Neill (1981) presented experiments both with and without Cr and described a simple empirical relationship of spinel-out depth with Cr content and temperature. Robinson and Wood (1998) suggest that, given fertile *pyrolite* compositions with little Cr, garnet is unstable at depths less than 80 km at the peridotite solidus (~1470°C at this depth). Subsolidus experimental results show that the maximum depth of the spinel stability field in the absence of Cr ranges from 1.8 to 2.0 GPa (55–60 km) at 1,000–1,200°C (Klemme & O'Neill, 2000). Chromian spinels are stable to much greater depth: thermodynamic modeling by Klemme (2004) suggests a broad garnet-spinel costability field (up to a spinel-out reaction at 5 GPa for Cr# of ~30), but a spinel-weighted metastable assemblage is possible even at higher pressures.

Samples in the high-temperature cohort (CK-3, CK-4, and CK-6) have high spinel Cr# due to their history of depletion by partial melting (Figure 6c). This enrichment in refractory Cr expands the stability field of spinel against garnet to deeper depths. Though Robinson and Wood (1998), Klemme and O'Neill (2000), and Klemme (2004) show a high-pressure phase transition with a complex compositional dependence, the rough estimate of the garnet-in pressure given by O'Neill (1981) performs sufficiently well at $T < 1200$°C. This empirical relationship is used in Figure 15 to graphically illustrate the predicted depth of the spinel-garnet phase transition based on the Cr# of each sample. This simple treatment provides a high-pressure constraint on the Crystal Knob xenolith source. The maximum possible entrainment depth of the highest-Cr residual samples is ~80 km versus ~65 km for the low-Cr samples.

3.2.2. Ca-in-Olivine Barometer

Equilibration pressure measurements are attempted for the peridotite xenoliths using the Köhler and Brey (1990) Ca-in-olivine barometer, which is based on the decreasing abundance of Ca in olivine with pressure. This barometer is calibrated for spinel peridotites, but its accuracy is limited by poor resolution, high temperature dependence, vulnerability to late-stage diffusion, and dependence on low Ca concentrations in olivine near analytical thresholds for electron microprobe analysis (Medaris et al., 1999; O'Reilly, 1997).

Within each sample, pressures are calculated separately for nearest-neighbor pyroxene and olivine measurements, and analytical errors are propagated through the calculation. Measured olivine Ca concentrations of ~200–400 ppm are scattered within each sample but separable (Figure 16). To correct for the mild pressure dependence of the two-pyroxene thermometer and coupled temperature dependence of the olivine barometer, we jointly solve temperature and pressure by iterative optimization. This yields internally consistent

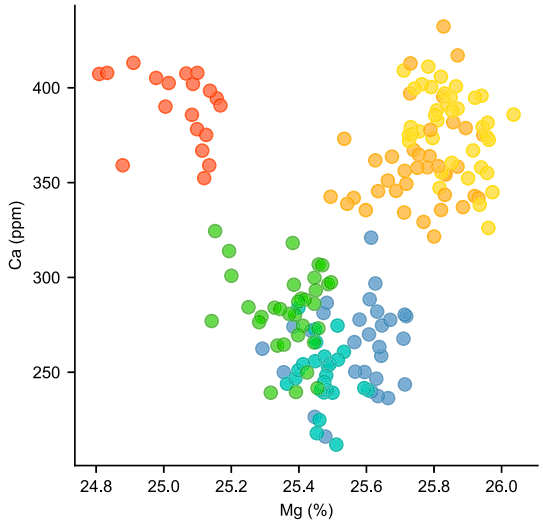

Figure 16. Ca abundance in olivine for peridotite samples, showing elevated Ca in samples CK-3, CK-4, and CK-6. The significant scatter in microprobe analyses (colored by sample) is due to low measured abundances.

pressure and temperature measurements for each set of analytical points. For each pressure estimate, sensitivity to analytical errors is explored using Monte Carlo random sampling ($n = 100,000$). The density of the resulting error space yields a probable depth range for each sample (Figure 15).

The Ca-in-olivine barometer yields model depths with modes between 40 and 53 km, largely coincident with the spinel stability field (Figure 15). Within the Crystal Knob sample set, the low- and high-temperature cohorts remain separable, with high-temperature samples showing deeper equilibrium depths. The scale of errors within a single sample reflects the barometer's strong covariance with major element thermometers, as well as its sensitivity to small variations in Ca concentrations. Much of the spread in the data reflects the poor calibration of the barometer: the low-temperature samples in particular have significant scatter toward depths above the spinel-in isograd. The large Ca cation diffuses rapidly during transient heating (Köhler & Brey, 1990), producing a shallowing bias on the depth distribution. This may explain why CK-4, which apparently experienced a unique transient heating event, has a depth mode ~10 km shallower than samples with similar equilibration temperatures (CK-3 and CK-6). Likewise, higher REE temperatures for samples CK-4 and CK-6 may indicate a slightly deeper source. Despite the imprecision of the method, Ca-in-olivine barometry suggests that the samples were sourced from >40 km, relatively deep within the spinel stability field.

3.2.3. Comparisons With Steady State Heat Flow

Estimates of xenolith depth can be constructed by pinning the equilibrium temperatures of the Crystal Knob samples to a conductive geotherm constrained by surface heat flux. In Figure 15, we show a range of geothermal gradients corresponding to surface heat fluxes of 60–120 mW/m^2. These are calculated using values for thermal conductivity and diffusivity given in Table 10 for the crust to a depth of 30 km and mantle lithosphere below this level. The empirical factor of 0.6 proposed by Pollack and Chapman (1977) is used to reduce surface heat flux to a presumed mantle contribution, with the remainder being taken up by radiogenic heat production near the surface. Radiogenic heating is modeled to decrease exponentially with depth, with an *e*-folding length scale of 10 km. Mantle heat flux and lithospheric thermal conductivity are the main controls on the slope of the modeled geothermal gradient. This methodology is developed in Turcotte and Schubert (2002) and is identical to that used by Luffi et al. (2009), except that crustal thermal conductivity is reduced to match the conditions used in dynamic thermal modeling (section 5). This yields a slightly *hotter* geotherm throughout the mantle lithosphere.

Depths of entrainment can be estimated by projecting the TA98 temperatures for each sample onto these model geotherms. Geotherms corresponding to all reasonable surface heat flows suggest entrainment over a depth range of 5–10 km within the mantle lithosphere, with the hotter samples more deeply sourced. Steady state geotherms anchored to surface heat flows of 65–120 mW/m^2 place the Crystal Knob sample set within the spinel stability field, and 70–110 mW/m^2 surface heat flows limit depths to the range modeled by Ca-in-olivine barometry. Measured surface heat flows of 80–90 mW/m^2 for the central California coast (Erkan & Blackwell, 2009) suggest depths of ~45–55 km for the Crystal Knob sample set.

3.3. Discussion of Xenolith Geothermal Constraints

The Crystal Knob xenoliths are sourced within the mantle lithosphere, deeper than 30 km (the Moho) and shallower than the 60–90 km lower boundary of the spinel stability field. Ca-in-olivine barometry suggests tighter constraints near the center of the spinel stability field. Model depths of 45–55 km from steady state geotherms agree with xenolith thermobarometry but may be underestimates due to potential nonconductive heat transfer through the crust (section 3.1). Given the bias of both Ca-in-olivine and heat flow measurements toward shallower depths, we suggest that the xenoliths were likely entrained at 45- to 75-km depth. This implies that the thermal structure of the mantle lithosphere can be modeled by conductive geotherms with

~65–90 mW/m^2 steady state heat flow. Relatively deep entrainment of the Crystal Knob xenoliths along a fairly cool lithospheric geotherm conforms to constraints from independent studies.

3.4. Geochemical Variation With Depth and Temperature

The Crystal Knob peridotite xenoliths vary in composition with temperature, with two separable cohorts that sample mantle material with somewhat different major and trace element characteristics. Major element and REE depletion track together and generally increase with the equilibration temperature of the sample, with the notable exception of sample CK-6. These differences in temperature are implicitly linked to a gradient in entrainment depth.

The low-temperature and shallower cohort includes phases with relatively fertile compositions in both major and trace elements. The samples have phase compositions similar to DMM (Workman & Hart, 2005), and clinopyroxene trace elements range from essentially undepleted to low levels of depletion characteristic of the least-depleted abyssal peridotites (Figure 10).

The higher-temperature, deeper samples CK-3 and CK-4 contain phases with high Mg#s, which suggests that all phases lost incompatible elements during high-degree depletion. These features, along with high levels of REE depletion, extremely low clinopyroxene modes, and chromian spinels, indicate significant melt extraction. Distinct enrichments in LREE likely correspond to assimilation of a fractionated melt, though this is modeled to be volumetrically insignificant.

Sample CK-6, the hottest and deepest sample, has a highly enriched major element composition, and is only moderately depleted in HREEs. However, high modal abundance of pyroxenes and spinel, and simultaneously elevated Cr, Al, and LREE suggest both significant depletion and re-enrichment. This is bolstered by petrographic evidence of substantial intergrowth and aggregation of pyroxene grains, unique in the sample set. Elevated REE-in-two-pyroxene temperatures for samples CK-4 and CK-6 suggest a fossil heating event not shown in major element thermometry. This event may have been more completely felt by sample CK-6, which has a fully equilibrated REE temperature measurement (Figure 13) and appears to have assimilated a sizable amount of enriched material.

The increasing depletion with depth of the Crystal Knob samples suggests increased melt extraction deeper in the lithospheric column. This pattern does not match the decrease in melting degrees with depth expected for decompression melting. Also, the geochemical variation between undepleted and depleted/re-enriched samples within a <10 km depth range suggests potential lateral heterogeneity to melting. Luffi et al. (2009) found a similar inverted pattern within mantle lithosphere packages beneath Dish Hill, ascribing fertile lherzolites at the top of the package to refertilization of suboceanic mantle lithosphere. With the exception of sample CK-6, HREE refertilization of the Crystal Knob samples is unlikely due to consistent major- and trace element chemistry.

The low-temperature samples are petrologically similar to abyssal peridotites (Figure 8 and Figure 10), suggesting an origin as fertile to moderately depleted suboceanic mantle lithosphere. The depleted harzburgites CK-3 and CK-4 could be tectonically juxtaposed to deeper levels by duplexing (as in Luffi et al., 2009) or depleted after emplacement by deeply sourced melting. Along these lines, the obvious refertilization of CK-6 at the base of the column shows melt-rock interactions that were most intense at deep levels. This spatial pattern of melt generation is commonly associated with flux melting in subarc settings (e.g., Jean et al., 2010) but could also arise from intense heating from below (Thorkelson & Breitsprecher, 2005). In this context, depletion of the deeper samples at Crystal Knob would correspond to melt generation deep within the mantle lithosphere.

4. Origin of the Mantle Lithosphere Beneath the Coast Ranges

The Crystal Knob spinel peridotite xenoliths are uniformly isotopically depleted, with an ϵ_{Nd} of 10.3-11.0, and $^{87}Sr/^{86}Sr$ of 0.7023-0.7024. These values are typical for the depleted upper mantle (e.g Hofmann, 1997) and require a mantle source that has not been recycled from the western North American subcontinental mantle or continental lithosphere more generally. Potential origins include underplated suboceanic or upwelling asthenospheric mantle material.

The lack of radiogenically enriched arc residues in the Crystal Knob xenolith suite confirms the unrooted nature of Salinia arc rocks (e.g., Hall and Saleeby, 2013) that lie slivered above the Franciscan accretionary

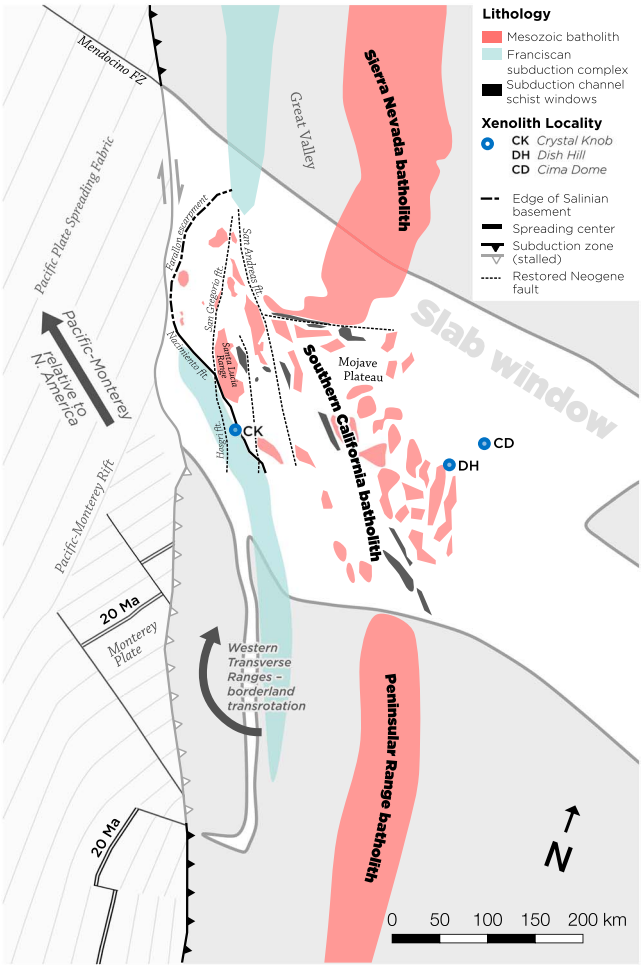

Figure 17. Tectonic reconstruction of the California margin at 19 Ma showing the early evolution of the San Andreas transform system, the evolving slab window and microplate detachment (after Wilson et al., 2005), and the reconstructed location of modern exposures of the Cretaceous batholithic belt, the disaggregated Mojave–Salinia batholith, and surface outcrops of subduction channel schists in the Mojave province (after Schott & Johnson, 1998, 2001; Chapman et al., 2012; Dickinson et al., 2005).

complex that dominates the crust of the Coast Ranges. This suggests the existence of a major structural discontinuity below the crust, with underplated, depleted peridotite forming the framework of the mantle lithosphere. The Crystal Knob xenolith suite is the only known direct sampling of this underplated mantle beneath coastal California. Several tectonic events since Cretaceous time could have replaced the mantle lithosphere beneath the Coast Ranges.

The Franciscan complex of the region was assembled by sustained subduction of the Farallon plate during the Cretaceous and early Cenozoic periods (Cowan, 1978; Chapman et al., 2016; Saleeby et al., 1986; Seton et al., 2012). The mantle lithosphere beneath the eastern Mojave Plateau was constructed from partly subducted Farallon plate upper mantle late in this Franciscan accretionary history (Luffi et al., 2009), and an outboard equivalent of this mechanism could have built the mantle lithosphere beneath Crystal Knob.

In Oligocene to early Miocene time, the Pacific-Farallon spreading ridge obliquely intersected the Cordilleran subduction zone at the coast of southern California, leading to the development of the San Andreas transform system (Atwater, 1970). Progressive impingement of large-offset ridge-ridge transforms resulted in the opening of a geometrically and kinematically complex slab window (Atwater & Stock, 1998; Wilson et al., 2005). Late Cenozoic volcanism of the coastal region of central California has been attributed to partial melting of asthenosphere as it ascended into the slab window (Wilson et al., 2005).

The Monterey microplate (Figure 17) nucleated as an oblique intra-oceanic rift along an ~250 km long segment of the Pacific-Farallon ridge (Bohannon & Parsons, 1995; Thorkelson & Taylor, 1989) during slab window formation (Wilson et al., 2005). Microplates may have stalled beneath coastal central California as the coherent main part of the Farallon plate continued to subduct deeper into the mantle (Bohannon & Parsons, 1995; Brocher et al., 1999; Van Wijk et al., 2001). In this scenario, late Cenozoic volcanism in the region is linked to the youthfulness of the subducted microplate(s), implying a partial melting mechanism within and directly below the lithospheric lid. Both the slab window (or gap) and stalled microplate hypotheses are based on plate kinematic relationships which require a combination of slab window and stalled oceanic microplate segments (Atwater & Stock, 1998; Bohannon & Parsons, 1995; Brink et al., 1999; Wilson et al., 2005).

The cross-sections presented in Figure 18 show the first-order crustal relations implied by three potential origins for the sub-Crystal Knob mantle lithosphere: *A*. shallowly ascended asthenosphere within the Pacific-Farallon slab window (Atwater & Stock, 1998); *B*. subduction of an underplated, or stalled, Monterey oceanic microplate (Bohannon & Parsons, 1995); or *C*. underplated Farallon plate mantle lithosphere nappe(s) that lie in structural sequence with the upper mantle duplex resolved beneath the Dish Hill xenolith location in the Mojave region (Luffi et al., 2009). Scenarios *A* and *B* have been proposed in previous models of the lithospheric structure of the California coast (Erkan & Blackwell, 2008), while scenario *C* is constructed based on a large body of literature on Cretaceous crustal and mantle-lithosphere tectonics.

4.1. The Neogene Slab Window

Figure 17 shows a hypothetical surface projection of the Pacific-Farallon slab window and partially subducted Monterey plate at ca. 19 Ma (Wilson et al., 2005). The slab window formed by subduction of the trailing edge of the Farallon plate and cessation of seafloor spreading along the former spreading axis with the Pacific plate. According to the Wilson et al. (2005) reconstruction of the Pacific-Farallon slab window and adjacent Monterey plate (Figure 17), the Crystal Knob eruption site was located above a slab window in the early Neogene, ~50–100 km northeast of the northeastern boundary transform fault of the Monterey plate. Diffuse volcanism, some clearly derived from decompression partial melting of convecting mantle, is widespread at this time period across the region of the reconstructed slab window (Cole & Basu, 1995; Hurst, 1982; Sharma et al., 1991; Wilson et al., 2005). However, this phase of slab window opening and related volcanism cannot account for the eruption of the ca. 1.7 Ma Crystal Knob volcanic neck itself (see section 6.3).

4.2. The Monterey plate stalled Slab

When the East Pacific Rise first reached the North American plate at 28.5 Ma, the Monterey microplate broke from the Farallon slab and subducted independently until 19.5 Ma, while rotating clockwise with respect to the Pacific plate (Wilson et al., 2005). Partial subduction and stalling of the Monterey plate occurred along the outer edge of the Franciscan complex to the south of the evolving slab window, and Figure 17 shows the incipient tear between the rotating microplate and the bulk of the downgoing Farallon slab. The relict Monterey Plate slab was integrated into the Pacific plate and translated ~250 km north to outboard of Crystal Knob by slip on the subduction megathrust and the San Gregorio-Hosgri fault (Dickinson et al., 2005; Wilson et al., 2005). The remnant microplate still forms part of the abyssal seafloor in the proximal offshore region (Figure 1).

The eastward extent of the partially subducted Monterey Plate slab is unknown, and it is likely truncated by the San Gregorio-Hosgri fault system (see section 6.1). However, if the Monterey plate extended further eastward and was translated northward beneath a reactivated subduction megathrust (Figure 18b), it would make up the mantle lithosphere beneath Crystal Knob. In its most recent iterations, the stalled slab hypothesis suggests that the Monterey plate extends eastward of the San Andreas Fault as a horizontally translated stalled slab, potentially reaching ~300 km depth beneath the eastern Central Valley (Brink et al., 1999; Pikser et al., 2012; Wang et al., 2013). Although geodynamically suspect, this model has been presented as a candidate for construction of the mantle lithosphere in previous modeling efforts (Erkan & Blackwell, 2008) and is commonly invoked in the seismology literature (e.g., Wang et al., 2013). We include the model in our consideration of thermal history, but return to its viability in section 6.1.

4.3. Underplated Farallon Plate Mantle Nappes

The reconstruction of the Crystal Knob eruption site to its pre-San Andreas position (Figure 17) places it outboard of the Mojave province, where much of the mantle lithosphere was replaced by Farallon plate nappes during Cretaceous time. An outboard extension of this underplating, prior to Neogene transform faulting, is a highly viable alternative for the development of the mantle lithosphere beneath the Coast Ranges.

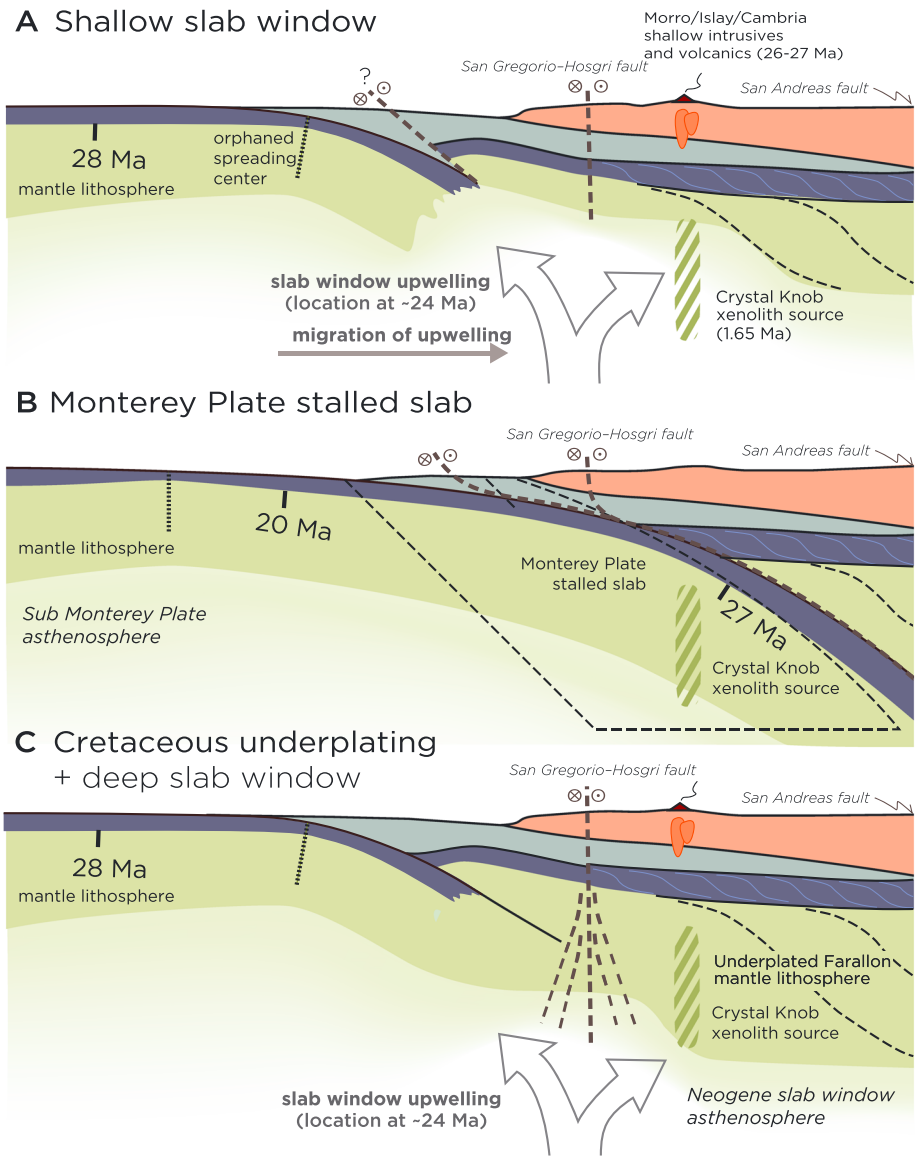

Figure 18. Schematic cross-sections showing potential scenarios for modification of the marginal mantle lithosphere at the end of subduction in the early Miocene. Forearc crust (orange) is generalized for late Cretaceous inherited structure (see Figure 19), including Salina nappes and associated Franciscan-complex fragments. (a) Migration of the East Pacific mantle upwelling beneath the continental margin, forming a slab window and causing wholesale replacement of sub-Salinia mantle lithosphere with ascended asthenosphere. (b) Translation of the Monterey plate stalled slab along the former subduction megathrust to a current position beneath the California Coast Ranges (after Bohannon & Parsons, 1995). (c) Mantle lithosphere beneath the Crystal Knob eruption site composed of underplated Farallon plate mantle nappes reheated at their base by the Neogene slab window. The Monterey plate fragment is translated along the Hosgri fault from the Transverse Ranges region, to have its lithospheric column juxtaposed with previously underplated Farallon plate mantle lithosphere.

The pre-Neogene tectonic setting of the Crystal Knob eruption site is shown in Figure 17 by restoration of the San Andreas dextral transform system relative to North America (Chapman et al., 2012; Dickinson et al., 2005; Matthews, 1976; Hall & Saleeby, 2013; Sharman et al., 2013). The Crystal Knob eruption site restores to a position outboard of the southern California batholith. The principal windows into shallowly underplated subduction channel schists are shown in Figure 17 along with the principal upper plate batholithic exposures. The current western extent of the Salinia crystalline nappes is shown as the Nacimiento fault and the offshore Farallon escarpment. Crystalline rocks of the Salinia nappes extended an unknown distance westward across

the Nacimiento belt Franciscan (Hall & Saleeby, 2013) but were eroded off the lower plate complex as the coastal region rose in the Pliocene (Ducea et al., 2003).

The Crystal Knob neck erupted through the Nacimiento belt of the Franciscan complex, immediately adjacent to the current western limit of Salinia crystalline nappes (Figure 1). Accretion of the Nacimiento belt occurred in the Late Cretaceous beneath the outer reaches of the Salinia nappe sequence (Hall & Saleeby, 2013; Chapman et al., 2016). In their core area, the Salinia nappes rode westward on slightly older, higher metamorphic grade, Franciscan rocks that are shown in Figures 1 and 17 as windows into subduction channel schists (Barth et al., 2003; Kidder & Ducea, 2006; Ducea et al., 2009). The southernmost Sierra Nevada-western Mojave *autochthon* for the Salinia nappes is likewise detached from its original mantle wedge underpinnings and shingled into crystalline nappes that lie on underplated high-grade subduction channel schists (Chapman, 2010; Chapman et al., 2010, 2012; Saleeby, 2003). Tectonic erosion of the mantle wedge followed by shallow subduction underplating of Franciscan rocks requires wholesale replacement of the mantle lithosphere beneath the Mojave province. Luffi et al. (2009) presents petrologic evidence from the Dish Hill and Cima mantle xenolith suites (Figure 1) that suggests the presence of a mantle lithosphere duplex with multiple Farallon plate upper mantle nappes in structural sequence beneath an eastern residual roof of continental mantle lithosphere. Since the crustal structural sequence of the western Mojave region is closely spatially and temporally correlated to that of the Salinia nappes (Chapman et al., 2010, 2012, 2016), it stands to reason that upper mantle duplex accretion progressed westward from the Mojave region to beneath the Salinia nappes as well as the Nacimiento belt of the Franciscan Complex.

4.3.1. Mantle Underplating After Flat Subduction

In Figure 19, we present a model for the tectonic underplating of the Farallon plate mantle lithosphere beneath the Mojave-Salinia-Nacimiento segment of the Late Cretaceous convergent margin (after Saleeby, 2003; Luffi et al., 2009), which occurred in conjunction with shallow flat subduction of the Shatsky Rise conjugate Large Igneous Province (Saleeby, 2003; Liu et al., 2010; Sun et al., 2017). The approximate age of Farallon plate entering the trench is shown on each frame (after Seton et al., 2012). Crustal deformation, timing, and thermal conditions are integrated from Kidder and Ducea (2006), Chapman et al. (2010), Chapman et al. (2012), and Chapman et al. (2016). Figures 19a and 19b show the arrival of the oceanic plateau into the subducting trench and plateau buoyancy-driven shallowing of the subduction megathrust, which drove tectonic erosion of the mantle wedge. During this episode, deep arc rocks cooled rapidly from ~900°C, and temperatures along the flat megathrust were near the ~715°C peak recorded in subduction channel metaclastic rocks of the Sierra de Salinas schist (Kidder & Ducea, 2006).

In Figures 19c and 19d we adopt the focused slab rollback and mantle lithosphere underplating models of Saleeby (2003) and Luffi et al. (2009) for the dynamic response of the forearc to the end of LIP subduction. Gravitational collapse and/or suction by the retreating slab drove crustal responses including large-magnitude, trench-directed extension coupled to regional extrusion of the underplated subduction channel schists. In Figures 19c and 19d transition, accelerated rollback corresponds to the formation of Farallon plate mantle duplexes. Buoyancy-driven resistance to LIP subduction could have driven the transient imbrication of Farallon plate mantle lithosphere and establishment of successive basal megathrust surfaces, leading to forearc overthickening. Alternatively, duplex formation could have occurred due to negative buoyancy during retreating subduction, with tensile stresses in the slab promoting nappe detachment. Observational data and laboratory experiments showing profound coseismic dilation transients along subduction megathrusts (Gabuchian et al., 2017) underscore the ability of tensile stresses to cause dislocations in subducting slabs. We suspect that mantle nappe detachment was mediated by the temperature of the brittle-plastic transition in olivine: for ~40- to 50-Myr oceanic lithosphere entering a subduction zone (Figures 19c and 19d), this ~700–800°C transition (Mei et al., 2010; Warren & Hirth, 2006) occurs at ~25- to 40-km depth in the slab (Doin & Fleitout, 1996).

The lack of high-pressure mafic schists in both the Crystal Knob and Dish Hill xenolith suites further suggests that an intact subduction channel is not preserved in the mantle lithosphere. The seismically imaged, thickened lower crust of the region (Brocher et al., 1999; Tréhu, 1991) may instead originate as underplated slivers of oceanic crust detached along with mantle lithosphere nappes. On the basis of both the regional structural evolution of the central to southern California basement and the petrogenetic history recorded in the region's

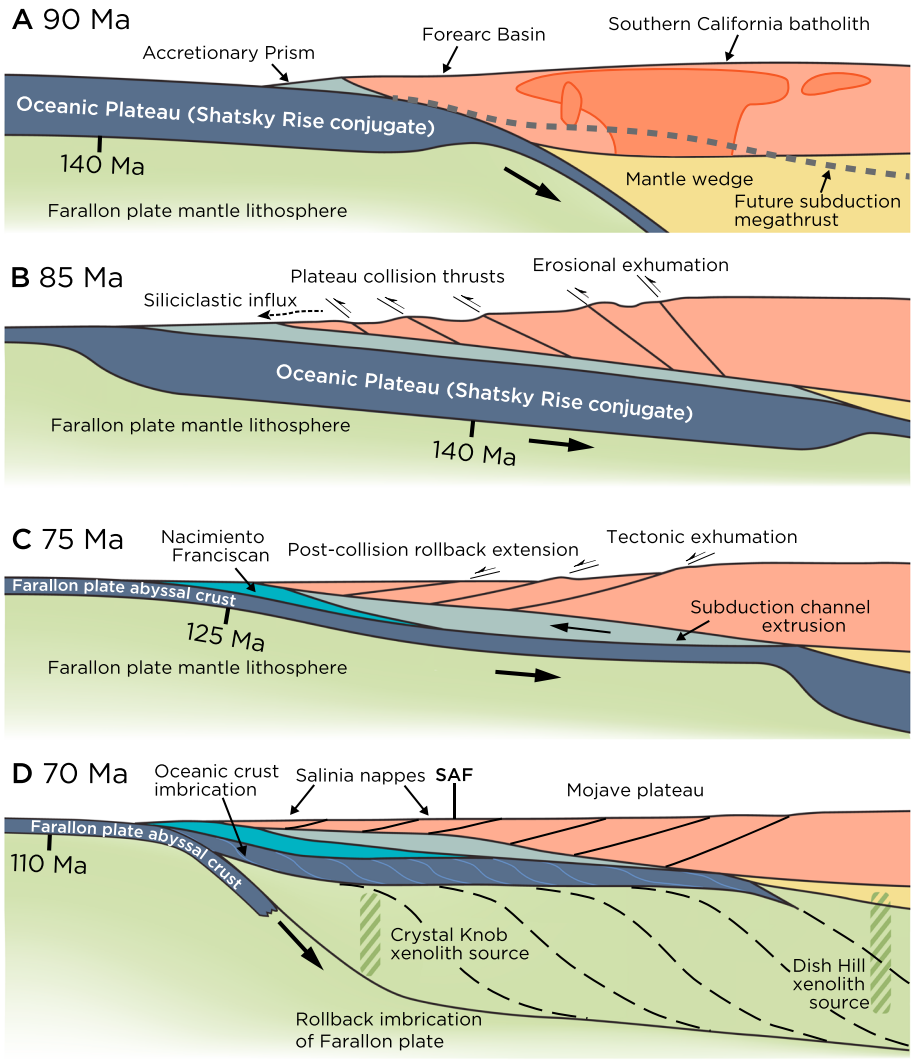

Figure 19. Cross sections showing the evolution of southern California during the subduction of a large oceanic plateau during the late Cretaceous and underplating of Farallon plate mantle nappes during slab rollback (after Chapman et al., 2010; Luffi et al., 2009; Saleeby, 2003).

mantle xenolith suites, we suspect Figure 19d section most accurately represents the construction of the mantle domain sampled by Crystal Knob. This section is idealized for Late Cretaceous time, and we now layer the complexity of late Cenozoic tectonics onto this framework.

4.3.2. A Deep Slab Window Beneath Relict Lithosphere

Kinematic reconstructions of the impingement of the Pacific-Farallon spreading center on the SW Cordilleran subduction zone require a slab window beneath the Crystal Knob eruption site in the early Neogene (Atwater & Stock, 1998; Wilson et al., 2005). Previous modeling of thermal effects of the slab window (Erkan & Blackwell, 2008) only investigated the resulting emplacement of asthenosphere at immediate subcrustal levels. However, the depth of asthenospheric underplating related to slab window opening is poorly constrained and likely varies geographically as a function of thickness and thermal variations in the preexisting lithospheric lid, as well as its state of stress and structural coherence. Volcanism in the central California Coast Ranges tied to slab window opening (e.g., Ernst & Hall, 1974) has been volumetrically insignificant when compared to that generated by other coeval examples of shallow asthenospheric upwelling in the Cordillera, such as Eocene-Miocene high-flux volcanism in the Basin and Range province (e.g., Humphreys, 1995).

An apparent lack of shallow asthenopheric upwelling in the Miocene is readily explained if the slab window opened beneath preexisting mantle lithosphere underplated in the late Cretaceous. This would consist of a tiered duplex of underplated Farallon plate oceanic crust and mantle lithosphere nappes, roofed by the

Nacimiento belt of Franciscan and Salinia nappes. Our estimate of a 45- to 75-km depth interval over which the Crystal Knob lavas sampled the underlying mantle lithosphere, coupled with a general lack of significant late Cenozoic extensional faulting in the immediate region, implies a strong thermomechanical lid that likely suppressed the ascent of voluminous asthenosphere-derived magmas that were hypothetically sourced from a deep underlying slab window.

Figure 18c shows the early Neogene architecture of the mantle lithosphere beneath the Coast Ranges in this scenario. The partially subducted terminus of the Monterey plate is bounded to the east by the San Gregorio-Hosgri fault. East of the fault, the Nacimiento-belt Franciscan complex and its tectonic veneer of Salinia nappes and associated oceanic crustal duplex lie tectonically above underplated Farallon plate mantle nappes. The structural profile shown in Figure 18c closely aligns with offshore seismic lines in the region (Tréhu, 1991), and the part between the San Andreas and San Gregorio-Hosgri Faults restores to southern California latitudes, adjacent to the Mojave Plateau and extended southern California batholith.

5. Thermal Modeling of Tectonic Scenarios

The Crystal Knob mantle xenoliths have a peridotite composition with a depleted (convecting-mantle) isotopic and trace element signature. Petrographic and geochemical variations provide information on the depletion history but cannot discriminate between slab window, Monterey Plate, and Cretaceous mantle duplexing origins of the mantle lithosphere. However, these emplacement scenarios present potentially distinct thermal structures due to large differences in timescales of cooling. Tectonic models for the emplacement of depleted mantle lithosphere under the central California coast can be tested by comparing their implied geothermal structure with xenolith geothermometry.

5.1. Model Setup

To distinguish between potential emplacement mechanisms for the mantle lithosphere sampled by Crystal Knob, we construct a forward model of the geotherm implied by each of the tectonic scenarios discussed in section 4. A model based on the one-dimensional heat flow equation

$$\frac{\partial T}{\partial t} = \frac{k}{\rho C_p}\frac{\partial^2 T}{\partial z^2} + \frac{\alpha}{\rho C_p} \tag{1}$$

(e.g., Turcotte and Schubert (2002), with T: temperature, t: time, and standard values for oceanic and continental material properties shown in Table 10) is used to track the evolution of the lithospheric geotherm predicted by the three tectonic scenarios presented above.

The model is implemented in Python using the FiPy software package (Guyer et al., 2009), combining explicit and implicit finite difference approaches using a two-sweep technique (Crank & Nicolson, 1947) to ensure a stable result. To simulate both subduction and slab window-driven mantle underplating, the forearc geotherm is stacked atop a modeled suboceanic or asthenospheric geotherm and relaxed toward the present. The model is run to a depth of 500 km to remove the effects of unknown mantle heat flux.

A mantle adiabat held at the base of the crust provides a static initial thermal structure for models of scenario *A*, while analytical models for the thermal evolution of oceanic crust (Stein & Stein, 1992) and a forearc geotherm under continuing subduction (Royden, 1993) provide time-dependent boundary conditions for scenarios *B* and *C*. More information about model setup and integration is given in supporting information.

5.2. Model Results

Model results are presented as temperature-time tracers in Figure 20 and as geotherms corresponding to specific model steps in Figure 21.

5.2.1. Shallow Slab Window

The geologic context of the shallow slab window scenario (model group *A*) is shown in Figure 18a, and thermal modeling results are shown in Figure 20a and 21a. The model begins at 24 Ma, corresponding to the opening of the Mendocino slab window under southern California (Wilson et al., 2005). A steady state profile through the crust is truncated by a mantle adiabat to simulate direct contact with the ascended asthenosphere (for 0–6 Myr), after which the domain relaxes conductively to the conclusion of the model. Previous modeling by Erkan and Blackwell (2008) suggests that this scenario yields temperatures too hot to correspond to the modern regional geotherm. We confirm this assessment, finding that this scenario produces extremely

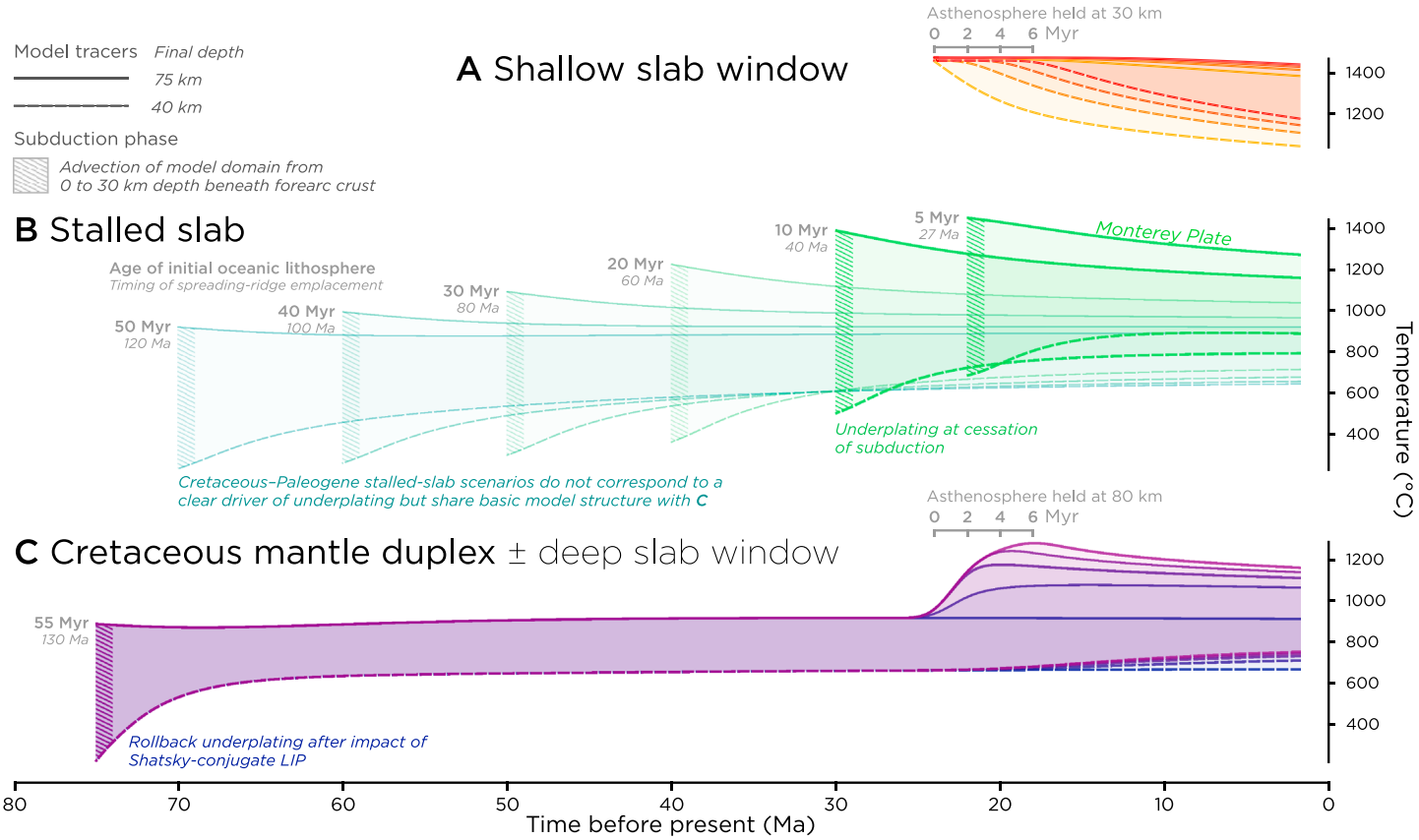

Figure 20. Temperature-time tracers for each modeled scenario, following the evolution of particles at final depths of 40 and 75 km in the model domain (dashed and solid lines, respectively), bracketing the boundary conditions of the Crystal Knob xenolith suite. All models conclude at 1.65 Ma, the eruptive age of the Crystal Knob xenoliths. (a) Upwelling-driven mantle lithosphere replacement to the base of the crust during the Mendocino slab window episode beginning at 24 Ma (Wilson et al., 2005). Asthenospheric mantle is held at the base of the crust for a period of time between 0 and 6 Myr to represent potential durations of active convection. (b) Oceanic lithosphere slices underplated at different times until the Neogene cessation of Farallon plate subduction in the Neogene. The youngest of these scenarios corresponds to the likely thermal evolution of a Monterey Plate stalled slab. The models with subduction times >30 Ma are included for completeness, though they do not correspond to specific events recorded by geologic features in coastal California. Model tracers begin at 10 and 45 km beneath the seafloor and are advected to depths of 40 and 75 km during subduction over the first 1.04 Myr of the model run. (c) A Farallon plate slab subducted and underplated during the late Cretaceous (Figure 19). While similar to the older stalled slab models, it is tuned for key thermobarometric constraints on subduction channel schists (Kidder et al., 2003). The effect of Mendocino slab window upwelling at the base of this section is shown, with timing equivalent to the replacement of the entire mantle lithosphere represented in (a).

steep geotherms at the upper boundary of spinel lherzolite stability for much of the temperature domain of interest (Figure 22), reproducing neither the xenolith pressure-temperature array observed in this study nor the seismically inferred depth of the lithosphere-asthenosphere boundary (e.g., Li et al., 2007).

5.2.2. Neogene Stalled Slab

The geologic context of the stalled slab scenario (model group *B*) is shown in Figure 18b, and modeling results are displayed in Figures 20b and 21b. This scenario tracks the potential thermal structure of oceanic plates stalled under the forearc at a range of times. Each run begins with the subduction of oceanic lithosphere assigned an initial thermal structure corresponding to oceanic lithosphere of a given age.

We model cooling scenarios for a wide range of underplating times, with the start of subduction ranging from 80 to 22 Ma. This reflects the long Cretaceous and Paleogene subduction history of the Farallon plate beneath the central California coast. These subduction times (T_{start}) set the initial conditions shown in Figure 20b and the first panel of Figure 21b. Each model operates on oceanic crust of the appropriate age for the time of subduction, given the Cretaceous to Paleogene geometry of Farallon plate subduction (Liu et al., 2010; Seton et al., 2012). As T_{start} approaches the present, the age of subducted oceanic crust generally decreases, reflecting the approach of the Pacific-Farallon spreading ridge to the western margin of North America.

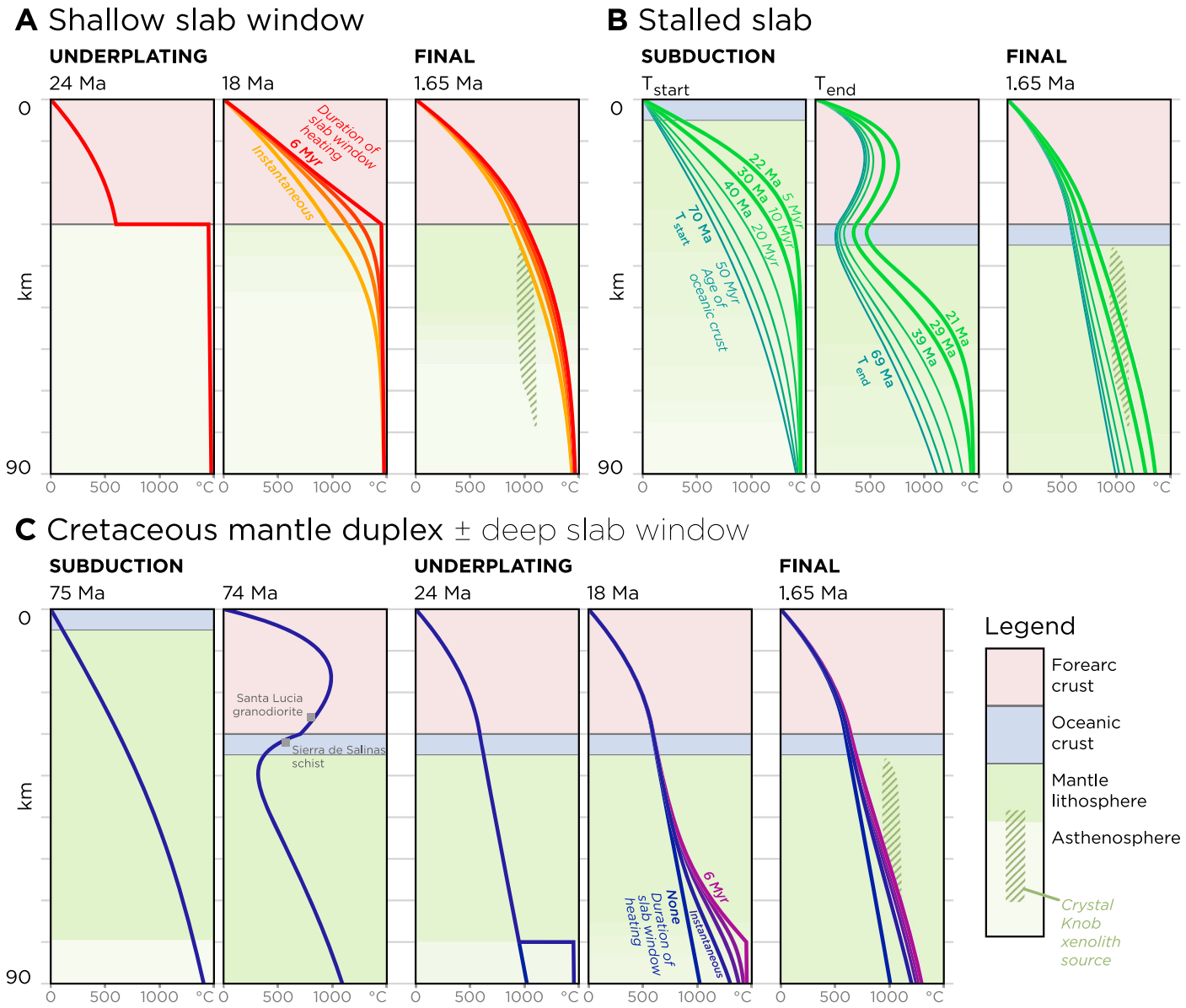

Figure 21. Temperature-depth profiles through the crust and upper mantle at key timesteps during the evolution of the three tectonic scenarios shown in Figure 20. Each profile represents a different model run based on the same scenario. (a) A shallow slab window scenario, with underplating of upwelling asthenosphere truncating a forearc geotherm at 24 Ma. This asthenosphere is held against the base of the crust from 0 to 6 Myr, accounting for the spread of models in the second panel. The final panel tracks all models to the present. (b) Stalled slabs of different ages, with panels corresponding to shared tectonic events, modeled at different times based on the timing of subduction and age of oceanic crust. Subduction is bracketed by T_{start} and T_{end}, with $T_{start} = T_{end} - 1.04$ Myr for all cases. The youngest and hottest of these runs corresponds to the *Monterey plate* tectonic scenario. (c) Farallon Plate mantle lithosphere emplaced beneath the central California coast by mantle duplexing during the late Cretaceous (Figure 19) and reheated by a pulse of heat from below during the Miocene slab window (Figure 18). The second panel, at the end of subduction, shows the geologic temperature constraints used to tune the model to subduction conditions on the late Cretaceous megathrust (e.g., Ducea, 2003, Kidder and Ducea, 2006) In this scenario, oceanic lithosphere is 55 Myr old at the time of subduction.

Stalled slab scenarios with subduction ages older than 30 Ma simulate rollback during sustained Farallon plate subduction. While backstepping of the subduction megathrust and underplating of a slice of mantle lithosphere could, in principle, occur at any time, these older stalled slab models do not correspond to geodynamic and geological evidence of a specific episode of subduction instability. Though improbable, these models are included to fully explore the model space between model groups *B* and *C* and are represented with a reduced opacity on Figure 20b. In the oldest model with a subduction time of 70 Ma, the oceanic lithosphere is 50 Myr old at the time of subduction. At this time,

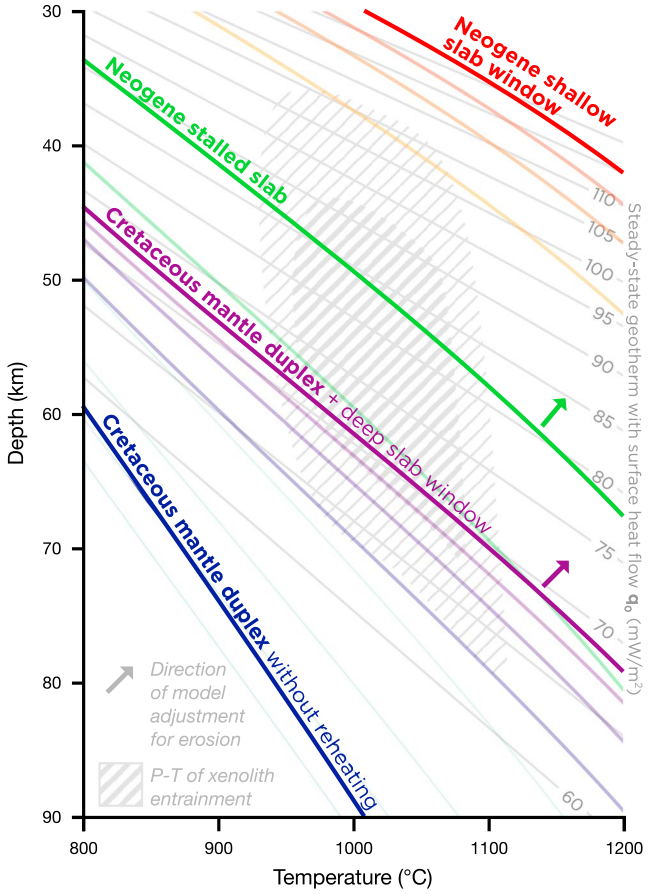

Figure 22. Comparisons of Crystal Knob eruptive (1.65 Ma) sub-Salinia geotherms for each of the modeled scenarios. The hottest model run of each group is highlighted, with cooler models of the same family shown with lower opacity. The model predicts purely conductive geotherms, and arrows show potential response to erosion (see supporting information). The background of the plot shows a range of steady state geotherms anchored to surface heat flows and the likely field of xenolith entrainment (Figure 15).

the Shatsky conjugate had already subducted to beneath the Cordilleran interior (Liu et al., 2010) and the Nacimiento belt of the Franciscan Complex was in its later stages of subduction accretion (Chapman et al., 2016). This is the earliest time a stalled slab could have developed outside of the specific scenario treated in model group *C*.

The youngest model run in Figure 20b corresponds to the Monterey plate hypothesis (Pikser et al., 2012; Van Wijk et al., 2001), which entails hypothetical northward lateral translation on a shallowly dipping remobilized subduction megathrust. The potential thermal effects of the required anhydrous shearing of the underplated oceanic lithosphere along a ~300 km flat displacement trajectory (see section 6.1) are not accounted for in model *B*. Instead, this scenario is modeled simply as a young end-member stalled slab scenario, with generation of mantle lithosphere beneath the oceanic spreading ridge at 27 Ma (corresponding to the chron 7 magnetic anomaly) and subduction shortly thereafter (Atwater & Stock, 1998; Wilson et al., 2005).

Overall, the stalled slab underplating scenarios represented in *B* result in cooler geotherms than shallow slab window underplating, matching the broad thermobarometric constraints placing Crystal Knob xenolith entrainment relatively deep within the spinel stability field (Figure 22). The Monterey plate subduction scenario likewise predicts a modern geotherm that matches the entrainment constraints on the Crystal Knob xenoliths. Without consideration of potential bias toward colder measurements in the modeled geotherms, this appears to match our xenolith data. Accounting for possible external effects (section 3.1 and Supplementary Information), it suggests a hotter geotherm marginally conforming to thermobarometric constraints.

5.2.3. Late Cretaceous Mantle Nappe Underplating

The geologic context of the Late Cretaceous mantle nappe underplating scenario (model group *C*) is shown in Figure 18c, and model results are displayed in Figures 20c and 21c. The initiation of this scenario is similar to the older stalled slab scenarios (Figure 20b). In both cases, the oceanic mantle forms under the Pacific-Farallon spreading ridge during the early Cretaceous, thermally matures to form a mantle lithosphere lid during oceanic plate transport, and subducts beneath the southwest Cordilleran margin later in Cretaceous time. Thus, the initial conditions and thermal evolution of scenario *C* are qualitatively similar to the older runs of *B*, except that this scenario incorporates more crustal geological constraints that pertain to its subduction history. In model *C*, the Royden (1993) forearc geotherm is tied to temperature constraint of 715°C at 25-km depth based on garnet-biotite thermometry of Salinia granites that lie tectonically above the subduction complex and ~575°C at 30-km depth based on garnet-biotite thermobarometry on the proximally underplated schist of Sierra de Salinas (Ducea, 2003; Kidder & Ducea, 2006). The subduction conditions and mantle lithosphere structure implied by this scenario are shown in Figure 19.

In model group *C*, the age of subduction and underplating is taken as 70 Ma, based on the youngest mica Ar/Ar ages for the Sierra de Salinas/Nacimiento Franciscan subduction complex (Barth et al., 2003; Chapman et al., 2010, Chapman, 2016, Chapman et al., 2016; Grove et al., 2003; Saleeby et al., 2007). Seafloor being subducted at that time was 40 Myr old (Liu et al., 2010; Seton et al., 2012). In this tectonic scenario (Figures 18c and 19), Farallon oceanic lithosphere continued to subduct after mantle nappe detachment until the Pacific-Farallon spreading ridge encountered the trench in Neogene time.

In model runs for this scenario (Figure 21), the underplated mantle nappe(s) cool beneath the forearc for 50 Myr, after which the geotherm is perturbed by the underplating of asthenosphere at ~80-km depth, corresponding to a deep slab window. This interaction is modeled by holding an adiabatic temperature gradient

with a mantle potential temperature of 1450°C against the base of the lithosphere for 0—6 Myr. The model for 0 Myr entails instantaneous contact followed immediately by conductive relaxation, while 6 Myr of sustained upwelling produces the *kinked* geotherm seen in panel 4 of Figure 21c at the 18 Ma time step, due to continuing imposition of a mantle adiabat below 80-km depth. A single model without slab window heating predicts much cooler geotherms than allowed by xenolith constraints (Figure 22).

Figure 21c, panel 2, shows the thermobarometric constraints and inverted metamorphic gradient recorded by subduction channel schists for this episode of subduction (Kidder & Ducea, 2006; Kidder et al., 2013) and used to tune the Royden (1993) forearc geotherm model. These high subduction temperatures constrained by crustal geothemometry make little difference to the final thermal structure of the mantle lithosphere (Figure 20c). Without reheating by a deep slab window, the Cretaceous underplating scenario has a similar final thermal structure to the longest-running stalled slab scenarios in *B* (Figure 22), suggesting that high subduction channel temperatures experienced during late Cretaceous flat slab subduction and schist metamorphism did not have a long-lasting impact on the thermal structure of the margin. Thus, heating by a Miocene deep slab window is required for Cretaceous mantle nappe underplating scenarios to produce the mantle lithosphere temperatures sampled by the Crystal Knob xenoliths.

5.3. Summary of Model Results

An assessment of model sensitivity presented in supporting information includes biases that may influence the model results. The largest potential bias is a potential underestimation of true geothermal gradients due to lack of accounting for exhumation during the progression of the model. A correction for this bias would (1) push model results for the slab window scenario further out of the field of acceptable mantle lithosphere geotherms derived from xenolith constraints, (2) push the stalled slab scenario (*B*) to the upper margin of the field, and (3) push the reheated mantle nappe (*C*) toward the centroid of the field. The direction of these adjustments is summarized in Figure 22.

Our thermal modeling predicts much higher temperatures within the mantle lithosphere, and much higher geothermal gradients, for the shallow slab window (scenario *A*) than for either of the other modeled scenarios. Predicted geotherms for the slab window are much higher than mantle lithosphere temperatures measured by xenolith thermobarometry or extrapolated from surface heat flows (Figure 22). We can thus reject a shallow slab window source for the mantle lithosphere sampled by Crystal Knob.

The stalled slab (scenario *B*) and Cretaceous mantle nappes reheated by a deep slab window (scenario *C*) suggest mantle lithosphere temperatures similar to those measured by xenolith thermobarometry and inferred from surface heat flows and seismic tomography. Both scenarios *B* and *C* are acceptable given the thermal modeling. However, the geotherm predicted for the stalled slab occupies the higher-temperature part of the acceptable field, and its viability could be impacted by potential erosion in the Coast Ranges, which would elevate geotherms for all scenarios (Figure 22).

6. Discussion of Lithospheric History

Both the Monterey plate stalled slab (scenario *B*) and Cretaceous underplating of mantle lithosphere followed by heating at depth by the Neogene slab window (scenario *C*) predict plausible mantle lithosphere geotherms beneath the Coast Ranges that match surface heat flow measurements and xenolith thermobarometry.

We strongly prefer scenario *C*, which is informed by the architecture of the lithospheric mantle in the Mojave region (Luffi et al., 2009) and the crustal geologic structure of southern California inherited from Cretaceous tectonics (e.g., Liu et al., 2010, Chapman et al., 2012). The Neogene thermal pulse in scenario *C* also incorporates the geodynamic response of coastal California to Neogene ridge subduction (Atwater & Stock, 1998; Wilson et al., 2005), suggesting an explanation for the lack of large-volume magmatism associated with the Pacific-Farallon slab window.

The plausibility of mantle lithosphere temperatures produced by scenario *B* reproduces the results of previous modeling (Erkan & Blackwell, 2008). However, these workers did not consider a mechanism equivalent to our scenario *C*, which provides a viable alternative. Although we cannot reject the stalled slab model based on

thermal modeling alone, there are many geologic and geodynamic reasons to discount its feasibility, which we detail below.

6.1. Geodynamic Implausibility of the Neogene Stalled Slab

The Monterey plate nucleated along a ~250-km segment of the Pacific-Farallon ridge as an oblique rift that was rotated ~25° clockwise from the Pacific-Farallon rift axis (Atwater & Severinghaus, 1989). Its generation was synchronous with the early stages of Pacific-Farallon plate convergence into the Cordilleran subduction zone along the southern California coastal region, and coincided with transrotational rifting of the continental borderland region and displacement of the western Transverse Ranges bedrock (Bohannon & Parsons, 1995; Atwater & Stock, 1998).

The current position of the Monterey plate offshore of the Crystal Knob eruption site is a result of dextral displacements linked to borderland transrotational rifting, subsequent ~155-km scale dextral offsets along the San Gregorio-Hosgri fault system and ~100 km of additional dextral offsets in the offshore region (Figure 1) as modeled both by geologic reconstruction of fault offsets (Dickinson et al., 2005) and plate kinematic reconstructions (Wilson et al., 2005). Continuation of the Monterey plate east of the San Gregorio-Hosgri fault requires the lateral translation of its downdip extension along the former subduction interface beneath the Coast Ranges. Its hypothetical extension east of the San Andreas Fault requires that this reactivated subduction interface likewise extended east of the San Andreas Fault (e.g., Brocher et al., 1999; Brink et al., 1999; Pikser et al., 2012). Seismological, geodynamic, and surface geological evidence presented here argues against models invoking horizontal translation of the Monterey plate *remnant slab* beneath both the Coast Ranges and Central Valley.

The Monterey microplate separated from the Farallon Plate at ca. 22 Ma, forming a widening slab window segment east of the Peninsular Ranges (Figure 17). From ca. 22 to 10 Ma, the Monterey plate, already coupled to the Pacific plate, diverged from North America (Atwater & Stock, 1998; Wilson et al., 2005). This likely caused extensional attenuation of its subducted extension (Bohannon & Parsons, 1995). Coupling of Monterey plate rotation across the stalled subduction megathrust may have driven dextral transrotational rifting of the southern California borderland (Bohannon & Parsons, 1995; Nicholson et al., 1994).

As western Transverse Range crustal panels rotated to their current position at the end of borderland transrotation (ca. 10 Ma), the Monterey plate was displaced northward along the San Gregorio-Hosgri fault system (Figure 1), which is aligned with the outer edge of the Farallon-Monterey slab window (Figure 17). The abyssal fragment of the Monterey Plate likely separated from its underthrust extension in conjunction with the sudden cessation of crustal transrotation. If the subducted portion of the Monterey Plate instead maintained its structural integrity, it would be translated northward beneath the Coast Ranges on a shallowly dipping fault surface (presumably, the remobilized subduction megathrust) along with its Pacific plate abyssal fragment (Figure 18c) to its current position outboard of Crystal Knob. This geometry has been proposed to extend beneath the entire Coast Ranges and east of the San Andreas Fault (e.g.Brink et al., 1999, Pikser et al., 2012). Although kinematically plausible, this is unlikely based on dynamic factors: a large mantle mass at the base of the crust should cause transients in dynamic topography and brittle crustal deformation in response to coupling across the shallow fault. Such surface deformation patterns are not expressed north of the Transverse Ranges during the Neogene.

Seismic tomography of central California (Tréhu & Wheeler, 1987) suggests an 8- to 15-km-thick, shallowly east dipping mafic lower crustal layer that extends from the offshore region toward the San Andreas Fault, thickening eastward over Moho depths of ~12–30 km. This layer could represent the continuous surface of the stalled Monterey plate beneath coastal central California (Brocher et al., 1999). However, strong internal reflectivity within this mafic layer (Brocher et al., 1999; Tréhu & Wheeler, 1987) and sharp inflections in its upper surface (Tréhu, 1991) indicate that it is internally deformed and imbricated. It is accordingly 2 to 3 times as thick as typical mafic oceanic crust. Such imbrication and underplating require a basal detachment, which is most logically located at the underlying Moho. In this context, the regions's lower crustal mafic layer is more plausibly interpreted as a regional underplated duplex of Farallon plate oceanic crustal nappes that accreted during Franciscan subduction (Figure 18c).

Distinct steps and inflections in lower crustal velocity structure across the San Gregorio-Hosgri fault system (Brocher et al., 1999) indicate that it cuts the entire crust, likely forming the eastern boundary of the underplated Monterey plate. Additionally, offshore seismic observations show a ~16° eastward dipping Monterey

plate, with a typical abyssal crustal thickness, juxtaposed against a nearly flat thickened lower crustal layer beneath the adjacent Franciscan complex (Tréhu, 1991; Nicholson et al., 1992). These observations directly conflict with the idea that a structurally continuous Monterey Plate constitutes the lower crust beneath central coastal California and the adjacent offshore region.

Studies proposing a deep Monterey plate stalled slab (e.g., Furlong et al., 1989; Pikser et al., 2012) have suggested its translation on significant subhorizontal fault segments beneath the San Andreas system that accommodated dextral displacements. As of yet, however, all seismically imaged segments of the transform system have been shown to be steeply oriented (Brocher et al., 1999; Dietz & Ellsworth, 1990; Ozacar & Zandt, 2009; Titus et al., 2007; Yan et al., 2005; Yan & Clayton, 2007). These studies typically propose a steeply dipping eastward extension corresponding to the high wave speed anomaly of the southern Sierra Nevada-Great Valley region (Figure 1), commonly called the *Isabella anomaly*.

Seismological and geodynamic studies show that the Isabella anomaly is derived primarily from the convectively mobilized mantle wedge, or mantle lithosphere, of the southern Sierra Nevada batholith (Frassetto et al., 2011; Gilbert et al., 2012; Jones et al., 2014; Levandowski & Jones, 2015; Saleeby et al., 2012; Zandt et al., 2004).These studies show structural continuity between the seismic anomaly and the residual mantle lithosphere that is still in place beneath the Central Valley and Sierra Nevada (Figure 1) and suggest that the 200 km deep by 100 km wide Isabella anomaly far exceeds the reasonable size of an attenuated terminus of the Monterey Plate. These studies also provide mechanisms for lower crustal plastic deformation, observable surface faulting, upper mantle-lower crustal partial melting, and dynamic topographic effects that are ignored in the stalled slab hypothesis.

First-order geological effects such as volcanism and topographic transients are closely correlated to the convective mobilization of the sub-Sierran mantle lithosphere and its current expression as the Isabella anomaly (Cecil et al., 2014; Ducea & Saleeby, 1998a; Farmer et al., 2002; Levandowski & Jones, 2015; Saleeby et al., 2013). The surface effects of Monterey plate partial subduction, followed by transtensional coupling to the Pacific plate, are closely correlated to transrotational rifting in the southern California Borderland and the linked clockwise rotation of the western Transverse Ranges (Bohannon & Parsons, 1995; Wilson et al., 2005). This supports a Monterey slab with a limited downdip extent, bounded by the Monterey-Farallon slab window segment (Figure 17). If the hypothetical Monterey *relict slab* extended far enough inland to form the Isabella anomaly, its effects on surface geology should not be restricted to the Borderland and Transverse Ranges. Epeirogenic transients that correlate to the convective mobilization of the sub-Sierran mantle lithosphere as the Isabella anomaly are highly out of phase with the predicted translation pattern for a deep Monterey slab (Saleeby et al., 2013; Cecil et al., 2014). Possible remnants of necked-off, partially subducted Monterey plate are more plausibly correlated to the Transverse Ranges high wave speed anomaly in terms of position and volume (Figure 1) and also have a firm geodynamic basis as such (Burkett & Billen, 2009).

The stalled slab hypothesis has provided an explanation for the limited Neogene volcanism and low modern crustal heat flow observed in the Coast Ranges, neither of which can correspond the shallow emplacement of asthenosphere within a slab window (Brocher et al., 1999; Erkan & Blackwell, 2008). These observations can also be explained by the interaction of the slab window with the base of a preexisting mantle lithosphere domain attached to the continental margin, such as the Cretaceous-underplated lithospheric duplexes envisioned in Scenario *C*. Based on the geologic and geodynamic factors discussed above, we reject the stalled slab as a potential mechanism for underplating the mantle lithosphere beneath the central Coast Ranges.

6.2. Thermal Events Recorded by Xenolith Petrology

The Crystal Knob xenolith suite shows petrologic variation consistent with reheating from below, possibly due to interaction of a deep slab window with a thick preexisting lithospheric lid from which the xenoliths were sourced. Increasing depletion with depth in the Crystal Knob sample set does not match the signature of simple decompression melting (section 3.4) and sample CK-6 experienced polyphase major element refertilization by fractionated melt presumably generated below its entrainment depth. At the same time, low levels of re-enrichment by alkali-basalt-like melt are evident across the sample set. Deep partial melting and alkalic melt generation are common features of slab window volcanism (Hole et al., 1991) and may contribute to the signature of depletion and re-enrichment recorded by the Crystal Knob xenoliths.

The highly fractionated, alkalic magma of the Crystal Knob pipe and its entrainment of both dunite cumulates and spinel peridotite xenoliths suggest that it was sourced from a multitiered network within the mantle litho-

sphere at depths >45 km. The fractally scaled melt migration channels investigated by Kelemen et al. (2000) provide a good potential model, in which cumulates are sometimes re-entrained by small-volume volcanism during progressive upward percolation of melt from a deep mantle source. A deep, slowly cooling body of slab window material, locally mobilized as melt and rising through a thick lid of relict mantle lithosphere, provides a mechanism for both mid-Miocene hypabyssal intrusives (Stanley et al., 2000; Ernst & Hall, 1974) and later deeply sourced, small-volume eruptions such as Crystal Knob.

6.3. The Timing of the Crystal Knob Eruption

Although potentially sourced from slowly rising slab window melts, the ca. 1.65 Ma eruption of Crystal Knob (and other Plio-Pleistocene volcanic eruptions in the Coast Ranges) was likely proximally triggered by recent tectonism. Rapid uplift of the central California coastal region at ca. 2 Ma (Ducea et al., 2003) could have caused decompression melting in the lower lithosphere. Additionally, Neogene dextral faulting provides a localized mechanism for transient decompression leading to mobilization of small volumes of mantle lithosphere melt. Crystal Knob is located ~15 km east of the Hosgri fault, and its host Franciscan complex is pervasively cut by faults and shear zones (Cowan, 1978; Seiders, 1989). The Hosgri fault was likely active during the eruption of the Crystal Knob neck (Dickinson et al., 2005; Hardebeck, 2010), and theoretical and observational data on intracontinental transform faults (Platt & Behr, 2011; Titus et al., 2007) indicate that Hosgri fault shear could be distributed across tens of kilometers laterally in the lower crust and upper mantle (Figure 18c).

Elsewhere in the Coast Ranges, Plio-Pleistocene eruptions of small-volume basalts are associated with the traces of active faults. This includes the Coyote Lake pipe (Figure 1), which occurred ~150 km north of Crystal Knob along the San Andreas-Calaveras fault bifurcation zone and entrained lower crust and upper mantle xenoliths (Jové & Coleman, 1998; Titus et al., 2007). As at Crystal Knob, xenoliths recovered from these flows record partial melting of the mantle markedly postdating any possible slab window opening. The interplay of localized extensional transients with deep, low-volume melts is consistent with infrequent but energetic recent volcanism in the Coast Ranges.

7. Conclusion

The lithospheric structure of southern California, to first order created by Cretaceous convergent margin tectonics, was severely overprinted by two subsequent tectonic episodes: the two subsequent tectonic episodes impact and subduction of the Shatsky Rise large igneous province conjugate during the Late Cretaceous and the progressive Neogene evolution of a transform boundary. These episodes have remade the crustal architecture of southern California and the central California Coast Ranges outboard of the San Andreas Fault. Using constraints from the Crystal Knob xenolith suite along with thermal modeling of tectonic scenarios, we show that the mantle lithosphere beneath the central California coast was created during late Cretaceous time and heated by a Neogene asthenospheric pulse.

The Crystal Knob xenolith suite was entrained along a depth gradient from ~45 to 75 km and erupted at 1.65 Ma. It has the isotopic signature of the depleted convecting mantle, which is typical of mid-ocean ridges or shallowly ascended asthenosphere. Samples are variably depleted by partial melting, and trace element re-enrichment (and a single example of likely major element assimilation) suggests interaction with low-volume melts after the formation and initial thermal equilibration of this mantle lithosphere material.

Major element, trace element, and radiogenic isotope data for the Crystal Knob xenolith suite equally satisfy the first-order geochemical features of the shallow slab window, stalled slab, and Late Cretaceous mantle duplex tectonic scenarios. Xenolith pressure-temperature constraints, thermal modeling, and geochemical signatures of depletion and re-enrichment together allow some discrimination between these scenarios. Thermal modeling of a shallowly underplated slab window predicts extremely hot geotherms that are untenable for the xenolith constraints of this study, while the stalled slab and mantle nappe scenarios are both reasonable. When the effects of potential exhumation/erosion are qualitatively considered, the Monterey plate stalled slab end-member scenario corresponds less well to constraints on the upper mantle geotherm. This, along with the poor correspondence of a stalled slab to crustal geology and geodynamic constraints, leads us to strongly favor the Late Cretaceous mantle duplex underplating scenario, with Neogene reheating by a deep slab window.

A late Cretaceous origin of the mantle lithosphere beneath the Coast Ranges (our scenario *C*) matches crustal geologic evidence of Late Cretaceous slab rollback and regional extension, as the Shatsky Rise conjugate

subducted deeper into the mantle following its initial collision and shallow subduction beneath the southern California convergent margin. This episode built the mantle lithosphere beneath the Mojave province Desert by duplexing during the retreat of the Farallon Plate subducting slab (Luffi et al., 2009) and appears to have subsequently built the outboard mantle lithosphere beneath the Crystal Knob eruption site. The presence of underplated Cretaceous mantle lithosphere beneath the Coast Ranges confirms that the entire lithospheric column, including the Salinia nappes and Nacimiento belt of the Franciscan complex, was formed in a single episode of extension during Late Cretaceous time. The outer toe of this extensionally collapsed accretionary belt was subsequently displaced along the San Andreas transform system to its current location beneath the central California Coast Ranges.

The deep mantle lithosphere beneath coastal central California, appended during Cretaceous time, was reheated by the Neogene opening of the Mendocino slab window. As the Pacific-Farallon ridge encountered the California convergent margin, the relatively cool underplated mantle lithosphere shielded the crust from intense slab window heating and volcanism. Peridotite major and trace element re-enrichment and abundant dunite cumulate xenoliths and xenocrysts within the Crystal Knob basalt record the percolation of fluids and melts through the lithosphere. This percolation, the highly fractionated Crystal Knob basaltic pipe, and the modeled thermal pulse at the base of the lithosphere can be attributed to the ca. 24 Ma opening of an asthenospheric slab window at 70- to 90-km depth. This interaction of the slab window with the base of an integrated lithospheric column could explain the relatively subdued response of coastal California to Neogene ridge subduction.

Acknowledgments
We would like to thank M. Cosca and the USGS Argon geochronology laboratory for their assistance with dating the Crystal Knob basalt flow. J. Blundy and M. Gurnis were valuable resources on REE thermometry and geodynamic modeling, respectively. F. Sousa and J. Price encouraged consideration of the wider tectonic context. We would also like to thank A. Chapman, E. Nadin, and one anonymous reviewer for their excellent feedback, which greatly improved this contribution. This work was supported by the Caltech Tectonics Observatory and funded by the Gordon and Betty Moore Foundation through grant GBMF423.01. A PostgreSQL database containing analytical data and modeling results is archived with CaltechDATA at DOI 10.22002/D1.320. Data reduction, modeling, and graphics compilation code is at 10.22002/D1.321.

References

Ague, J. J., & Brimhall, G. H. (1988). Magmatic arc asymmetry and distribution of anomalous plutonic belts in the batholiths of California: Effects of assimilation, crustal thickness, and depth of crystallization. *Bulletin of the Geological Society of America*, *100*(6), 912–927. https://doi.org/10.1130/0016-7606(1988)100<0912:MAAADO>2.3.CO;2

Alibert, C. (1994). Peridotite xenoliths from western Grand Canyon and the Thumb: A probe into the subcontinental mantle of the Colorado Plateau. *Journal of Geophysical Research*, *99*(B11), 21,605–21,620. https://doi.org/10.1029/94jb01555

Argus, D. F., & Gordon, R. G. (1991). Current Sierra Nevada-North America motion from very long baseline interferometry: Implications for the kinematics of the western United States. *Geology*, *19*(11), 1085. https://doi.org/10.1130/0091-7613(1991)019<1085:csnnam>2.3.co;2

Armstrong, J. T. (1988). *Quantitative analysis of silicate and oxide materials: Comparison of Monte Carlo, ZAF, and Phi-Rho-Z Procedures, in Microbeam Analysis*, pp. 239–246. San Francisco: San Francisco Press.

Armytage, R. M. G., Brandon, A. D., Andreasen, R., & Lapen, T. J. (2015). Evolution of Mojavian mantle lithosphere influenced by Farallon plate subduction: Evidence from Hf and Nd isotopes in peridotite xenoliths from Dish Hill, CA. *Geochimica et Cosmochimica Acta*, *159*, 264–284.

Asimow, P. (1999). A model that reconciles major-and trace-element data from abyssal peridotites. *Earth and Planetary Science Letters*, *169*, 303–319.

Atwater, T. (1970). Implications of plate tectonics for the Cenozoic tectonic evolution of western North America. *Geological Society of America Bulletin*, *81*(12), 3513–3536. https://doi.org/10.1130/0016-7606(1970)81

Atwater, T., & Severinghaus, J. (1989). Tectonic maps of the northeast Pacific, in The Geology of North America, Vol. N. In E. Winterer, D. Hussong, & R. Decker (Eds.), *The Eastern Pacific Ocean and Hawaii* (pp. 15–20). Boulder, CO: Geological Society of America. https://doi.org/10.1130/dnag-gna-n.15

Atwater, T., & Stock, J. (1998). Pacific-North America plate tectonics of the Neogene southwestern United States: An update. *International Geology Review*, *40*(5), 375–402. https://doi.org/10.1080/00206819809465216

Baker, M. B., & Beckett, J. R. (1999). The origin of abyssal peridotites: A reinterpretation of constraints based on primary bulk compositions. *Earth and Planetary Science Letters*, *171*(1), 49–61. https://doi.org/10.1016/S0012-821X(99)00130-2

Barbeau, D. L., Ducea, M. N., Gehrels, G. E., Kidder, S., Wetmore, P. H., & Saleeby, J. B. (2005). U-Pb detrital-zircon geochronology of northern Salinian basement and cover rocks. *Geological Society of America Bulletin*, *117*(3), 466. https://doi.org/10.1130/b25496.1

Barth, A. P., Wooden, J. L., Grove, M., Jacobson, C. E., & Pedrick, J. N. (2003). U-Pb zircon geochronology of rocks in the Salinas Valley region of California: A reevaluation of the crustal structure and origin of the Salinian block. *Geology*, *31*(6), 517.

Beard, B. L., & Glazner, A. F. (1995). Trace element and Sr and Nd isotopic composition of mantle xenoliths from the Big Pine Volcanic Field, California. *Journal of Geophysical Research: Solid Earth*, *100*(B3), 4169–4179. https://doi.org/10.1029/94JB02883

Blackwell, D., & Richards, M. (2004). Geothermal map of North America.

Blake, M. C. J., Jayko, A. S., McLaughlin, R. J., & Underwood, M. B. (1988). Metamorphic and tectonic evolution of the Franciscan Complex, northern California. In *Metamorphism and crustal evolution of the Western United States* (Vol. 8, pp. 1035–1060). New Jersey: Prentice-Hall Englewood Cliffs.

Blundy, J., & Wood, B. (2003). Partitioning of trace elements between crystals and melts. *Earth and Planetary Science Letters*, *210*(3-4), 383–397. https://doi.org/10.1016/S0012-821X(03)00129-8

Bohannon, R. G., & Parsons, T. (1995). Tectonic implications of post-30 Ma Pacific and North American relative plate motions. *Geological Society of America Bulletin*, *107*(8), 937–959. https://doi.org/10.1130/0016-7606(1995)107<0937:TIOPMP>2.3.CO;2

Borghini, G., Fumagalli, P., & Rampone, E. (2009). The stability of plagioclase in the upper mantle: Subsolidus experiments on fertile and depleted lherzolite. *Journal of Petrology*, *5*(1-2), 229–254. https://doi.org/10.1093/petrology/egp079

Brady, R. J., Ducea, M. N., Kidder, S. B., & Saleeby, J. B. (2006). The distribution of radiogenic heat production as a function of depth in the Sierra Nevada Batholith, California. *Lithos*, *86*(3-4), 229–244. https://doi.org/10.1016/j.lithos.2005.06.003

Brey, G., & Köler, T. (1990). Geothermobarometry in four-phase lherzolites II. New thermobarometers, and practical assessment of existing thermobarometers. *Journal of Petrology*, *31*(c), 1353–1378.

Brocher, T. M. . U. S., Brink, T. B., & Abramovitz, T. (1999). Synthesis of crustal seismic structure and implications for the concept of a slab gap beneath coastal California. *International Geology Review*, *41*(3), 263–274. https://doi.org/10.1080/00206819909465142

Burkett, E. R., & Billen, M. I. (2009). Dynamics and implications of slab detachment due to ridge-trench collision. *Journal of Geophysical Research*, *114*(12), 1–16. https://doi.org/10.1029/2009JB006402

Cecil, M. R., Saleeby, Z., Saleeby, J., & Farley, K. A. (2014). Pliocene-Quaternary subsidence and exhumation of the southeastern San Joaquin Basin, California, in response to mantle lithosphere removal. *Geosphere*, *10*(1), 129–147. https://doi.org/10.1130/GES00882.1

Chapman, A., Saleeby, J., Wood, D., Piasecki, A., Kidder, S., Ducea, M., & Farley, K. (2012). Late Cretaceous gravitational collapse of the southern Sierra Nevada batholith, California. *Geosphere*, *8*(2), 314–341. https://doi.org/10.1130/GES00740.1

Chapman, A. D. (2016). The Pelona-Orocopia-Rand and related schists of southern California: A review of the best-known archive of shallow subduction on the planet. *International Geology Review*, *59*, 664–701. https://doi.org/10.1080/00206814.2016.1230836

Chapman, A. D., Kidder, S., Saleeby, J. B., & Ducea, M. N. (2010). Role of extrusion of the Rand and Sierra de Salinas schists in Late Cretaceous extension and rotation of the southern Sierra Nevada and vicinity. *Tectonics*, *29*(5), 1–21. https://doi.org/10.1029/2009TC002597

Chapman, A. D., Saleeby, J. B., & Eiler, J. (2013). Slab flattening trigger for isotopic disturbance and magmatic flare-up in the southernmost Sierra Nevada batholith, California. *Geology*, *41*(9), 1007–1010. https://doi.org/10.1130/g34445.1

Chapman, A. D., Ducea, M. N., Kidder, S., & Petrescu, L. (2014). Geochemical constraints on the petrogenesis of the Salinian arc, central California: Implications for the origin of intermediate magmas. *Lithos*, *200-201*, 126–141. https://doi.org/10.1016/j.lithos.2014.04.011

Chapman, A. D., Jacobson, C. E., Ernst, W., Grove, M., Dumitru, T., Hourigan, J., & Ducea, M. N. (2016). Assembling the world's type shallow subduction complex: Detrital zircon geochronologic constraints on the origin of the Nacimiento block, central California Coast Ranges. *Geosphere*, *12*(2), GES01,257.1. https://doi.org/10.1130/GES01257.1

Chapman, A. D., Wood, D., Saleeby, J. B., & Saleeby, Z. (2016). *Late Cretaceous to early Neogene tectonic development of the southern Sierra Nevada region, in Geological Society of America Fieldtrip Guide* (Vol. 7). California: Ontario.

Chin, E., Lee, C.-T., & Blichert-Toft, J. (2015). Growth of upper plate lithosphere controls tempo of arc magmatism: Constraints from Al-diffusion kinetics and coupled Lu-Hf and Sm-Nd chronology. *Geochemical Perspectives Letters*, *1*(1), 20–32. https://doi.org/10.7185/geochemlet.1503

Cole, R. B., & Basu, A. R. (1995). Nd-Sr isotopic geochemistry and tectonics of ridge subduction and middle Cenozoic volcanism in western California. *Geological Society of America Bulletin*, *107*(2), 167–179. https://doi.org/10.1130/0016-7606(1995)107<0167:NSIGAT>2.3.CO;2

Cosca, M., Stunitz, H., Bourgeix, A.-L., & Lee, J. P. (2011). 40Ar loss in experimentally deformed muscovite and biotite with implications for 40Ar/39Ar geochronology of naturally deformed rocks. *Geochimica et Cosmochimica Acta*, *75*, 7759–7778. https://doi.org/10.1016/j.gca.2011.10.012

Cowan, D. S. (1978). Origin of blueschist-bearing chaotic rocks in the Franciscan Complex, San Simeon, California. *Geological Society of America Bulletin*, *89*(9), 1415. https://doi.org/10.1130/0016-7606(1978)89<1415:oobcri>2.0.co;2

Crank, J., & Nicolson, P. (1947). A practical method for numerical evaluation of solutions of partial differential equations of the heat-conduction type. *Mathematical Proceedings of the Cambridge Philosophical Society*, *43*(01), 50–67.

DePaolo, D., & Wasserburg, G. (1976). Inferences about magma sources and mantle structure from variations of 143Nd/144Nd. *Geophysical Research Letters*, *3*(12).

Dick, H., & Bullen, T. (1984). Chromian spinel as a petrogenetic indicator in abyssal and alpine-type peridotites and spatially associated lavas. *Contributions to Mineralogy and Petrology*, *86*, 54–76.

Dickinson, W., Ducea, M. N., Rosenberg, L. I., Greene, G. H., Graham, S. A., Clark, J. C., et al. (2005). Net dextral slip, Neogene San Gregorio-Hosgri fault zone, coastal California: Geologic evidence and tectonic implications. *Geological Society of America Special Papers*, *391*, 43. https://doi.org/10.1130/2005.2391

Dietz, L. D., & Ellsworth, W. L. (1990). *Geophysical Research Letters*, *17*(9), 1417–1420. https://doi.org/10.1029/gl017i009p01417

Dodge, F. (1988). Fragments of the mantle and crust from beneath the Sierra Nevada batholith: Xenoliths in a volcanic pipe near Big Creek, California. *Geological Society of America Bulletin*. https://doi.org/10.1130/0016-7606(1988)100<0938

Doin, M. P., & Fleitout, L. (1996). Thermal evolution of the oceanic lithosphere: An alternative view. *Earth and Planetary Science Letters*, *142*(1-2), 121–136. https://doi.org/10.1016/0012-821x(96)00082-9

Drew, S. T., Ducea, M. N., & Schoenbohm, L. M. (2009). Mafic volcanism on the Puna Plateau, NW Argentina: Implications for lithospheric composition and evolution with an emphasis on lithospheric foundering. *Lithosphere*, *1*, 305–318.

Ducea, M., & Saleeby, J. (1996). Buoyancy sources for a large, unrooted mountain range, the Sierra Nevada, California: Evidence from xenolith thermobarometry. *Journal of Geophysical Research*, *101*(B4), 8229–8244.

Ducea, M., & Saleeby, J. (1998a). A case for delamination of the deep batholithic crust beneath the Sierra Nevada, California. *International Geology Review*, *40*(1), 78–93. https://doi.org/10.1080/00206819809465199

Ducea, M., House, M. A., & Kidder, S. (2003). Late Cenozoic denudation and uplift rates in the Santa Lucia Mountains California. *Geology*, *31*(2), 139. https://doi.org/10.1130/0091-7613(2003)031<0139:lcdaur>2.0.co;2

Ducea, M. N. (2003). Arc composition at mid-crustal depths: Insights from the Coast Ridge Belt, Santa Lucia Mountains, California. *Geophysical Research Letters*, *30*(13), 0–3.

Ducea, M. N., & Saleeby, J. B. (1998b). The age and origin of a thick mafic-ultramafic keel from beneath the Sierra Nevada batholith. *Contributions in Mineralogy and Petrology*, *133*, 169–185.

Ducea, M. N., Kidder, S., Chesley, J. T., & Saleeby, J. B. (2009). Tectonic underplating of trench sediments beneath magmatic arcs: The central California example. *International Geology Review*, *51*(1), 1–26. https://doi.org/10.1080/00206810802602767

Ducea, M. N., Saleeby, J. B., & Bergantz, G. (2015). The architecture, chemistry, and evolution of continental magmatic arcs. *Annual Review of Earth and Planetary Sciences*, *43*, 299–333. https://doi.org/10.1146/annurev-earth-060614-105049

England, P., & Molnar, P. (1990). Surface uplift, uplift of rocks, and exhumation of rocks. *Geology*, *18*(12), 1173–1177. https://doi.org/10.1130/0091-7613(1990)018<1173:SUUORA>2.3.CO

Erkan, K., & Blackwell, D. (2009). Transient thermal regimes in the Sierra Nevada and Baja California extinct outer arcs following the cessation of Farallon subduction. *Journal of Geophysical Research*, *114*(B2), B02,107. https://doi.org/10.1029/2007JB005498

Erkan, K., & Blackwell, D. D. (2008). A thermal test of the post-subduction tectonic evolution along the California transform margin. *Geophysical Research Letters*, *35*(7). https://doi.org/10.1029/2008GL033479

Ernst, W. G., & Hall, C. A. (1974). Geology and petrology of the Cambria Felsite, a new Oligocene formation, west-central California Coast Ranges. *Bulletin of the Geological Society of America*, *85*(4), 523–532. https://doi.org/10.1130/0016-7606(1974)85<523:GAPOTC>2.0.CO;2

Farmer, G. L., Glazner, A. F., Wilshire, H. G., Wooden, J. L., Pickthorn, W. J., & Katz, M (1995). Origin of late Cenozoic basalts at the Cima volcanic field, Mojave Desert, California. *Journal of Geophysical Research*, *100*(B5), 8399. https://doi.org/10.1029/95JB00070

Farmer, G. L., Glazner, A. F., & Manley, C. R. (2002). Did lithospheric delamination trigger late Cenozoic potassic volcanism in the southern Sierra Nevada, California? *Geological Society of America Bulletin*, *114*(6), 754–768. https://doi.org/10.1130/0016-7606(2002)114<0754:dldtlc>2.0.co;2

Fischer, K. M., Ford, H. A., Abt, D. L., & Rychert, C. A. (2010). The lithosphere-asthenosphere boundary. *Annual Review of Earth and Planetary Sciences*, *38*(1), 551–575. https://doi.org/10.1146/annurev-earth-040809-152438

Fowler, C. (2005). *The solid Earth: An introduction to global geophysics* (1st ed.). Cambridge: Cambridge University Press.

Frassetto, A. M., Zandt, G., Gilbert, H., Owens, T. J., & Jones, C. H. (2011). Structure of the Sierra Nevada from receiver functions and implications for lithospheric foundering. *Geosphere*, *7*, 898–921. https://doi.org/10.1130/ges00570.1

Frey, F. A., & Prinz, M. (1978). Ultramafic inclusions from San Carlos, Arizona—Petrologic and geochemical data bearing on their petrogenesis. *Earth and Planetary Science Letters*, *38*, 129–176. https://doi.org/10.1016/0012-821X(78)90130-9

Furlong, K. P., Hugo, W. D., & Zandt, G. (1989). Geometry and evolution of the San Andreas Fault Zone in northern California. *Journal of Geophysical Research*, *94*(B3), 3100–3110. https://doi.org/10.1029/jb094ib03p03100

Gabuchian, V., Rosakis, A. J., Bhat, H. S., Madariaga, R., & Kanamori, H. (2017). Experimental evidence that thrust earthquake ruptures might open faults. *Nature*, *545*, 336–339.

Galer, S. J. G., & O'Nions, R. K. (1989). Chemical and isotopic studies of ultramafic inclusions from the San Carlos Volcanic Field, Arizona: A bearing on their petrogenesis. *Journal of Petrology*, *30*(4), 1033–1064. https://doi.org/10.1093/petrology/30.4.1033

Gao, S., Günther, D., Chen, L., & Hu, S. (2002). Determination of forty two major and trace elements in USGS and NIST SRM glasses by laser ablation-inductively coupled plasma-mass spectrometry. *Geostandards and Geoanalytical Research*, *26*(2), 181–196. https://doi.org/10.1111/j.1751-908X.2002.tb00886.x

Gasparik, T. (2000). An internally consistent thermodynamic model for the system CaOâSiO2 derived primarily from phase equilibrium data. *The Journal of Geology*, *108*, 103–119.

Gilbert, H., Yang, Y., Forsyth, D. W., Jones, C. H., Owens, T. J., Zandt, G., & Stachnik, J. C. (2012). Imaging lithospheric foundering in the structure of the Sierra Nevada. *Geosphere*, *8*, 1310–1330. https://doi.org/10.1130/GES00790.1

Glazner, A. F (1991). Plutonism, oblique subduction, and continental growth: An example from the Mesozoic of California. *Geology*, *19*, 784–786. https://doi.org/10.1130/0091-7613(1991)019<0784

Goes, S., & van der Lee, S. (2002). Lee Thermal structure of the North American uppermost mantle inferred from seismic tomography. *Journal of Geophysical Research*, *107*.

Green, D., & Ringwood, A. (1970). Mineralogy of peridotitic compositions under upper mantle conditions. *Physics of the Earth and Planetary Interiors*, *3*, 359–371. https://doi.org/10.1016/0031-9201(70)90076-2

Grove, M., Jacobson, C. E., Barth, A. P., & Vucic, A. (2003). Temporal and spatial trends of Late Cretaceous-early Tertiary underplating of Pelona and related schist beneath southern California and southwestern Arizona. *Tectonic Evolution of Northwestern Mexico and the Southwestern USA*, *374*, 381.

Guyer, J. E., Wheeler, D., & Warren, J. A. (2009). FiPy:Partial differential equations with python. *Computing in Science and Engineering*, *11*, 6–15. https://doi.org/10.1109/MCSE.2009.52

Hall, C. A. (1991). Geology of the Point Sur-Lopez Point region, Coast Ranges, California: A part of the Southern California allochthon. *Geological Society of America Special Papers*, *266*, 1–41. https://doi.org/10.1130/SPE266-p1

Hall, C. A., & Saleeby, J. B. (2013). Salinia revisited: A crystalline nappe sequence lying above the Nacimiento fault and dispersed along the San Andreas fault system, central California. *International Geology Review*, *55*(13), 1575–1615. https://doi.org/10.1080/00206814.2013.825141

Hardebeck, J. L. (2010). Seismotectonics and fault structure of the California Central Coast. *Bulletin of the Seismological Society of America*, *100*(3), 1031–1050. https://doi.org/10.1785/0120090307

Helmstaedt, H., & Doig, R. (1975). Eclogite nodules from kimberlite pipes of the Colorado Plateau—Samples of subducted Franciscan-type oceanic lithosphere. *Physics and Chemistry of the Earth*, *9*, 95–111.

Hofmann, A. W. (1997). Mantle geochemistry: The message from oceanic volcanism. *Nature*, *385*, 219–229. https://doi.org/10.1038/385219a0

Hole, M. J., Rogers, G., Saunders, a. D., & Storey, M. (1991). Relation between alkalic volcanism and slab window formation. *Geology*, *19(June)*, 657–660. https://doi.org/10.1130/0091-7613(1991)019<0657

Humphreys, E. D. (1995). Post-Laramide removal of the Farallon slab, western United States. *Geology*, *23*, 987–990. https://doi.org/10.1130/0091-7613(1995)023<0987

Hurst, R. W. (1982). Petrogenesis of the Conejo volcanic suite, southern California: Evidence for mid-ocean ridge continental margin interactions. *Geology*, *10*(5), 267. https://doi.org/10.1130/0091-7613(1982)10<267:potcvs>2.0.co;2

Jean, M. M., Shervais, J. W., Choi, S. H., & Mukasa, S. B. (2010). Melt extraction and melt refertilization in mantle peridotite of the Coast Range ophiolite: An LA-ICP-MS study. *Contributions to Mineralogy and Petrology*, *159*(1), 113–136. https://doi.org/10.1007/s00410-009-0419-0

Johnson, K., Dick, H., & Shimizu, N. (1990). Melting in the oceanic upper mantle: An ion microprobe study of diopsides in abyssal peridotites. *Journal of Geophysical Research*, *95*(89), 2661–2678.

Jones, C. H., & Phinney, R. A. (1998). Seismic structure of the lithosphere from teleseismic converted arrivals observed at small arrays in the southern Sierra Nevada and vicinity, California. *Journal of Geophysical Research: Solid Earth*, *103*(B5), 10,065–10,090. https://doi.org/10.1029/97jb03540

Jones, C. H., Reeg, H., Zandt, G., Gilbert, H., Owens, T. J., & Stachnik, J. (2014). P-wave tomography of potential convective downwellings and their source regions, Sierra Nevada,California. *Geosphere*, *10*(3), 505–533. https://doi.org/10.1130/ges00961.1

Jové, C. F., & Coleman, R. G. (1998). Extension and mantle upwelling within the San Andreas fault zone, San Francisco Bay area, California. *Tectonics*, *17*(6), 883–890. https://doi.org/10.1029/1998TC900012

Kelemen, P. B., Braun, M., & Hirth, G. (2000). Spatial distribution of melt conduits in the mantle beneath oceanic spreading ridges: Observations from the Ingalls and Oman ophiolites. *Geochemistry Geophysics Geosystems*, *1*(1). https://doi.org/10.1029/1999GC000012

Kennedy, B. M. (1997). Mantle Fluids in the San Andreas Fault System, California. *Science*, *278(June)*, 1278–1281. https://doi.org/10.1126/science.278.5341.1278

Kidder, S., & Ducea, M. N. (2006). High temperatures and inverted metamorphism in the schist of Sierra de Salinas, California. *Earth and Planetary Science Letters*, *241*(3-4), 422–437.

Kidder, S., Ducea, M., Gehrels, G., Patchett, P. J., & Vervoort, J. (2003). Tectonic and magmatic development of the Salinian Coast Ridge Belt, California. *Tectonics*, *22*(5), 1058. https://doi.org/10.1029/2002TC001409

Kidder, S. B., Herman, F., Saleeby, J., Avouac, J. P., Ducea, M. N., & Chapman, a. (2013). Shear heating not a cause of inverted metamorphism. *Geology*, *41*(8), 899–902. https://doi.org/10.1130/G34289.1

Kinzler, R. J. (1997). Melting of mantle peridotite at pressures approaching the spinel to garnet transition: Application to mid-ocean ridge basalt petrogenesis. *Journal of Geophysical Research*, *102*(B1), 853. https://doi.org/10.1029/96JB00988

Kistler, R. W., & Champion, D. E. (2001). Rb-Sr whole-rock and mineral ages, K-Ar , Ar/Ar, and U-Pb mineral ages, and strontium, lead, neodymium, and oxygen isotopic compositions for granitic rocks from the Salinian composite terrane. California: USGS Open File Report, 01-453.

Klemme, S. (2004). The influence of Cr on the garnet spinel transition in the Earth's mantle: Experiments in the system MgO Cr2O3 SiO2 and thermodynamic modelling. *Lithos*, *77*(1-4), 639–646. https://doi.org/10.1016/j.lithos.2004.03.017

Klemme, S., & O'Neill, H. S. C. (2000). The near-solidus transition from garnet lherzolite to spinel lherzolite. *Contributions to Mineralogy and Petrology*, *138*(3), 237–248. https://doi.org/10.1007/s004100050560

Köhler, T., & Brey, G. (1990). Calcium exchange between olivine and clinopyroxene calibrated as a geothermobarometer for natural peridotites from 2 to 60 kb with applications. *Geochimica et Cosmochimica Acta*, *54*, 2375–2388.

Lachenbruch, A., & Sass, J. (1980). Heat flow and energetics of the San Andreas Fault Zone. *Journal of Geophysical Research*, *85*, 6185–6222.

Le Pourhiet, L., Gurnis, M., & Saleeby, J. (2006). Mantle instability beneath the Sierra Nevada Mountains in California and Death Valley extension. *Earth and Planetary Science Letters*, *251*, 104–119. https://doi.org/10.1016/j.epsl.2006.08.028

Lee, C.-T., Rudnick, R. L., & Brimhall, G. H. (2001). Deep lithospheric dynamics beneath the Sierra Nevada during the Mesozoic and Cenozoic as inferred from xenolith petrology. *Geochemistry, Geophysics, Geosystems*, *2*(12). https://doi.org/10.1029/2001gc000152

Lee, C.-T., Yin, Q., Rudnick, R. L., & Jacobsen, S. B. (2001). Preservation of ancient and fertile lithospheric mantle beneath the southwestern United States. *Nature*, *411*, 69.

Lee, C.-T. A., Cheng, X., & Horodyskyj, U. (2006). The development and refinement of continental arcs by primary basaltic magmatism, garnet pyroxenite accumulation, basaltic recharge and delamination: Insights from the Sierra Nevada, California. *Contributions to Mineralogy and Petrology*, *151*(2), 222–242. https://doi.org/10.1007/s00410-005-0056-1

Lee, C.-T. T. A, Harbert, A., & Leeman, W. P. (2007). Extension of lattice strain theory to mineral/mineral rare-earth element partitioning: An approach for assessing disequilibrium and developing internally consistent partition coefficients between olivine, orthopyroxene, clinopyroxene and basaltic melt. *Geochimica et Cosmochimica Acta*, *71*, 481–496. https://doi.org/10.1016/j.gca.2006.09.014

Levandowski, W., & Jones, C. H. (2015). Linking Sierra Nevada, California, uplift to subsidence of the Tulare basin using a seismically derived density model. *Tectonics*, *34*, 2349–2358. https://doi.org/10.1002/2015tc003824

Li, X., Yuan, X., & Kind, R. (2007). The lithosphere-asthenosphere boundary beneath the western United States. *Geophysical Journal International*, *170*, 700–710. https://doi.org/10.1111/j.1365-246x.2007.03428.x

Liang, Y., Sun, C., & Yao, L. (2013). A REE-in-two-pyroxene thermometer for mafic and ultramafic rocks. *Geochimica et Cosmochimica Acta*, *102*, 246–260. https://doi.org/10.1016/j.gca.2012.10.035

Liu, L., Gurnis, M., Seton, M., Saleeby, J., Müller, R. D., & Jackson, J. M. (2010). The role of oceanic plateau subduction in the Laramide orogeny. *Nature Geoscience*, *3*, 353–357. https://doi.org/10.1038/ngeo829

Livaccari, R. F., & Perry, F. V. (1993). Isotopic evidence for preservation of Cordilleran lithospheric mantle during the Sevier-Laramide orogeny, western United States. *Geology*, *21*(8), 719. https://doi.org/10.1130/0091-7613(1993)021<0719:iefpoc>2.3.co;2

Livaccari, R. F., Burke, K., & Singör, A. M. C. (1981). Was the Laramide orogeny related to subduction of an oceanic plateau? *Nature*, *289*, 276–278. https://doi.org/10.1038/289276a0

Luffi, P., Saleeby, C.-T., Lee, a., & Ducea, M. N. (2009). Lithospheric mantle duplex beneath the central Mojave Desert revealed by xenoliths from Dish Hill, California. *Journal of Geophysical Research*, *114*, B03,202. https://doi.org/10.1029/2008JB005906

Malin, P. E., Goodman, E. D., Henyey, T. L., Li, Y. G., Okaya, D. A., & Saleeby, J. B. (1995). Significance of seismic reflections beneath a tilted exposure of deep continental crust, Tehachapi Mountains, California. *Journal of Geophysical Research: Solid Earth*, *100*(B2), 2069–2087. https://doi.org/10.1029/94jb02127

Mancktelow, N. S., & Grasemann, B. (1997). Time-dependent effects of heat advection and topography on cooling histories during erosion. *Tectonophysics*, *270*(3-4), 167–195. https://doi.org/10.1016/S0040-1951(96)00279-X

Matthews, V. (1976). *Correlation of Pinnacles and Neenach Volcanic Formations and Their Bearing on San Andreas Fault Problem*. *AAPG Bulletin*, 60(12). https://doi.org/10.1306/c1ea3a82-16c9-11d7-8645000102c1865d

McCulloch, M., & Wasserburg, G. (1978). Sm-Nd and Rb-Sr chronology of continental crust formation. *Science*, *200*, 1003–1011.

Medaris, G., Wang, H., & Fournelle, J. (1999). A cautionary tale of spinel peridotite thermobarometry: An example from xenoliths of Kozākov Volcano, Czech Republic. *Geolines*, *9*, 92.

Mei, S., Suzuki, A. M., Kohlstedt, D. L., Dixon, N. A., & Durham, W. B. (2010). Experimental constraints on the strength of the lithospheric mantle. *Journal of Geophysical Research*, *115*(B8). https://doi.org/10.1029/2009JB006873

Murchey, B. L., & Jones, D. L. (1984). *Age and significance of chert in the Franciscan Complex in the San Francisco Bay Region*. Franciscan Geology of Northern California.

Nadin, E. S., & Saleeby, J. B. (2008). Disruption of regional primary structure of the Sierra Nevada batholith by the Kern Canyon fault system, California. In J. Wright & J. W. Shervais (Eds.) (Chap. 15, Vol. 438, pp. 429–454). The Geological Society of America. https://doi.org/10.1130/978-0-8137-2438-6

Nesse, W. D. (2000). *Introduction to mineralogy*. Oxford: Oxford University Press.

Nicholson, C., Sorlien, C. C., & Luyendyk, B. P. (1992). Deep crustal structure and tectonics in the offshore southern Santa Maria Basin, California. *Geology*, *20*(3), 239–&. https://doi.org/10.1130/0091-7613(1992)020<0239

Nicholson, C., Sorlien, C. C., Atwater, T., Crowell, J. C., & Luyendyk, B. P. (1994). Microplate capture, rotation of the western Transverse Ranges, and initiation of the San Andreas transform as a low-angle fault system. *Geology*, *22*(6), 491–495. https://doi.org/10.1130/0091-7613(1994)022<0491:MCROTW>2.3.CO;2

Nimis, P., & Grütter, H. (2010). Internally consistent geothermometers for garnet peridotites and pyroxenites. *Contributions to Mineralogy and Petrology*, *159*(3), 411–427. https://doi.org/10.1007/s00410-009-0455-9

Nixon, P. H. (1987). *Mantle xenoliths*. New York, NY: John Wiley and Sons Inc.

O'Neill, H. (1981). The transition between spinel lherzolite and garnet lherzolite, and its use as a geobarometer. *Contributions to Mineralogy and Petrology*, *77*, 185–194.

O'Reilly, S. Y. (1997). Minor elements in olivine from spinel lherzolite xenoliths: Implications for thermobarometry. *Mineralogical Magazine*, *61*(405), 257–269. https://doi.org/10.1180/minmag.1997.061.405.09

O'Reilly, S. Y., & Griffin, W. L. (2010). The continental lithosphere-asthenosphere boundary: Can we sample it? *Lithos*, *120*(1-2), 1–13. https://doi.org/10.1016/j.lithos.2010.03.016

Otamendi, J. E., Ducea, M. N., Tibaldi, A. M., Bergantz, G. W., de la Rosa, J. D., & Vujovich, G. I. (2009). Generation of tonalitic and dioritic magmas by coupled partial melting of gabbroic and metasedimentary rocks within the deep crust of the Famatinian magmatic arc, Argentina. *Journal of Petrology*, *50*(5), 841–873. https://doi.org/10.1093/petrology/egp022

Ozacar, A. A., & Zandt, G. (2009). Crustal structure and seismic anisotropy near the San Andreas Fault at Parkfield, California. *Geophysical Journal International*, *178*(2), 1098–1104. https://doi.org/10.1111/j.1365-246x.2009.04198.x

Page, B. M. (1981). The southern Coast Ranges. *The geotectonic development of California; Rubey*, *I*(1), 329–417.
Pike, J. E. N., & Schwarzman, E. C. (1977). Classification of textures in ultramafic xenoliths. *The Journal of Geology*, *85*(1), 49–61. https://doi.org/10.2307/30068676
Pikser, J. E., Forsyth, D. W., & Hirth, G. (2012). Along-strike translation of a fossil slab. *Earth and Planetary Science Letters*, *331-332*, 315–321. https://doi.org/10.1016/j.epsl.2012.03.027
Platt, J. P., & Behr, W. M. (2011). Deep structure of lithospheric fault zones. *Geophysical Research Letters*, *38*(24), L24308. https://doi.org/10.1029/2011GL049719
Pollack, H. N., & Chapman, D. S. (1977). On the regional variation of heat flow, geotherms, and lithospheric thickness. *Tectonophysics*, *38*, 279–296. https://doi.org/10.1016/0040-1951(77)90215-3
Robinson, J. A. C., & Wood, B. J. (1998). The depth of the spinel to garnet transition at the peridotite solidus. *Earth and Planetary Science Letters*, *164*(1-2), 277–284. https://doi.org/10.1016/S0012-821X(98)00213-1
Royden, L. (1993). The steady state thermal structure of eroding orogenic belts and accretionary prisms. *Journal of Geophysical Research: Solid Earth*, *98*, 4487–4507.
Saleeby, J. (2003). Production and loss of high-density batholithic root, southern Sierra Nevada, California. *Tectonics*, *22*(6), 1064. https://doi.org/10.1029/2002TC001374
Saleeby, J., Speed, R., Blake, M., Allmendinger, R., Gans, P. B., Kistler, R. W., et al. (1986). Continent-ocean transect, corridor C2, Monterey Bay offshore to the Colorado Plateau, *Map and chart series TRA C2, 2 sheets, scale 1:500,000* (pp. 87). Geologic Society of America.
Saleeby, J., Farley, K. A., Kistler, R. W., & Fleck, R. J. (2007). Thermal evolution and exhumation of deep-level batholithic exposures, southernmost Sierra Nevada, California, *Special Paper 419: Convergent Margin Terranes and Associated Regions: A Tribute to W.G. Ernst* (pp. 39–66). Geological Society of America. https://doi.org/10.1130/2007.2419(02)
Saleeby, J., Le Pourhiet, L., Saleeby, Z., Gurnis, M., Pourhiet, L. L., Saleeby, Z., & Gurnis, M. (2012). Epeirogenic transients related to mantle lithosphere removal in the southern Sierra Nevada region, California. Part I: Implications of thermomechanical modeling. *Geosphere*, *8*(6), 1286–1309. https://doi.org/10.1130/GES00746.1
Saleeby, J., Saleeby, Z., & Le Pourhiet, L. (2013). Epeirogenic transients related to mantle lithosphere removal in the southern Sierra Nevada region, California: Part II. Implications of rock uplift and basin subsidence relations. *Geosphere*, *9*(3), 394–425. https://doi.org/10.1130/GES00816.1
Saleeby, J. B., Saleeby, Z., Robbins, J., & Gillespie, J. (2016). *Sediment provenance and dispersal of Neogene-Quaternary strata of the southeastern San Joaquin Basin and its transition into the southern*. Sierra Nevada, CA: Geosphere.
Schott, R. C., & Johnson, C. M. (1998). Sedimentary record of the Late Cretaceous thrusting and collapse of the Salinia-Mojave magmatic arc. *Geology*, *26*(4), 327. https://doi.org/10.1130/0091-7613(1998)026<0327:SROTLC>2.3.CO;2
Schott, R. C., & Johnson, C. M. (2001). Garnet-bearing trondhjemite and other conglomerate clasts from the Gualala basin, California: Sedimentary record of the missing western portion of the Salinian magmatic arc? *Geological Society of America Bulletin*, *113*(7), 870–880.
Seiders, V. (1989). *Geologic map of the Burnett Peak Quadrangle, Monterey and San Luis Obispo Counties*. California: U.S. Geological Survey Geologic Maps.
Seton, M., Müller, R., Zahirovic, S., Gaina, C., Torsvik, T., Shephard, G., et al. (2012). Global continental and ocean basin reconstructions since 200Ma. *Earth-Science Reviews*, *113*(3-4), 212–270. https://doi.org/10.1016/j.earscirev.2012.03.002
Sharma, M., Basu, A. R., Cole, R. B., & DeCelles, P. G. (1991). Basalt-rhyolite volcanism by {MORB}-continental crust interaction: Nd, Sr-isotopic and geochemical evidence from southern San Joaquin Basin, California. *Contributions to Mineralogy and Petrology*, *109*(2), 159–172. https://doi.org/10.1007/bf00306476
Sharman, G. R., Graham, S. A., Grove, M., & Hourigan, J. K. (2013). A reappraisal of the early slip history of the San Andreas fault, central California, {USA}. *Geology*, *41*(7), 727–730. https://doi.org/10.1130/g34214.1
Shervais, J. W., Wilshire, H. G., & Schwarzman, E. C. (1973). Garnet clinopyroxenite xenolith from Dish Hill, California. *Earth and Planetary Science Letters*, *19*(2), 120–130. https://doi.org/10.1016/0012-821x(73)90106-4
Shields, J. E., & Chapman, A. D. (2016). Late Cretaceous tectonic displacement of sub-continental mantle lithosphere beneath the SW U.S. Cordillera: Mantle xenolith constraints from the Colorado Plateau transition zone (central Arizona). *Geological Society of America Abstracts with Programs*, *48*.
Sliter, W. V. (1984). Foraminifers from Cretaceous limestone of the Franciscan Complex, northern California, in. In M. Blake (Ed.), Franciscan Geology of Northern California: Pacific Section S.E.P.M., 43, 149–162
Smith, P. M., & Asimow, P. D. (2005). Adiabat-1ph: A new public front-end to the MELTS, pMELTS, and pHMELTS models. *Geochemistry, Geophysics, Geosystems*, *6*(2), Q02,004. https://doi.org/10.1029/2004GC000816
Stanley, B. R. G., Wilson, D. S., & McCrory, P. A. (2000). Locations and ages of middle tertiary volcanic centers in coastal California. *USGS Open File Reports*, *00*(154), 0–27.
Stein, C. A. (1995). *Heat flow of the Earth* (pp. 144–158). AGU Reference Shelf. https://doi.org/10.1112/S0024609301008396
Stein, C. A., & Stein, S. (1992). A model for the global variation in oceanic depth and heat flow with lithospheric age. *Nature*, *356*, 133–135. https://doi.org/10.1038/359123a0
Sun, C., & Liang, Y. (2012). Distribution of REE between clinopyroxene and basaltic melt along a mantle adiabat: Effects of major element composition, water, and temperature. *Contributions to Mineralogy and Petrology*, *163*(5), 807–823. https://doi.org/10.1007/s00410-011-0700-x
Sun, D., Gurnis, M., Saleeby, J., & Helmberger, D. (2017). A dipping, thick segment of the Farallon Slab beneath Central US. *Journal of Geophysical Research: Solid Earth*. https://doi.org/10.1002/2016JB013915
Sun, S.-s., & McDonough, W. F. (1989). Chemical and isotopic systematics of oceanic basalts: Implications for mantle composition and processes. *Geological Society, London, Special Publications*, *42*(1), 313–345. https://doi.org/10.1144/GSL.SP.1989.042.01.19
Taylor, W. (1998). An experimental test of some geothermometer and geobarometer formulations for upper mantle peridotites with application to the thermobarometry of fertile lherzolite and garnet websterite. *Neues Jahrbuch für Mineralogie Abhandlungen*, *172*(2), 381–408.
Brink, t, Shimizu, U. N., & Molzer, P. (1999). Plate deformation at depth under northern California: Slab gap or stretched slab? *Tectonics*, *18*(6), 1084–1098.
Thorkelson, D. J., & Breitsprecher, K. (2005). Partial melting of slab window margins: Genesis of adakitic and non-adakitic magmas. *Lithos*, *79*(1-2 SPEC. ISS.), 25–41. https://doi.org/10.1016/j.lithos.2004.04.049
Thorkelson, D. J., & Taylor, R. P. (1989). Cordilleran slab windows. *Geology*, *17*(9), 833–836. https://doi.org/10.1130/0091-7613(1989)017<0833:CSW>2.3.CO;2

Titus, S. J., Medaris, L. G., Wang, H. F., & Tikoff, B. (2007). Continuation of the San Andreas fault system into the upper mantle: Evidence from spinel peridotite xenoliths in the Coyote Lake basalt, central California. *Tectonophysics*, *429*(1-2), 1–20. https://doi.org/10.1016/j.tecto.2006.07.004

Tréhu, A (1991). Tracing the subducted oceanic crust beneath the central California continental margin: Results from ocean bottom seismometers deployed during the 1986 Pacific Gas and Electric EDGE experiment. *Journal of Geophysical Research*, *96*(90), 6493–6506.

Tréhu, A. M., & Wheeler, W. H. (1987). Possible evidence for subducted sedimentary materials beneath central California. *Geology*, *15*(3), 254–258. https://doi.org/10.1130/0091-7613(1987)15<254:PEFSSM>2.0.CO;2

Turcotte, D., & Schubert, G. (2002). *Geodynamics 2 ed.*Cambridge: Cambridge University Press.

Usui, T., Nakamura, E., Kobayashi, K., Maruyama, S., & Helmstaedt, H. (2003). Fate of the subducted Farallon plate inferred from eclogite xenoliths in the Colorado Plateau. *Geology*, *31*(7), 589. https://doi.org/10.1130/0091-7613(2003)031<0589:fotsfp>2.0.co;2

Van Wijk, J., Govers, R., & Furlong, K. (2001). Three-dimensional thermal modeling of the California upper mantle: A slab window vs. stalled slab. *Earth and Planetary Science Letters*, *186*, 175–186.

Vilā, M., Fernández, M., & Jiménez-Munt, I. (2010). Radiogenic heat production variability of some common lithological groups and its significance to lithospheric thermal modeling. *Tectonophysics*, *490*(3-4), 152–164. https://doi.org/10.1016/j.tecto.2010.05.003

Wang, Y., Forsyth, D. W., Rau, C. J., Carriero, N., Schmandt, B., Gaherty, J. B., & Savage, B. (2013). Fossil slabs attached to unsubducted fragments of the Farallon plate. In *Proceedings of the National Academy of Sciences*, pp. 5342–6. https://doi.org/10.1073/pnas.1214880110

Warren, J. (2016). Global variations in abyssal peridotite compositions. *Lithos*, *248-251*, 193–219. https://doi.org/10.1016/j.lithos.2015.12.023

Warren, J. M., & Hirth, G. (2006). Grain size sensitive deformation mechanisms in naturally deformed peridotites. *Earth and Planetary Science Letters*, *248*(1-2), 438–450. https://doi.org/10.1016/j.epsl.2006.06.006

Wasserburg, G., Jacobsen, S., DePaolo, D., McCulloch, M., & Wen, T. (1981). Precise determination of ratios, Sm and Nd isotopic abundances in standard solutions. *Geochimica et Cosmochimica Acta*, *45*(12), 2311–2323. https://doi.org/10.1016/0016-7037(81)90085-5

Wilshire, H., Meyer, C. E., Nakata, J. K., & Calk, L. C. (1988). Mafic and ultramafic xenoliths from volcanic rocks of the western United States. U.S. Geological Survey Professional Paper, 1443.

Wilson, D. S., McCrory, P. a., & Stanley, R. G. (2005). Implications of volcanism in coastal California for the Neogene deformation history of western North America. *Tectonics*, *24*, 1–22. https://doi.org/10.1029/2003TC001621

Witt-Eickschen, G., & O'Neill, H. S. (2005). The effect of temperature on the equilibrium distribution of trace elements between clinopyroxene, orthopyroxene, olivine and spinel in upper mantle peridotite. *Chemical Geology*, *221*(1-2), 65–101. https://doi.org/10.1016/j.chemgeo.2005.04.005

Wood, D. J., & Saleeby, J. B. (1997). Late Cretaceous-Paleocene extensional collapse and disaggregation of the southernmost Sierra Nevada batholith. *International Geology Review*, *39*(11), 973–1009. https://doi.org/10.1080/00206819709465314

Workman, R. K., & Hart, S. R. (2005). Major and trace element composition of the depleted MORB mantle (DMM). *Earth and Planetary Science Letters*, *231*(1-2), 53–72. https://doi.org/10.1016/j.epsl.2004.12.005

Yan, Z., & Clayton, R. W. (2007). A notch structure on the Moho beneath the Eastern San Gabriel Mountains. *Earth and Planetary Science Letters*, *260*(3-4), 570–581. https://doi.org/10.1016/j.epsl.2007.06.017

Yan, Z., Clayton, R. W., & Saleeby, J. (2005). Seismic refraction evidence for steep faults cutting highly attenuated continental basement in the central Transverse ranges, California. *Geophysical Journal International*, *160*(2), 651–666. https://doi.org/10.1111/j.1365-246x.2005.02506.x

Zandt, G., Gilbert, H., Owens, T. J., Ducea, M., Saleeby, J., & Jones, C. H. (2004). Active foundering of a continental arc root beneath the southern Sierra Nevada in California. *Nature*, *431*, 41–46. https://doi.org/10.1038/nature02847

Erratum

In the originally published version of this article, the key in Figure 17 was not rendered correctly, and there was a minor typographical error in Figure 19. These figures have since been corrected and this version may be considered the authoritative version of record.